INVESTIGATION OF MICROSTRUCTURAL EFFECTS IN ROLLING CONTACT FATIGUE

by

Dallin Morris

A Dissertation

Submitted to the Faculty of Purdue University

In Partial Fulfillment of the Requirements for the degree of

Doctor of Philosophy

Department of Mechanical Engineering

West Lafayette, Indiana

August 2021

THE PURDUE UNIVERSITY GRADUATE SCHOOL
STATEMENT OF COMMITTEE APPROVAL

Dr. Farshid Sadeghi, Chair
Department of Mechanical Engineering

Dr. Anil Bajaj
Department of Mechanical Engineering

Dr. Rodney Trice
Department of Materials Engineering

Dr. Marcial Gonzalez
Department of Mechanical Engineering

Approved by:
Dr. Nicole L. Key

This dissertation is dedicated my Heavenly Father for his continued guidance and to my dearest wife Chanele.

ACKNOWLEDGMENTS

I would like to thank my advisor Professor Farshid Sadeghi for providing me the opportunity to join his laboratory. Under his guidance I have been able to advance my education and develop technical excellence. I would also like to thank Prof. Anil Bajaj, Prof. Marcial Gonzalez, and Prof. Rodney Trice for serving on my advisory committee.

I would like to thank all my past and present friends at Mechanical Engineering Tribology Laboratory (METL) for their help and support. They provided a productive and friendly environment to work.

I would like to thank Dr. Chinpei Wang from Cummins for his mentoring and interest in this work.

Lastly, I express deep gratitude for my exceptional wife, Chanele, for her consistent support and patience.

TABLE OF CONTENTS

LIST OF TABLES

LIST OF FIGURES

ABSTRACT

Rolling contact fatigue (RCF) is a common cause of failure in tribological machine components such as rolling-element bearings (REBs). Steels selected for RCF applications are subject to various material processes in order to produce martensitic microstructures. An effect of such material processing is the retention of the austenitic phase within the steel microstructure. Retained austenite (RA) transformation in martensitic steels subjected to RCF is a well-established phenomenon. In this investigation, a novel approach is developed to predict martensitic transformations of RA in steels subjected to RCF. A criteria for phase transformations is developed by comparing the required thermodynamic driving force for transformations to the energy dissipation in the microstructure. The method combines principles from phase transformations in solids with a damage mechanics framework to calculate energy availability for transformations. The modeling is then extended to incorporate material alterations as a result of RA transforming within the material. A continuum damage mechanics (CDM) FEM simulation is used to capture material deterioration, phase transformations, and the formation of internal stresses as a result of RCF. Crystal lattice orientation is included to modify energy requirements for RA transformation. Damage laws are modified to consider residual stresses and different components of the stress state as the drivers of energy dissipation. The resulting model is capable of capturing microstructural evolution during RCF.

The development and stability of internal stresses caused by RA transformation in bearing steel material was experimentally investigated. Specimens of 8620 case carburized steel were subjected to torsional fatigue at specific stress levels for a prescribed number of cycles. X-ray diffraction techniques were used to measure residual stress and RA volume fraction as a function of depth in the material. A model is set forth to predict compressive residual stress in the material as a function of RA transformation and material relaxation. Modeling results are corroborated with experimental data. In addition, varying levels of retained austenite (RA) were achieved through varying undercooling severity in uniformly treated case carburized 8620 steel. Specimens were characterized via XRD and EBSD techniques to determine RA volume fraction and material characteristics prior to rolling contact fatigue (RCF). Higher RA volume fractions did not lead to improvement in RCF lives. XRD measurements after RCF testing indicated that little RA

decomposition had occurred during RCF. The previously established RCF simulations were modified to investigate the effects of RA stability on RCF. The results obtained from the CDM FEM captured similar behavior observed in the experimental results. Utilizing the developed model, a parametric study was undertaken to examine the effects of RA quantity, RA stability, and applied pressure on RCF performance. The study demonstrates that the energy requirements to transform the RA phase is critical to RCF performance.

CHAPTER 1. INTRODUCTION

1.1 Background

Fatigue is the failure of machine components subjected to cyclic loads that are below the ultimate or yield strength of the material. In components such as rolling element bearings (REBs), gears, cam-followers, and rail-wheel contacts, rolling contact fatigue (RCF) is the major cause of failure. RCF has different modes of failure that vary in terms of driving factor and crack location. The most common types of RCF are surface pitting or subsurface spalling. Figure 1.1 illustrates and compares two such types of failure. As can be seen, in surface pitting, the cracks start from the surface and propagate into the material resulting in superficial pits. The root cause of surface pitting is high stress due to asperity contact between the two surfaces as a result of improper lubrication or contaminants in the lubricant. Subsurface spalling is different in both crack initiation and propagation. In this type of fatigue failure, cracks initiate within the material and propagate towards the surface resulting in deeper spalls compared to surface initiated failures.

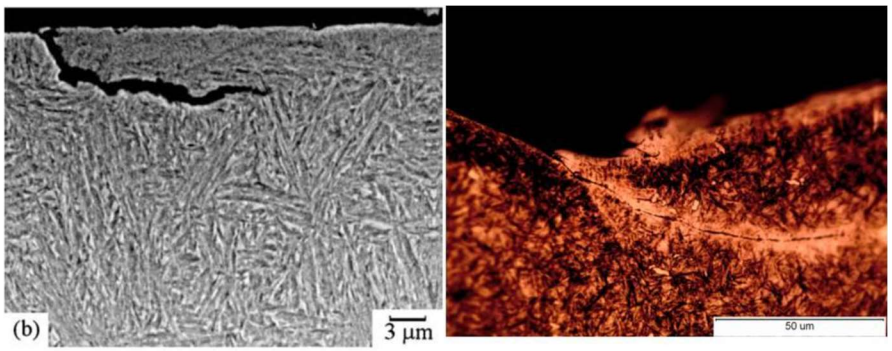

Figure 1.1: Surface pitting (left), subsurface spalling (right). Note the difference in the crack depths.

As the current document focuses on microstructural evolution occurring during a subsurface failure mode, it would be beneficial to present the fundamentals of this type of failure. Consider the subsurface stresses when the material is subjected to Hertzian contact. Figure 1.2 depicts the stress history for a point located at 0.5b below the surface as the ball rolls over the point. As can be seen, shear stress is the only stress at the subsurface of the material which alternates between positive and negative values. Based on a similar analysis, Lundberg and

Palmgren [1] suggested that subsurface shear stress alteration is the main cause for subsurface spalling.

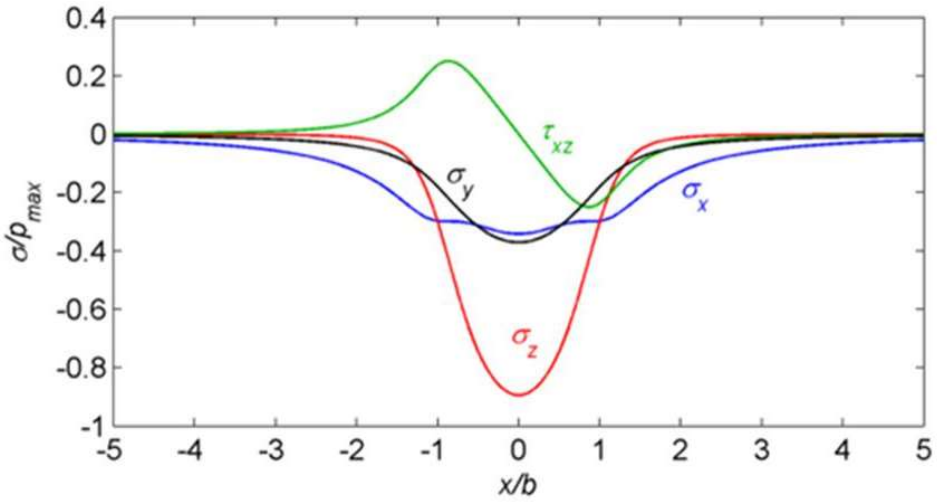

Figure 1.2: Stress history experienced by a material point at the maximum orthogonal shear stress as Hertzian line contact passes over the surface.

1.2 RCF vs Classical Fatigue

Many of the observations and assumptions applied to classical fatigue problems do not translate to an RCF phenomenon. Below are listed some reasons why RCF is a more challenging and involved problem.

1. Classical fatigue mostly occurs at the surface. The main reason is due to existence of scratches and/ or notches on the surface that cause stress concentration points or loading conditions such as bending or torsion produce maximum stresses at the surface. Investigation of surface initiated fatigue is generally easier as the cracks are mostly visible and they can be tracked during the propagation stage. However, in RCF, the cracks mostly initiate and propagate from the subsurface of the material which makes it more difficult to locate and track them.
2. In classical fatigue testing, e.g. uniaxial or torsion fatigue, specimens are subjected to loadings that produce bulk stresses. This causes damage to a large volume of the material and failure happens at the most critical point due to existence of stress risers like defects or inclusions. However, the stresses in RCF are highly localized within the non-conformal contact regions, e.g. a rolling element on a bearing raceway. Consequently only very small

volumes of the material are subjected to very large values of stress and a significant stress gradient versus location exists in the matrix.

3. At such small scales, it is not easy to apply common fatigue analysis methods such as linear elastic fracture mechanics (LEFM). This is mainly due to the crack sizes which are comparable to microstructural grain size. Thus, the crack propagation can be affected by microstructural geometry of the material. This makes it of great importance to differentiate between intergranular and transgranular crack propagation assumptions in RCF studies.
4. There is a large compressive component of hydrostatic stress in rolling contacts which tends to inhibit Mode I crack growth, but there is not sufficient information regarding how it affects the Mode II crack growth which is the main cause of RCF.
5. Different stress components, as pictured in Figure 1.2, experience their peaks at different times during a loading cycle. This culminates in a complex multiaxial state of stress which changes the direction and magnitude of principle stresses at different moments. This makes it very important to consider the history of all stress components during loading cycles.

The above points are some of the reasons that make RCF and RCF related phenomena more challenging to investigate and understand. The problem is further complicated by the heterogeneity and instability of the material microstructure. The next sections provide background into the heterogeneity and unstable nature of steels manufactured for RCF scenarios.

1.3 Binary Fe-C systems

The material often referred to as steel is principally iron (Fe) with a small composition of carbon (C) and other alloying elements. Depending on composition and temperature, iron and carbon produce many different material phases. Figure 1.3 presents the different phases of a Fe-C system in equilibrium as a function of temperature and carbon composition. The three phases of interest in the diagram are austenite, ferrite, and cementite or carbide. The three phases are distinct based on their atomic organization or structure. Austenite or γ phase is a face centered cubic (FCC) lattice structure and has the highest atomic packing density with 4 atoms per unit cell. Ferrite or α phase is a body centered cubic (BCC) lattice structure with 2 atoms per unit cell. Carbide is orthorhombic unit cell containing twelve iron atoms and four carbon atoms. The large

lattice parameter and large Burgers vectors results in high hardness in contrast to the easily deformed γ and α phases [2].

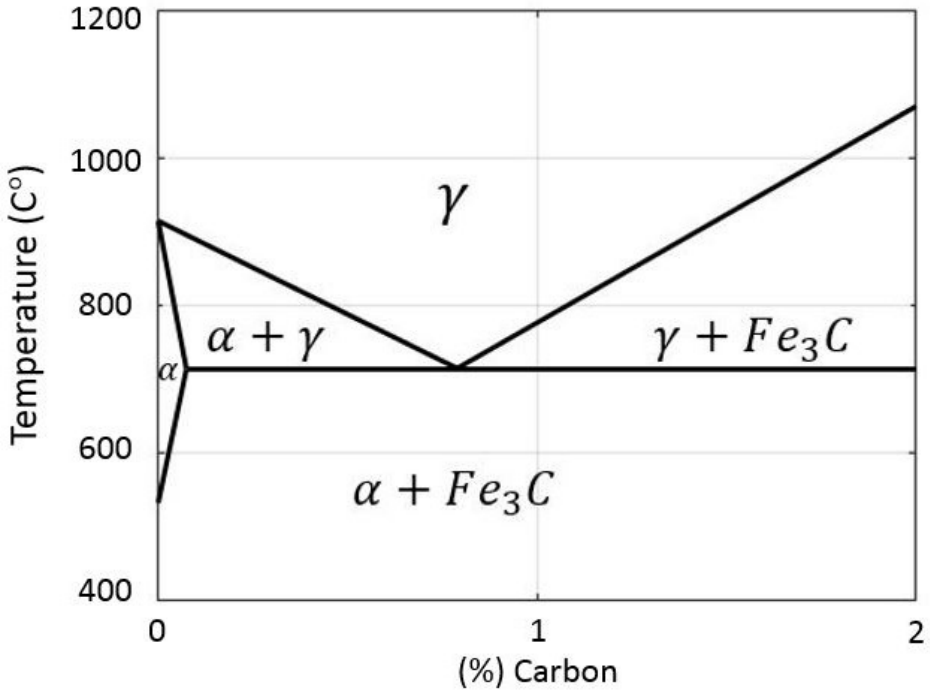

Figure 1.3: Binary Fe-C system phase diagram of eutectic steel (0.80% carbon) with slow cooling. α= Ferrite, γ= Austenite, Fe_3 C= Cementite or Carbide.[3]

Up to this point the discussion has been focused on phases existing in steel based on slow and gradual changes of temperature or composition. However, steel microstructure can be greatly affected by the rate at which change occurs. A typical time-temperature transformation (TTT) diagram for plain carbon steel is presented in Figure 1.4. Through careful control of heating and cooling rates, various steel microstructures can be produced which provide various material properties. As indicated by Figure 1.4, martensite is generated by rapid quenching from the high temperature austenite phase. The martensitic lattice structure in steels is a body centered tetragonal structure due to carbon atoms located on interstitial sites between iron atoms. This results in a highly deformed crystal structure which produces the characteristically high hardness of martensite. Without consideration of other alloying elements within the system, a simple plain carbon steel can produce a variety of unique microstructures. It is important to note, however, that not all microstructures are equally stable.

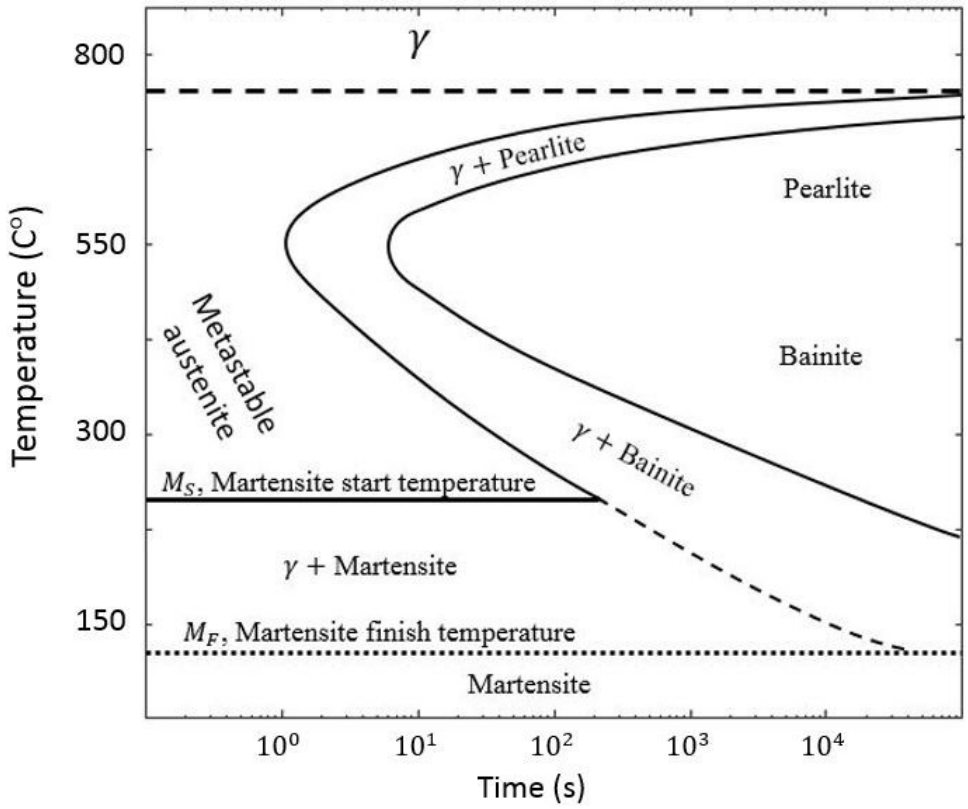

Figure 1.4: Time temperature transformation diagram for plain carbon eutectoid steel. [3]

1.4 Phase Transformations in Solids

The three most common phases of material are gas, liquid, and solid. A material will shift between these different phases of matter based on available energy. However, as demonstrated by Figure 1.3, materials in a solid state of matter can have a multiplicity of phases present depending on temperature and chemical composition. The stability of one phase at a particular temperature is due to the thermodynamics of the system and is described by the Gibbs free energy [4]. The Gibbs free energy (G) is described as

$$G = H - TS \tag{1.1}$$

where H is the enthalpy, T is the absolute temperature, and S is the entropy of the system.

Figure 1.5 illustrates an important difference between stable and metastable equilibrium. Location A on the diagram demonstrates stable equilibrium where the change in the Gibbs free energy is zero ($dG = 0$) and the Gibbs free energy is at the lowest value possible. Location B is a

metastable configuration as $dG = 0$ but a lower energy state exists. A phase transformation would occur if the material were able to move from location B to location A. However, an energy barrier (ΔG) exists which does not allow the transformation to occur. A driving force providing energy greater than ΔG would enable the material to move from the metastable equilibrium to a state of stable equilibrium.

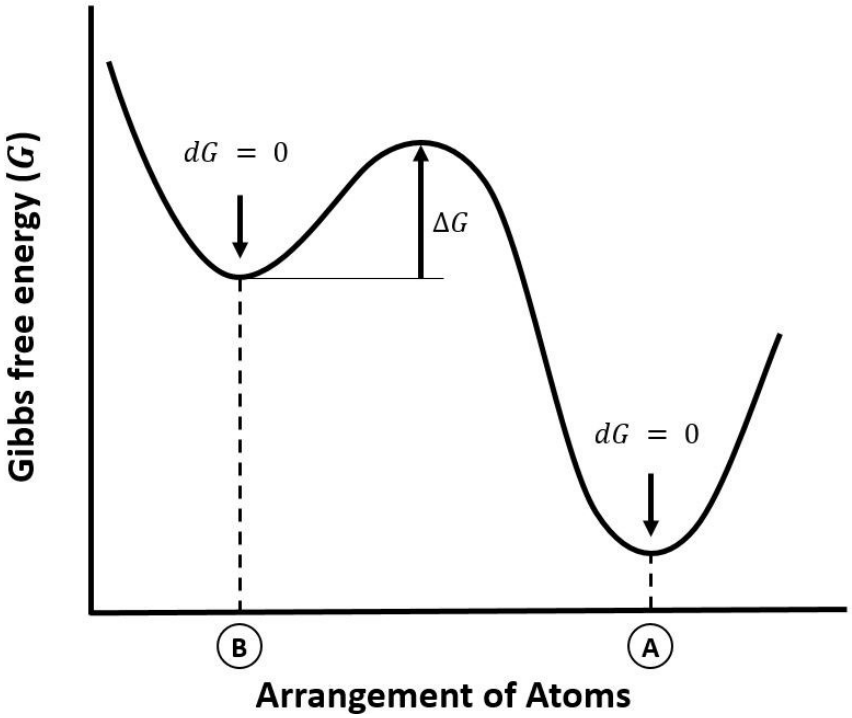

Figure 1.5: Diagram illustrating the difference between stable and metastable equilibrium.

1.5 Bearing Steels

A subgroup of steels known as "bearing" steels have been developed specifically for RCF scenarios. 52100 or 100Cr6, 8620, and M50 are a few examples of bearing quality steels. Bearing steels are generally characterized by fewer inclusions within the microstructure, good wear resistance, and high hardness (58 – 64 Rockwell C) which improves RCF performance [5,6]. The manufacturing process of bearing steels permits great flexibility in developing specialized microstructures. Depending on temperature and time of tempering, bearing steels can have strongly martensitic structures with high carbon concentrations and large carbides [7] or bainitic steels of ultrafine carbides embedded in ferritic sheaves [8]. Regardless of desired microstructure all bearing steels must undergo rapid quenching to produce high material hardness. As a result of

rapid cooling, the steel microstructure is heterogeneous. The martensite, carbide, and austenite phases observed in Figure 1.6 illustrates the heterogeneous nature of bearing steels.

Aside from the heterogeneity of the material system, the system is also somewhat unstable. The austenite present in the system is in metastable equilibrium. Therefore, given proper conditions, the austenite can undergo a phase transformations within the steel microstructure. This attribute of the entrapped or retained austenite (RA) has led to extensive investigations of the effect of RA in RCF.

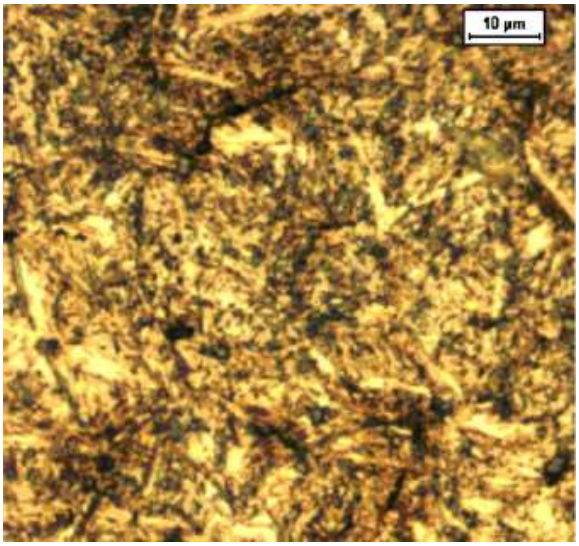

Figure 1.6: Image of bearing steel microstructure prior to tempering [9]. RA is the white area in the image.

1.6 Effect of Retained Austenite in RCF

For many years, RA has been a focus of developing new steels for RCF applications. Many works have found an increase in RA volume fraction to be beneficial to RCF performance. [10–15] Such enhancements in RCF life is attributed to RA's ability to undergo a strain or temperature induced phase transformation. As previously mentioned, austenite is the highest atomic density for steel (FCC). However, after a phase transformation, the FCC structure is replaced by a BCC or body-centered tetragonal (BCT) structure. This causes a volume expansion in the material and produces internal compressive stresses. Richman et al. [16] suggested that the compressive stresses associated with the RA transformation is the cause of improved fatigue life. Huo et al. [17] found that RA transforms in the plastic zone near a crack tip acting to absorb energy, close

the crack, and therefore slow the rate of crack propagation. Antolovich et al. [18] also observed crack tip blunting caused by transformation of the austenitic phase. There is debate regarding by what mechanism RA is beneficial, however, the general consensus is that RA improves fatigue performance.

Depending on heat treatment and chemical composition, a high strength steel matrix can be composed of ~0 - 70% RA [19,20]. However, the benefits of RA during a fatigue process must also be considered within the context of utility. Most RCF application require tight tolerances to ensure proper functionality. Many investigations have identified RA as the cause of dimensional instability [21–26]. Dimensional instability in roller element bearings or gears can result in misalignment or interference which leads to premature failure [27].

1.7 Modeling RA Transformations

Unlike most phase transformations in solids, the RA transformation does not require diffusion of atoms. Instead, the transformation is martensitic or an orderly and rapid shift of the atoms to form a new structure. The martensitic transformation is typically triggered by temperature but is also influenced by the amount of strain in the material [28]. This behavior has led to extensive modeling and simulation of RA transformation under static loading [29–32]. While many models exist for a statically loaded condition, few seek to incorporate the RA transformation into a fatigue process.

Alley et al. [33] created a simulation to incorporate material microstructural considerations into the fatigue process. The simulation included the RA transformation caused by RCF using a crystal plasticity framework to incorporate the transformation induced plasticity. The simulation was impressive, however, limited as it did not provide any criteria to predict when the RA transformation would occur. As the RCF process leads to significant microstructural alterations over time, predicting at what point microstructural changes will occur is of great value for advances in simulating RCF performance.

1.8 Scope of this Work

As previously mentioned, a major focus of improving RCF performance is material based. Chemical composition, heat treating, and other manufacturing process allow for a variety of

materials to be evaluated under RCF conditions. RA volume fraction is one parameter that has been subject to many such investigations. Despite the significant interest in RA, work is lacking to incorporate RA within RCF simulations. This work focuses on the development of a system to include RA and the associated phase transformation into RCF simulations.

Chapter Two presents a thermodynamics based theory for predicting RA transformation during RCF. An energy based criteria is constructed by combining principles from phase transformations in solids with the field of damage mechanics. The criteria is implemented in an FEM simulation of RCF to corroborate results against experimental data.

Chapter Three furthers the RCF modeling by considering microstructural deterioration, the RA transformation, and residual stress formation occurring during RCF. Crystal orientation is included to modify the RA transformation requirement. Damage laws are modified to consider residual stresses and different components of the stress as the driver of failure. Common residual stress profiles achieved through various manufacturing post-processing procedures are implemented within the simulation. RCF performance is compared between the initial residual stress profiles.

Chapter Four discusses experimental data to investigate the stability and formation of residual stresses in bearing steel material due to RA transformation. Specimens of 8620 case carburized steel are subjected to torsional fatigue at specific stress levels for a prescribed number of cycles. X-ray diffraction techniques are used to measure residual stress and RA volume fraction as a function of depth in the material. A model is set forth to predict compressive residual stress in the material as a function of RA transformation and material relaxation. Model results are corroborated with experimental data.

Finally, Chapter Five presents experimental and analytical work demonstrating the significance of RA stability on RCF performance. Varying levels of retained austenite (RA) are achieved through varying undercooling severity in uniformly treated case carburized 8620 steel. Specimens are characterized via XRD and EBSD techniques to determine RA volume fraction and material characteristics prior to rolling contact fatigue (RCF). Higher RA volume fractions did not lead to improvement in RCF lives. XRD measurements after RCF testing indicated that little RA decomposition had occurred during RCF. A continuum damage mechanics (CDM) finite element model (FEM) is then developed to investigate the effects of RA stability on RCF.

Utilizing the CDM FEM, a parametric study is undertaken to examine the effects of RA quantity, RA stability, and applied pressure on RCF performance. The study demonstrates that the energy requirements to transform the RA phase is critical to RCF performance.

CHAPTER 2. A NOVEL APPROACH FOR MODELING RETAINED AUSTENITE TRANSFORMATIONS DURING ROLLING CONTACT FATIGUE

2.1 Introduction

Steels undergo many different types of heat treatments in order to achieve required material properties for specific applications. When steels are subjected to rolling contact fatigue (RCF) (e.g. cam and followers, bearings, etc.) hardness is considered to be one of the most important material properties. In order to achieve high hardness, steels are rapidly quenched from high temperatures in order to form martensite from the parent austenite phase. As a consequence of the high cooling rates, some austenite becomes entrapped inside the steel microstructure, commonly referred to as retained austenite (RA). These steels typically undergo subsequent heat treatment processes to temper the otherwise brittle steel and decrease the amount of RA which can be as high as 40 percent near the surface.

The steel microstructure can be considered as a heterogeneous material with RA having a lower yield strength than the surrounding matrix [34]. Anoop et al. [35] developed a model to characterize the material properties of 52100 steel as a function of RA concentration. The effectiveness of such a model is apparent in static loading conditions but not applicable for fatigue considerations as material microstructures evolve due to continuous periodic loading [36–40].

Microstructural evolution caused by cyclic loading has been a topic of interest for the past fifty years. It is well known that SAE 52100 through hardened bearing steels undergo a microstructural morphology when subjected to RCF. The first stage is the development of the dark etching region (DER). The DER is observed directly under the raceway in rolling element bearings and is termed as such due to its dark contrast during optical examination when etched with 2% nitric acid. However, no definitive answer can be given as to what causes this phenomenon but many agree that the DER represents martensitic decay [8, 9]. Some have concluded that DER initiation begins at the depth of maximum (unidirectional) shear stress [43] and then propagates throughout the depth. Oila [44] observed DER initiation along parent austenite grain boundaries in helical gears.

Smelova et al. [38] recently applied electron microscopy and nanoindentation to investigate material variations within 52100 steel microstructure due to RCF. They observed a reduction in

material hardness from 10 GPa (Nano Berkovich hardness) to 7.5 – 7.9 GPa in the DER region. Through secondary and backscattered electrons, they identified elongated and globular ferritic grains appearing within the martensitic structure as the cause of material softening. This observation provides the strongest evidence of DER formation due to martensitic decay. Additionally, they provided EBSD maps spanning areas of both the DER and unaffected region. Theses maps demonstrate a dramatic reduction of austenite within the DER compared to the unaffected region. The relationship between the DER and austenite is of particular interest for the current topic as it links martensitic decay or weakening of the microstructure with the phenomenon commonly referred to as RA transformations or decomposition.

The entrapped RA exhibits metastablilty at ambient temperatures and will therefore undergo a phase transformation provided sufficient energy. Researchers have observed the occurrence of an immediate transformation when a free surface was introduced to a grain of RA [45]. Accompanying these transformations is a volume expansion of approximately 3-5 percent. The volume expansion is the resultant of RA shifting from the face-centered cubic lattice structure to a martensitic body centered tetragonal or body centered cubic structure. Some researchers have concluded that high amounts of RA within a microstructure induces desirable residual stresses and will therefore improve fatigue resistance [11–13,46,47]. However, in order to reduce dimensional complications related to volumetric expansion within the material, the RA concentration is typically limited to less than 10 percent.

The phase transformation of RA within the steel microstructure occurs without atomic diffusion, known as a martensitic transformation. Martensitic transformations are thermodynamically driven phenomenon requiring a sufficiently large driving force. In the case of RA transformations, this driving force is typically provided by undercooling the system. As the temperature decreases, the Gibbs free energy of the austenitic phase increases [48]. It is the difference between Gibbs free energy of the austenite and the martensite or ferrite phase that constitutes the thermodynamic driving force necessary to cause the RA to transform [49].

Both theoretical and experimental work has been conducted to determine the necessary driving force for RA to transform. Singh and Parr [50] experimentally measured the driving force necessary for RA transformation as 300 ± 70 cal/mol in pure iron. Investigations into Fe-C systems found that initial transformations occurred from a driving force of 290 cal/mol [21, 22]. Nishiyama [53] agreed that 290 cal/mol would satisfy theoretical estimates for the chemical free

energy and therefore constitute a sufficient driving force to cause the transformation in Fe-C systems. Please note that this value is subjective as the energy requirements are affected by other factors such as austenitic grain size and alloying elements [54–56].

Cryogenic treatment of hardened steels has been investigated as a means to eliminate all RA within the microstructure. Zhirafar et al. [19] compared conventionally heat treated 4340 steel to 4340 steel which was held at -196° C for 24 hours prior to tempering. They found a drop from 5.7% to 4.2% comparing the conventional to the cryogenic treatment. Thus despite a significant temperature reduction, which would constitute a large driving force, much of the RA persists within the microstructure. Thus the transformation of RA requires an increasing amount of energy as less RA is present within the material.

Although undercooling is typically the energy source for phase transformations, Patel and Cohen [28] demonstrated that applied stresses can facilitate or hinder transformations. Shearing and tensile stresses will enable transformations by decreasing the necessary driving force while compressive stresses increase the energy required for transformations. Furthermore, Voskamp et al. [42] provided experimental results demonstrating RA decomposition at a constant temperature as a function of depth and cycle in 52100 steel for deep groove ball bearings. Dommarco et al. [12] was able to demonstrate similar results in 52100 steel utilizing a modified 3 ball and rod testing apparatus. Distinguishing between bulk and lathe or film RA, Park et al. [57] observed phase transformations in steel as a function of strain. They demonstrated that bulk type RA, typically larger than lathe and situated between or inside ferrite grains, more readily transforms compared to lathe type distributed along martensitic grain boundaries. Therefore energy requirements for transformation are greatly influenced by the strength and hardness of the surrounding matrix.

Few models exist to predict RA transformations due to mechanical loading. Available models simplify the phenomenon by considering only one-dimensional static loading [30, 31]. Models under these conditions have been useful, however cannot be applied to fatigue loading conditions.

This chapter presents a novel modeling approach for predicting RA transformations as a function of depth and cycle based on an energy criterion. The approach utilizes continuum damage mechanics to predict microstructural alterations induced by fatigue loading, in particular RCF. The current model does not incorporate the effects of material defects. Additionally, residual

stresses induced by RA transformations will not be considered as this model is only concerned with modeling until the transformation and residual stresses occur afterwards. The results obtained from the model for RA decomposition as a function of depth and cycle qualitatively compare well with the experimental results for 52100 steel.

2.2 Model Description

The proposed model considers RA as a soft inclusion entrapped within the significantly harder and stronger steel matrix. This entrapped RA is capable of martensitic transformation given an adequate driving force. Our assertion is to attribute the driving force required for martensitic transformations to the energy necessary for the RA to overcome the surrounding matrix in order to provide the appropriate volume expansion for the transformation.

In thermodynamic terms, the steel matrix halts the needed volume expansion by performing work on the RA phase. Therefore, the model developed for this investigation, considers the deterioration or decay of the steel microstructure as a reduction to the work energy available in the steel matrix to halt the transformation. The continuum damage mechanics approach is implemented to characterize work energy lost within the steel matrix. The loss of work energy is used in conjunction with a stress-assisted transformation mechanism to determine when energy requirements for RA transformations are met. The transformation process and modeling approach developed for this investigation is applied to the specific case of SAE 52100 through hardened steel in order to corroborate analytical and experimental results. However, the analysis is general and can be applied to other steel types.

2.2.1 Damage Mechanics

The field of continuum damage mechanics represents the degradation of materials by an internal state variable D. Material degradation is a thermodynamic phenomenon described by a state potential function and a dissipative function. The state potential function defines the total energy within the system while the dissipative function describes the evolution of energy from a useful to non-useful form. A mechanical representation of the state variable D is defined as;

$$D = \frac{S_D}{S} \tag{2.1}$$

where S is the total cross-sectional area of some arbitrary plane in the material and S_D is the area of voids lying on that plane. .Lemaitre describes the state potential and dissipative functions respectively as follows [32, 33]

$$\Psi^* = \Psi_e^* + \frac{1}{\rho}\sigma_{ij}\epsilon_{ij}^p - \Psi_P - \Psi_T \tag{2.2}$$

$$F = F\left(\sigma, r, X_{ij}, Y_{ij}, D_{ij}, T\right) \tag{2.3}$$

where Ψ^* is the Gibbs specific free enthalpy term deduced from the Helmholtz free energy by partial Legendre transform on the strain. Ψ_e^* is the elastic contribution affected by the damage parameter; σ_{ij} and ϵ_{ij}^P are the corresponding stress and plastic strain respectively. Ψ_T is defined as the temperature contribution while Ψ_P is defined as

$$\Psi_P = \frac{1}{\rho}\left(\int R dr + \frac{1}{3} C \alpha_{ij}\alpha_{ij}\right) \tag{2.4}$$

Here, R is the associated variable for isotropic hardening, α_{ij} is the back stress, and C is the material parameter representing the linear portion of the kinematic hardening. In the case of isotropic damage accumulation, the elastic contribution is defined as

$$\Psi_e^* = \frac{\sigma_{eq}^2 R_{VE}}{2E(1-D)} \tag{2.5}$$

where σ_{eq}, R_{VE}, and E are the von Mises equivalent stress, the triaxiality function and Young's modulus, respectively.

$$R_{VE} = \frac{2}{3}(1+\nu) + 3(1-2\nu)\left(\frac{\sigma_H}{\sigma_{eq}}\right)^2 \tag{2.6}$$

Damage mechanics quantifies the dissipation of energy from a useful state, work, to a non-useful state, entropy. In the context of the austenite phase trapped within a steel microstructure, the degradation of the surrounding matrix is a decrease in the energy available within the steel matrix to halt the martensitic transformation. Therefore, the intent is to find the change in available work energy or $\Delta\Psi^*$ in the steel matrix and equate this to a reduction of the barrier energy or driving force needed for the austenite to transform. Thus if the steel matrix has lost a sufficiently large amount of work energy, the RA transformation will spontaneously occur without further provocation.

By considering a steady state condition at constant temperature, $\Delta\Psi_T$ is zero and thus the equation reduces to;

$$\Delta\Psi^* = \Delta\Psi_e^* + \frac{1}{\rho}\Delta\sigma_{ij}\Delta\epsilon_{ij}^p - \Delta\Psi_P \tag{2.7}$$

This relationship was implemented to predict RA transformations. Due to the availability of RCF experimental results, SAE 52100 steel was chosen as the case study for evaluating the modeling procedure. Rubin et al. [61] demonstrated that SAE 52100 steel subject to RCF undergoes kinematic hardening without isotropic hardening. Therefore, in the current study, the isotropic hardening parameter R in equation (2.4) is neglected thus reducing the $\Delta\Psi_P$ term.

2.2.2 Damage Accumulation

The state and dissipative functions from damage mechanics establish an energy criterion to predict phase transformations within the microstructure. However, the objective is to model RA decomposition as a function of both depth and cycles. Therefore, additional equations are needed to calculate the damage rate in the material with respect to cycles and the subsurface stress state. Xiao [62] developed an equation for high cycle fatigue that relates the rate of damage with respect to cycles as follows.

$$\frac{dD}{dN} = \left[\frac{\Delta\sigma_{eq}}{M(\sigma_m)(1-D)}\right]^{2q} \tag{2.8}$$

Here, $\Delta\sigma_v$ is the range of the von Mises stress over a single stress cycle. M, q, and σ_m are material specific parameters found via fatigue testing. Raje et al., Bomidi et al., and Slack et al. [63–65] have used this fatigue equation successfully to predict life for different RCF loading conditions. In the case of RCF, it is generally accepted that the rolling contact fatigue phenomenon is a shear driven process. As fully reversible loads are considered to be the most detrimental to fatigue life and experimental observations have indicated initial failure at or near the depth of maximum orthogonal shear stress, this led to a modification of damage equation (2.8).

$$\frac{dD}{dN} = \left[\frac{\Delta\tau}{\tau_r(1-D)}\right]^m \tag{2.9}$$

This modified form is derived by replacing the von Mises criteria with the range of orthogonal shear stress ($\Delta\tau$) over a single stress cycle. τ_r and m are material specific parameters established from torsional fatigue experimentation. This modified damage law has been implemented in multiple RCF modeling procedures [10,64,66–68]. Equations (2.8) and (2.9) can be used to calculate the energy dissipation in the material microstructure as a function of stress cycles.

2.2.3 52100 Steel Material Parameters

Having established a method by which RA transformations can be predicted, a specific material must be selected to compare analytical and experimental results. SAE 52100 through hardened steel was chosen as the case study because of the experimental results available in the open literature.

As previously described, the damage rate equations (2.8, 2.9) require material specific parameters. The evaluation of these material parameters requires experimental stress life (S-N) data. Bomidi et al. [69] demonstrated that a power law in the form of equation (2.10) can be used to fit the experimental results for the case of fully-reversed shear loading;

$$\frac{\Delta\tau}{2} = AN_f^b \tag{2.10}$$

where N_f is the number of cycles to failure at the range of shear stress $\Delta\tau$ with A and b being constants of the line fit. Integrating equation (2.9) from an undamaged state ($D = 0$) to a fully damaged state ($D = 1$);

$$\int_0^{N_f} dN = \int_0^1 \left(\frac{\tau_r(1-D)}{\Delta\tau}\right)^m dD \rightarrow N_f = \frac{1}{1+m}\left[\frac{\tau_r}{\Delta\tau}\right]^m \tag{2.11}$$

Comparing equations (2.10) and (2.11) results in the following relationships;

$$m = -\frac{1}{b} \tag{2.12}$$

$$\tau_r = 2A\left(1 - \frac{1}{b}\right)^{-b} \tag{2.13}$$

Jalalahmadi et al. [67] provides a thorough explanation of this process. Given the experimental results by Bomidi et al. [69], where $A = 2.39$ and $b = -0.09$, equations (2.12) and (2.13) result in $m = 11.1$ and $\tau_r = 5.98$ for SAE 52100 steel subjected to fully reversed shear stress.

Applying similar principles, the σ_r can be derived from the available data by recognizing the relationship between the shear stress reversal ($\Delta\tau$) and von Mises stress (σ_v) in materials subjected to pure shear. Based on the Mohr's circle and the definition of von Mises stress, for a material in pure shear;

$$\frac{\Delta\tau}{2} = \tau_{max} \tag{2.14}$$

$$\sigma_{eq} = \sqrt{3}\tau_{max} \tag{2.15}$$

Therefore combining equations (2.14) and (2.15);

$$\Delta\tau = \frac{2\sigma_{eq}}{\sqrt{3}} \tag{2.16}$$

Following a similar process as before, integrating equation (2.8) from an undamaged condition to a fully damaged condition results in;

$$\int_0^{N_f} dN = \int_0^1 \left\{\frac{\sigma_r(1-D)}{\sigma_{eq}}\right\}^m dD \tag{2.17}$$

$$N_f = \frac{1}{m+1}\left[\frac{\sigma_r}{\sigma_{eq}}\right]^m \tag{2.18}$$

Substituting equation (2.16) into (2.10) and comparing to equation (2.18) gives

$$\frac{1}{m+1}\left[\frac{\sigma_r}{\sigma_{eq}}\right]^m = \left(\frac{\sigma_{eq}}{\sqrt{3}A}\right)^{\frac{1}{b}} \tag{2.19}$$

$$m = -\frac{1}{b} \tag{2.20}$$

$$\sigma_r = \frac{\sqrt{3}A}{\left(1-\frac{1}{b}\right)^b} \tag{2.21}$$

As before, $m = 11.1$ while $\sigma_r = 5.18$ for SAE 52100 steel considering von Mises stress as the cause of damage within the material.

2.2.4 Driving Force Variation

Zener [51] and Cohen et al. [52] measured 290 cal/mol as the necessary driving force to produce initial martensitic transformations in Fe-C systems. This value varies based on the applied stress, the crystal orientation [28], and the surrounding material composition. For the specific case of 52100 through hardened steel, alloying elements such as Chromium, Manganese and Silicon will directly affect the driving force required for RA to transform. However, lacking experimental measurements of the exact driving force needed in 52100 steel, the effect of alloying elements was

not considered in this modeling. Instead, the measured driving force for a generic Fe-C system was considered as an approximation for 52100 steel.

An important consideration in stress-assisted martensitic transformations is the orientation of the habit plane. The habit plane is the interface plane between the parent austenite phase and the martensite. Unique to this plane is the lack of lattice distortion due to the martensitic transformation. Patel and Cohen [28] demonstrated that shear stresses resolved on habit planes will facilitate martensitic transformations while normal stresses will either facilitate or inhibit the transformation depending on the directionality. They found that compressive stresses will increase the required driving force thus impeding transformations while tensile stress normal to the habit plane will decrease the required energy for RA transformations.

To incorporate the effect of habit planes, crystal orientations are randomly assigned to each element within the model. For SAE 52100, the habit planes are approximated as [2,2,5] using miller indices [70]. Shear and normal stresses are then resolved along habit planes based on the assigned crystal orientation. These resolved stresses then directly modify the driving force required for RA to transform. The miller indices [2,2,5] can be represented by multiple equivalent planes within a given crystal lattice orientation; therefore only the plane that most reduces the required driving force is considered as the habit plane for the specific crystal orientation.

Aside from the crystal orientation, the required driving force is also a function of RA present within the material. This is most clearly demonstrated from results produced by Zhirafar et al. [19] and Park et al. [57]. In order to capture this phenomenon within the model, as the volume fraction of austenite decreases towards zero, the energy requirement is modified by an assumed relationship of the initial volume fraction of austenite divided by the current volume fraction of austenite present $\left(\frac{V_{f,initial}}{V_f}\right)$. This is applied to represent increasing energy requirements for transformations as less RA is present in the material. The increase in energy requirements for transformations is at a rate less than the growth of available energy due to material damage, therefore the increased energy requirements do not forbid RA transformations as volume fractions approach zero.

2.3 FEM Model of Rolling Contact Fatigue

Modeling RA decomposition can be achieved by considering the localized driving force present at different points throughout the material. This driving force is a function of the damage accumulation and resolved stresses along crystalline habit planes, both of which are functions of the stress state. Therefore, a two-dimensional FEA model was developed to capture the complex subsurface stress state induced by rolling contact fatigue.

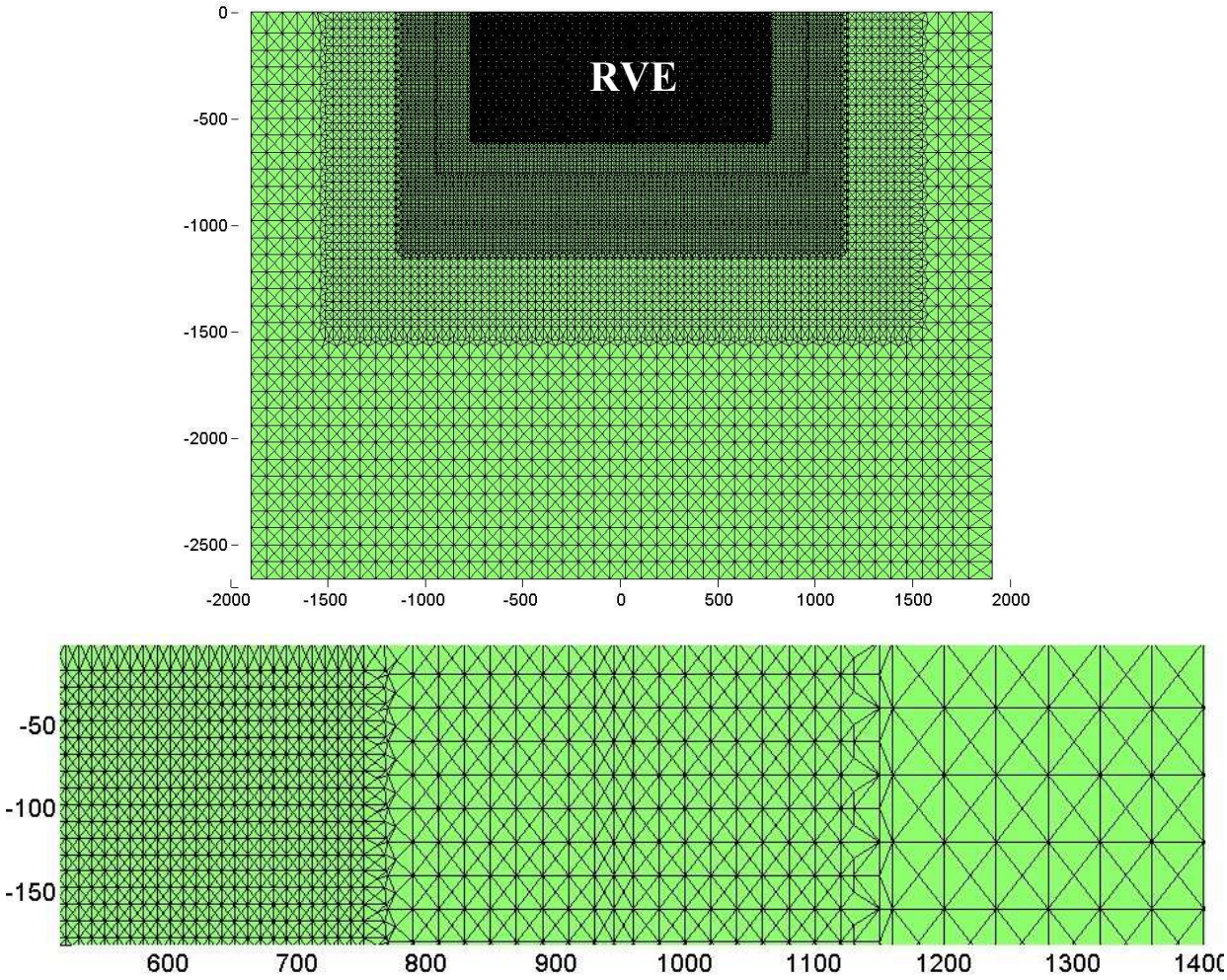

Figure 2.1: a) Depiction of 2D finite element domain. b) Magnification of finite element mesh to demonstrate mesh refinement nearing the RVE

Figure 2.1 depicts the domain developed for this investigation. The domain is $10b$ by $7b$ in the width and depth, respectively, comprised of constant strain triangular elements, where b is half the width of the Hertzian contact in the rolling direction. The representative volume element (RVE) is the region from -3b to 3b with respect to the x direction and 0 to –1.57b in the y direction. Boundary conditions were enforced along the bottom surface by setting the displacement in the x and y directions to zero. The area of interest in the model is from -0.5b to 0.5b in the x direction and 0 to -1.57b in the y direction. The domain dimensions are sufficiently large to produce stresses in the area of interest comparable to a Hertzian pressure profile being passed over a semi-infinite domain. To reproduce RCF loading conditions in the area of interest, a Hertzian pressure profile was moved from left to right along the upper surface of the RVE from -3b to 3b in 81 discrete steps. The developed FEA model closely mirrors previous rolling contact models [10,64,67,68,71].

In order to incorporate material effects due to austenite concentration, a random function generator was used to assign an austenite volume fraction to each element within the RVE. The procedure further ensures that the aggregate volume fraction of austenite within the domain is comparable to reported levels in experimental data. Figure 2.2 presents the RA volume fraction assigned throughout the RVE. The scale depicted in Figure 2.2 assigned red to the highest RA concentration (~12.5%) and blue to the lowest (~0%).

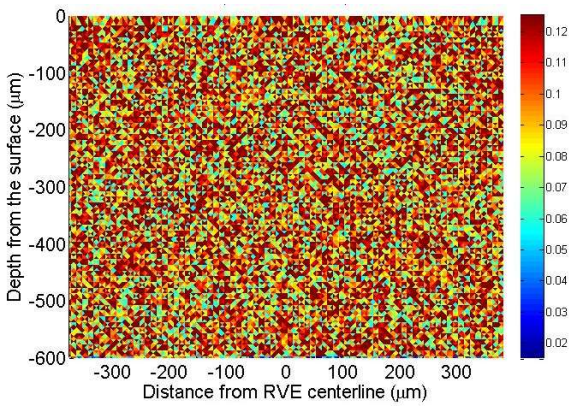

Figure 2.2: Initial local RA assignments throughout the RVE for an average RA concentration of 10%. Scale is relative to the maximum RA assignment 12.5%.

Via an assigned state variable, the volume fraction at each location within the domain is used in ABAQUS to modify element specific material properties. For simplicity, a Voight or rule of mixtures solution [72] is applied to calculate the yield strength for each element similar to previous modeling of RA in 52100 steel [35].

$$S_y = V_f * S_{ya} + \left(1 - V_f\right) * S_{ym} \tag{2.22}$$

where $V_f, S_{ya},$ and S_{ym} are the volume fraction of austenite, yield strength of austenite and yield strength of the matrix, respectively. In order to compare with the experimental data presented by Voskamp [42], the yield strength and modulus of elasticity are needed for both the austenite and matrix of 52100 steel. Hatem [34] provides material properties for the austenitic phase while Shimizu [73] has conducted extensive material testing on 52100 steel. Table 2.1 contains the material properties used in this investigation. Additionally, elemental material parameters were modified as a function of RA decomposition to represent material softening occurring within the DER. To the best knowledge of the authors, experimentally determined values for the DER yield strength and Young's modulus are not available. Therefore, reasonable estimates for the final yield strength and Young's modulus $\left(E = 180GPa, S_y = 1.8GPa\right)$ of the fully developed DER were assumed based on hardness measurements. Using the initial values of E and S_y for the steel matrix and final DER, a linear relationship between local RA decomposition and local material softening was imposed in the model.

Table 2.1: Material Properties of Austenite phase and 52100 steel matrix

	Austenite	**52100 steel**
E	200 GPa	205 GPa
S_y	367 MPa	2030 MPa

Because of the high localized stresses due to rolling contact pressures, the effect of plasticity must be considered within the model. As previously described, Rubin [61] demonstrated that fatigue loading causes kinematic hardening in SAE 52100 steel. In order to introduce kinematic hardening into the material model, the ABAQUS simulation is initially conducted

without considering damage or RA decomposition. This allows localized yielding and strain hardening to occur within the material. The simulation is continuously updated during this process until a steady state condition is reached where plastic yielding ceases. After achieving steady state, stresses are then extracted from the ABAQUS simulation and input into a Matlab function where localized damage is calculated as a function of cycles. The state of stress and amount of damage at each element is implemented within the energy criteria to calculate RA decomposition. The Matlab function increases the number of cycles while continuously determining the RA decomposition until a threshold value of RA decomposition is reached. Updated volume fraction values of RA are then returned to ABAQUS for further simulation to extract modified stress states within the material. This procedure continues until a desired limit of total RA decomposition within the RVE is reached.

2.4 Results and Discussion

The FEA modeling and analysis for RA decomposition in 52100 steel was performed with the material parameters extracted from the experimental life data for 52100 steel in fully reversed shear loading. The analysis was completed by employing both the von Mises and orthogonal shear damage accumulation criterions individually. The ABAQUS FEA model developed was used to corroborate with the experimental loading and geometric conditions provided by Voskamp et al. [42].

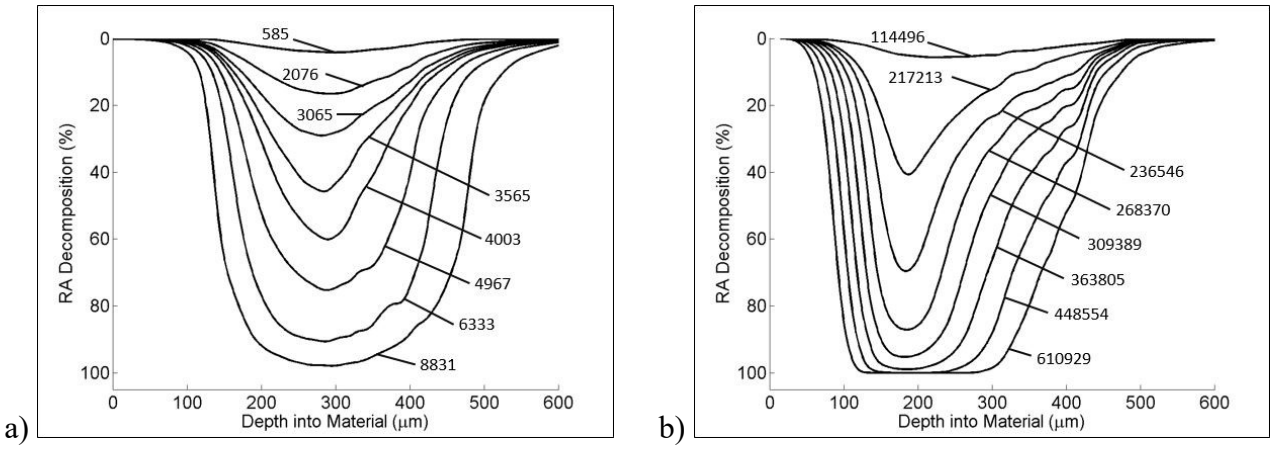

Figure 2.3: RA decomposition with respect to depth under the condition of a) von Mises stress and b) orthogonal shear inducing damage, equation (2.8) and (2.9). The plotted lines represent the RA decomposition in the microstructure at the different number of cycles provided.

Figures 2.3a and 2.3b depict the analytical results for RA decomposition with respect to depth and cycle. Each line on the Figure represents the amount of RA decomposition with respect to depth at a specific moment during the simulation. The cycle count is used to define when the RA decomposition verses depth was recorded during the simulation. These results were obtained by implementing the proposed energy criteria in conjunction with the FEA model. Figures 2.3a and 2.3b, were obtained by using the orthogonal shear and von Mises damage accumulation, respectively. The simulation was performed at an RA volume fraction of ~10% subjected to a maximum Hertzian pressure of 3.2 GPa with a half-width of contact, b, equal to 190 μm. The results shown in Figure 2.3 are compared to Figure 2.4 which illustrates Voskamp et al.'s [42] experimental results of RA decomposition as a function of depth and cycle in 52100 steel with a similar RA volume fraction and loading condition.

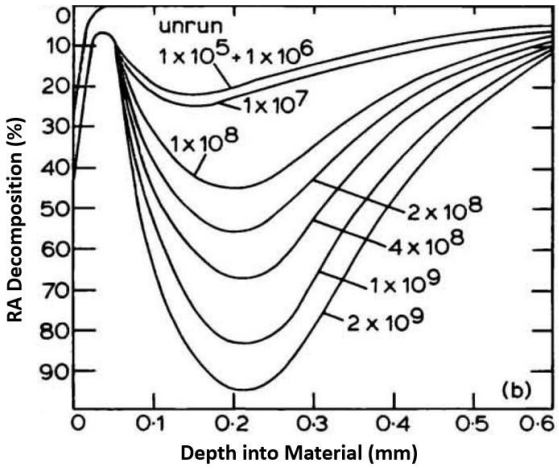

Figure 2.4: RA Decomposition as a function of depth and cycles. Results provided by Voskamp et al. [42] from 52100 steel deep-groove ball bearings.

Both the orthogonal shear and the von Mises criterion capture the overall shape as represented by the experimental results of Voskamp et al. [42]. The orthogonal shear criterion more accurately captures the location of the initial RA decomposition while the von Mises criteria is able to better capture the decomposition occurring further into the material. This comparison suggests orthogonal shear as the primary cause of material degradation and therefore RA transformations in rolling contact fatigue.

In the current modeling, trends in the overall decomposition caused by the orthogonal shear criterion as a function of depth were found to be in good agreement with experimental results. The

analytical model predicted the depth for maximum RA decomposition as observed in experimental results. Additionally, the modeling was correctly able to produce results that asymmetrically favored RA transformations at greater depths compared to superficial material layers. It is noted that analytical results deviate from experimental results at depths greater than 0.5 mm.

Cycle counts produced by the proposed model differed from those reported by Voskamp et al. [9]. This deviation is attributed to a lack of experimental data for RA transformations. As previously discussed, parameters $m,\ \tau_r,\ \sigma_r$ are material specific parameters applied within the damage accumulation equations to determine the rate of damage with respect to cycles. These material parameters were estimated from torsional fatigue life data. This is considered an appropriate approximation in order to introduce the proposed energy criteria presented in this investigation; however, fatigue experiments should be performed to improve model accuracy. The experiments need to measure RA decomposition as a function of cycles at various stress states. The data for RA decomposition with respect to cycles could then be curve fitted with a power law in accordance with the principles introduced to extract material parameters as done previously with the torsional fatigue data. This would then allow the extraction of the $m,\ \tau_r$, and σ_r specific to RA transformations.

Although approximate material parameters (m, τ_r, σ_r) are considered the primary cause of differing cycle counts, deviations in cycle count may also be attributed to the use of 290 cal/mol as the required driving force for RA transformations in 52100 steel. The value of $\Delta\Psi^*$ implemented in the model is for a generic Fe-C system and not specific to the 52100 steel composition which will be affected by the alloying elements: Cr, Mn, Si, S, P. Furthermore, material properties E and S_y for the DER were obtained based on the experimental hardness measurements. The values of E and S_y will alter subsurface stress states and therefore the rate of damage accumulation with respect to cycles.

Model parameters $(\tau_r, \sigma_r, m, \Delta\Psi^*, E, S_y)$ can be determined experimentally and employed within the model to better reflect RA decomposition with respect to cycles. In order to demonstrate the large effect model constants have on cycle prediction, all material parameters and properties except m were held constant for the condition of orthogonal shear induced damage. Figure 2.5 presents the results of the simulation employing $m = 17$ as the material parameter. The modification of the m parameter slightly affected the observed pattern of RA decomposition;

however, the cycle count was greatly influenced by the alteration of the m parameter. This result provides a clear demonstration of how material parameters greatly affect cycle predictions.

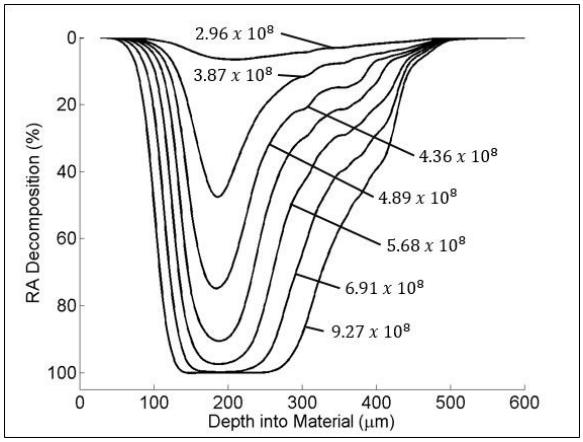

Figure 2.5: RA decomposition under the condition of orthogonal shear inducing damage with material parameter m=17.

Having observed good agreement between the analytical and experimental results for RA decomposition with respect to depth, the modeling procedure was utilized to examine the effects of RA concentration and distribution. Applying only the orthogonal shear stress criteria, the model was used to examine additional conditions of 20% and 35% RA randomly dispersed within the RVE. Figures 2.6a and 2.6b present the results for the 20% and 35% RA simulations, respectively. Furthermore, two additional cases were considered to examine the effects of RA distribution by linearly distributing the RA as a function of depth. In the first case, the maximum value of RA (35%) was assigned to the surface and was linearly decreased to 0 at a depth of 0.6 mm. In the second case the maximum was assigned at a depth of 0.6 mm and linearly decreased to 0 at the surface. Figures 2.7a and 2.7b show the results of RA transformation for the two different cases considered.

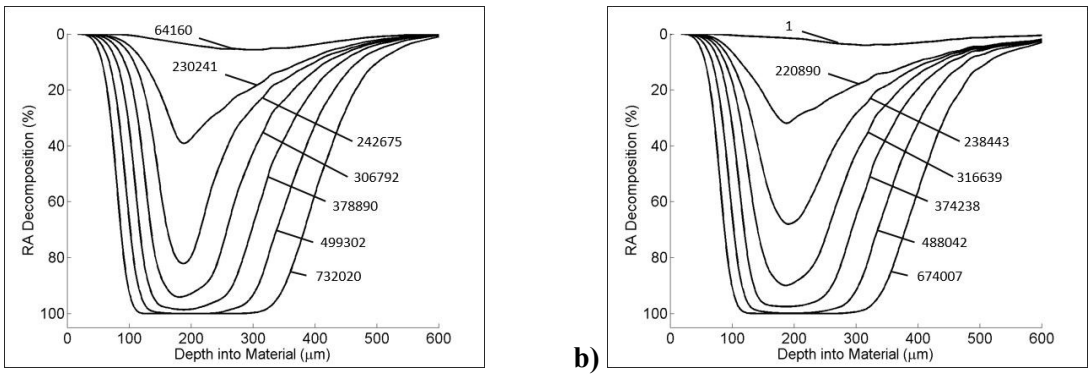

Figure 2.6: Results for RA decomposition of a) 20% and b) 35% RA randomly distributed throughout the microstructure applying the shear criteria.

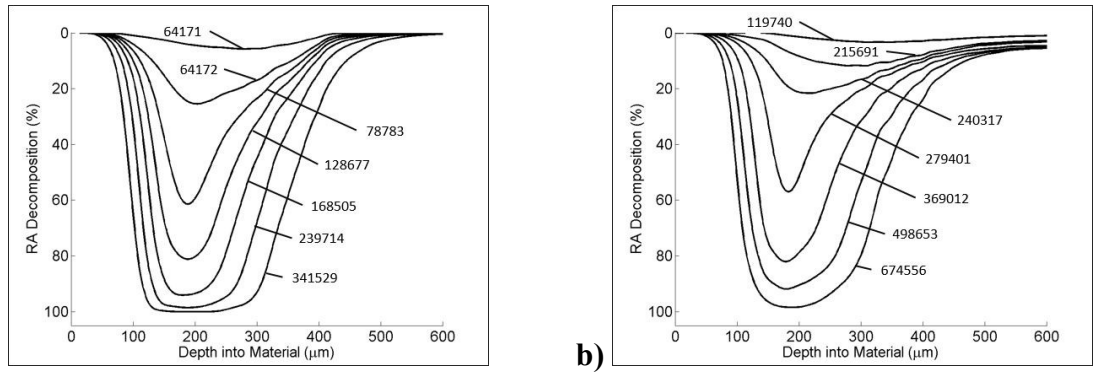

Figure 2.7: Results for RA decomposition for case of linear distribution with respect to depth. a) 35% assigned to surface and 0% assigned at 0.6 mm. b) 0% assigned to surface and 35% assigned at 0.6 mm.

When high levels of RA exist in the microstructure, RA decomposition occurs more readily without the need for material deterioration as seen in Figures 2.6a and 2.6b. From a microstructural stand point, this is expected as RA is a softer phase of the material and more RA will decrease the overall matrix strength. Thus less energy is required to overcome the surrounding matrix to enable RA transformations. Additionally, the material as a whole will be subjected to greater plastic deformation which further induces RA transformations.

Martensitic steels will typically have a high concentration of RA near the surface which gradually diminishes with increasing depth into the material. The distribution of the RA greatly affects RA decomposition with respect to cycles as demonstrated by Figures 2.7a and 7b. Typically, RA decomposition gradually occurs over many stress cycles, however, in the case of

high RA concentration at near the surface this does not occur. As shown in Figure 2.7a, two of the lines representing the amount of RA decomposition within the RVE at different times during the simulation are separated by a single load cycle. This signifies that additional material degradation was not necessary and the available energy provided by the applied stresses was sufficient to enable a large amount of RA transformations without the need for additional material degradation. This is caused by a high RA concentration near the surface which creates a less rigid material in close proximity to the highest stresses; therefore, RA decomposes rapidly in this region. Conversely, initial RA decomposition, as shown in Figure 2.7b, required significantly more cycles compared to the simulation for Figure 2.7a. This again is explained by having a low concentration of RA near the surface. The material is stronger and more rigid in the absence of RA at the locations of highest stress. Therefore the increased cycle count is due to both the improved material resistance to plastic deformation and the distance of the majority of RA from areas of high stress.

2.5 Combined Criteria

The modeling approach described in the previous sections has only considered the orthogonal shear or the von Mises stresses separately. As previously discussed, the orthogonal shear stress criteria produced results which are in better agreement with the experimental observation, however, material degradation may be a function of both damage criteria. Therefore, further simulations were performed which consider both the orthogonal shear stress and the von Mises damage criteria simultaneously.

To consider both criteria simultaneously, the rate of damage as a function of cycles was calculated for both criteria at every location throughout the RVE. The highest damage rate at each location was then applied to determine available energy as in previous simulations. The analysis considering both criteria simultaneously was first completed utilizing the material parameters as previously established for 52100 steel. Figure 2.8a illustrates the results of the analysis considering both criteria simultaneously while applying material parameters: $\tau_r = 5.97$, $\sigma_r = 5.17$. This produced results identical to simulations which only considered the von Mises damage criteria. This signifies that the von Mises criterion is dominating at every location throughout the domain given the current material parameters. However, experimental observation indicates that more RA decomposition occurs near the depth of maximum orthogonal shear as compared to the

depth of maximum von Mises stress. Thus, orthogonal shear is considered to be more detrimental to material degradation.

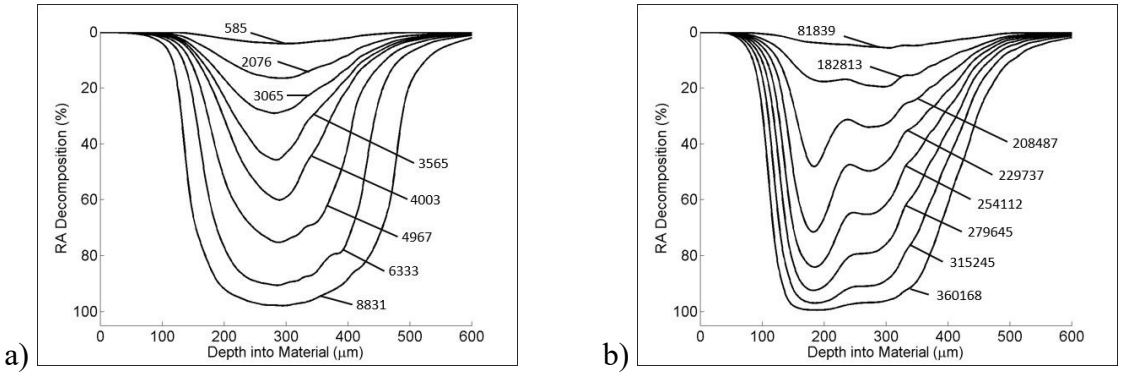

Figure 2.8: Results of RA decomposition when applying both damage laws simultaneously.

Therefore, varying the material parameters (τ_r, σ_r) would allow the orthogonal shear to be dominate at certain locations while the von Mises would be dominate elsewhere. A parametric study was performed to determine if a simulation combining both criteria could produce better results than the use of any single criterion. Thus in the parametric study material parameter σ_r was varied, while maintaining τ_r constant. This effectively varies which criteria is considered at every location. Figure 2.8b depicts the results of the parametric study when $\frac{\tau_r}{\sigma_r} = 0.7654$. Applying this ratio between the orthogonal shear and von Mises stress produces RA decomposition as function of depth which closely matches the experimental results of Voskamp et al. [42]. This agreement with experimental results suggests that RA transformations are a function of both orthogonal shear and von Mises stress; however, the orthogonal shear has a more dominant effect on material degradation as compared to the von Mises stress.

2.6 Summary and Conclusion

In this chapter, a novel energy based criterion is proposed to predict the decomposition of retained austenite within martensitic steels. The approach is based on the experimental observations of induced microstructural evolution through rolling contact fatigue. Fundamental to the energy criterion is that some thermodynamic driving force is necessary to promote the

material transformation. This driving force was accounted for by considering work energy provided by cyclic loadings upon habit planes within the material and the energy dissipation or loss of useful work in the surrounding matrix. Thus a continuum damage mechanics modeling approach was developed to determine changes in the state potential and determine transformational driving forces.

The energy criterion developed was implemented within an FEA model to investigate RA decomposition for the specific case of 52100 steel. The analytical results were then compared to published results measuring RA decomposition in 52100 steel. The RA decomposition results obtained from the FEA modeling approach developed for this investigation were corroborated with experimental results in the open literature. The results are in good agreement with published experimental results as a function of depth and cycle. Improvements for a more accurate cycle prediction can be achieved provided experimental work to measure required material parameters $(\tau_r, \sigma_r, m, \Delta\Psi^*)$ specific to RA transformations in 52100 steel.

CHAPTER 3. EFFECT OF RESIDUAL STRESSES ON MICROSTRUCTURAL EVOLUTION DUE TO ROLLING CONTACT FATIGUE

3.1 Introduction

Materials subjected to fatigue are known to undergo microstructural alterations. The rolling contact fatigue (RCF) process which induces a high localized stress state produces especially prominent changes in bearing steels. Bearing steels are known for their extremely high hardness derived from their martensitic microstructure.

At high temperatures prior to quenching, steels are composed of the Face-Centered Cubic (FCC) phase austenite. As cooling occurs the austenite transforms into a Body-Centered Cubic (BCC) phase. Depending on the carbon composition, steels at room temperature will be composed of pure ferrite or a ferrite cementite composite. In the case of bearing steels, martensite in the microstructure is produced by extremely high quenching rates which cause a phase transformation to occur without allowing for atomic diffusion; this is also known as a martensitic transformation. The martensitic transformations do not allow carbon atoms to diffuse from interstitial positions resulting in an asymmetrically warped crystal structure known as Body-Centered Tetragonal (BCT). This structure is highly strained and by nature of the transformation process leads to high dislocation densities within the martensite. These characteristics of the martensitic structure produce the high hardness of the material.

An additional consequence of the extremely high quenching rates, is the presence of retained austenite (RA) within the steel microstructure. Austenite at room temperature can achieve a lower energy state via a phase transformation to a BCC structure. However, phase transformations from an FCC to a BCC or BCT structure necessitate a volume expansion of approximately 4 – 8% due to the comparatively higher atomic packing density of the FCC structure. Therefore, the hardened steel structure surrounding the retained austenite acts as an obstacle to the martensitic transformation by halting the needed volume expansion. This produces the metastable behavior of retained austenite. Researchers have confirmed this behavior by providing a free surface to specific grains of RA via focused ion-beam (FIB) milling and observing immediate martensitic transformations [45].

Despite the surrounding material, the RA will undergo a martensitic transformation provided a sufficient driving force. This driving force has been approximated as 300 cal/mol in Fe-C systems by the electrode potential method [50]. The necessary driving force for transformations to occur is typically attributed to undercooling of the system, however, deformation has been shown to stimulate martensitic transformations[30,56–58]. Work performed by Blondé et al. [74] observed RA transformations due to temperature and deformation. As temperatures were decreased, the energy provided by undercooling increased and the total amount of mechanically induced austenite to martensite transformations increased leading to a larger deformation prior to fracture.

52100 through hardened steel is a martensitic steel frequently used for rolling contact applications. For this reason, it has been the subject of many studies to characterize microstructural variation induced by RCF. After repeated rolling contact, the first major indication of microstructural changes is the appearance of the dark etching region (DER). Jones [75] was one of the first to report this phenomenon in bearings. Oila et al. [44] also observed the DER below the contact surface in helical gears. This study indicated DER initiation to occur along parent austenite grain boundaries at a depth corresponding to the location of maximum Von Mises stress. Researchers have concluded that the DER formation is an optical representation of the decaying martensitic structure [41,42,76].

Recently, Smelova et al. [38] performed electron microscopy and nanoindentation on specimens of 52100 steel subjected to rolling contact. The study observed the DER formation and through nanoindentation measured a softening of the material within the DER. Muro et al. [77] also observed this softening in the DER. These results support the idea that the DER is simply an optical representation of material deterioration due to cyclic loading. Additionally, electron back-scatter diffraction (EBSD) performed on these specimens by Smelova et al. [38] observed a sharp decrease in the amount of RA within the DER compared to other regions within the material.

Morris et al. [78] considered these results as the basis to propose an energy criteria to predict RA transformations due to RCF. The key assertion of the model is to attribute the required driving force for RA transformations to the loss of useful work energy in the surrounding material. The model achieved good agreement with experimental results of RA decomposition in 52100 steel as measured by Voskamp [42]. Although the modeling procedure achieved results that compared well with previous investigation, the procedure lacked consideration of residual stresses

(RS) developing within the material due to the phase transformations and the RCF process. RA transformations are known to induce compressive internal stresses between the original steel microstructure and the newly transformed phase [79].

The concepts of material degradation, RA decomposition, and RS formation are not independent phenomena. In order to obtain a better understanding of the microstructural response to RCF, all three processes must be considered simultaneously. Microstructural decay, phase transformations and internal stresses were implemented within a 2D FEA line contact model to investigate variation in microstructural alterations due to residual stresses present within the material. In order to verify the modeling procedure, initial simulations were performed using parameters and conditions extracted from experimental conditions and then directly compare to empirical measurements of RA decomposition and RS formation in 52100 steel deep groove ball bearings. Further simulations implemented various residual stress profiles induced by laser-shot peening or carburizing processes to compare the benefits of different initial RS states.

3.2 Energy Criteria for RA Transformations

As previously mentioned, the energy criteria proposed by Morris et al. is implemented in this model to predict RA transformations as a function of stress history and load cycles. This modeling approach requires a material specific energy to predict RA transformations. The material specific energy has been observed to vary due to chemical composition, grain size and material phase composition [54,55,57]. Due to the lack of experimental results identifying the specific energy criteria for 52100 steel, measurements by Zener [51] and Cohen et al. [52] of 290 cal/mol in FE-C systems are considered as a good approximation and as the default required driving force for 52100 steel's chemical composition. Due to the carbon concentration of 52100 steel (~1%), the martensite morphology is considered a mixture of lathe and plate martensite.

Work done by Parks et al. [57] utilized EBSD to observe changes in RA volume fraction due to an increasing strain. Two important outcomes of the study were that austenite undergoes incremental transformations as energy is available and areas of higher austenite volume fraction required less energy to induce transformations. Therefore, within the modeling approach used for this investigation, partial RA transformations are considered to occur as the energy becomes available. These transformations in turn create more constraint on the remaining RA thus increasing the required energy for further phase transformations.

Two available sources are considered to fulfill the energy requirement. The first being material deterioration or damage which decreases the amount of useful work available in the surrounding matrix to halt the required expansion for the FCC to BCC or BCT phase transformation. The second is a stress-assisted transformation phenomenon. Patel and Cohen [28] observed a relationship between the required driving force of RA transformations and the applied stress resolved on the habit planes. A tensile normal stress reduced the total energy requirement while a compressive normal stress increased energy requirements necessary for martensitic transformations to occur. Shearing stress, regardless of direction, reduced the total energy requirements for transformation. They proposed the following work equation to modify the energy requirement

$$U = \tau\gamma_0 + \sigma\epsilon_0 \tag{3.1}$$

where τ is the shear along the habit plane and σ is the normal stress perpendicular to the habit plane. γ_0 and ϵ_0 are the shear and normal components of the transformational strain which are approximately 0.2 [28] and 0.04 [80], respectively. Voothaluru et al. [81] verified this concept by observing preferential austenite transformations along planes of the highest resolved shear stress via in-situ neutron diffraction.

3.3 Development of Residual Stresses

Residual stresses are internal stresses that exist within a body without the application of some external force. RS arises due to misfit strains within the material [82]. These misfit strains are attributed to either non-uniform volume expansion or non-uniform plastic deformation. For the specific case of 52100 steel subject to RCF, non-uniform volume expansion occurs due to RA transformations while non-uniform plasticity is caused by the complex subsurface stress state.

Johnson [83] has provided extensive theoretical examination of residual stresses within an elastic-plastic half-plane subjected to rolling contact. Applying Hertzian theory with a Von Mises failure criterion, Johnson asserts that residual stresses will develop perpendicular to the contacting surfaces. Development of such RS would decrease the maximum Von Mises stress occurring during a load pass and initiate the second stage of RCF process known as shakedown.

Experimental work by Voskamp [79] demonstrated large compressive residual stresses developing perpendicular to the contacting surfaces.

3.4 FEM Model of Rolling Contact Fatigue

A finite element modeling procedure was developed to determine the evolving microstructure due to RCF. The modeling procedure is performed for 52100 through hardened steel. 52100 steel was chosen because of its frequent use in rolling contact scenarios and the availability of extensive experimental results. Details of the specific modeling procedure are provided below.

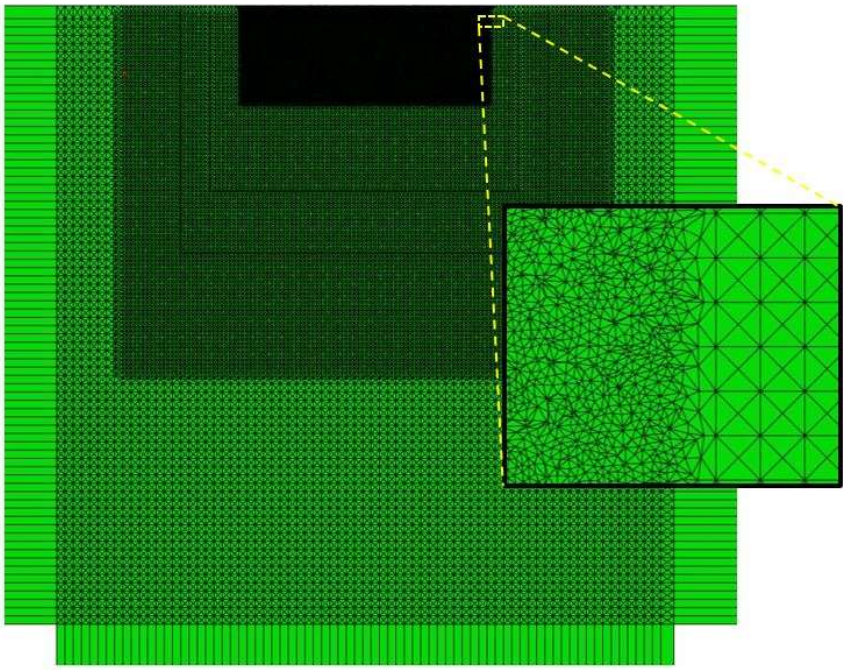

Figure 3.1: Depiction of 2D finite element domain

3.4.1 Two-Dimensional FEA Model

In ABAQUS, a semi-infinite domain constructed of infinite elements and constant strain triangular elements is used to determine stresses occurring within the material. Figure 3.1 depicts the domain developed for this investigation. The representative volume element (RVE) is the finest meshed region from -3*b* to 3*b* in the x direction and 0 to –1.57*b* in the y direction, where *b*

is the half width of the Hertzian contact. In order to simulate conditions similar to experimental results, b is set to 380 μm and P_{max} is 3.28 GPa. Infinite elements attached along the sides and bottom of the domain act as boundary conditions allowing for the implementation of residual stress along the rolling direction.

The area of interest in the model is from -0.5b to 0.5b in the x direction and 0 to -1.57b in the y direction. The domain dimensions are sufficiently large to produce stresses in the area of interest comparable to theoretical line contact on a semi-infinite plane. To reproduce RCF loading conditions in the area of interest, a Hertzian pressure profile is moved from left to right along the upper surface of the RVE from -2.2b to 2.2b in 81 discrete steps. The use of 81 steps allowed for close approximations of the stress history at all points throughout the domain while minimizing computational effort. The developed FEA model closely mirrors previous rolling contact models [10,64,67,68,71].

Stresses are extracted from the ABAQUS simulation and input into a Matlab function where localized damage is calculated as a function of cycles. The state of stress and the amount of damage at each element is implemented within the energy criteria to calculate RA decomposition. The Matlab function increases the number of cycles while continuously determining the RA decomposition and RS formation until a threshold value of RA decomposition is reached. Updated volume fraction values of RA and new RS values are then returned to ABAQUS for further simulation to extract modified stress states within the material. This procedure continues until a desired limit of total RA decomposition within the area of interest is reached.

3.4.2 Crystallographic Considerations

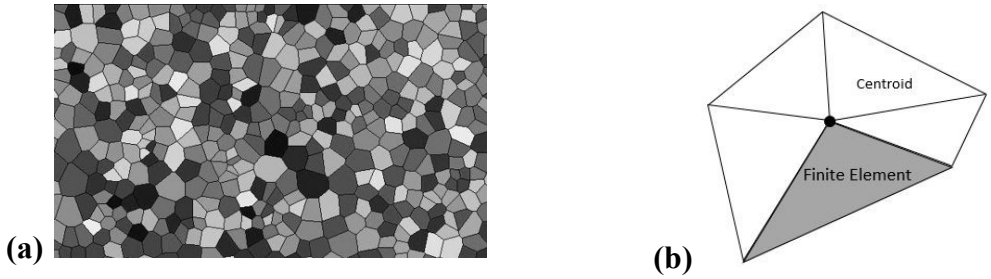

Figure 3.2: a) Voronoi tessellations representative of an austenitic microstructure. The average Voronoi diameter is 10 μm. b) Discretization of Voronoi tessellations to create finite element mesh.

As previously discussed, crystal orientation directly affects energy requirements for RA transformations and is therefore an important component of modeling material microstructures. Voronoi tessellations simulate observed microstructures and have been incorporated into modeling procedures [67,84,85]. These tessellations are generated via seed points or a finite and distinct set of points distributed within a plane. Areas of the domain are assigned to the closest corresponding seed point. This generates the Voronoi diagram representative of an austenitic steel matrix as shown in Figure 3.2a. Each tessellation is further discretized into finite elements to allow for a better stress state solution (Figure 3.2b).

Crystalline orientation is described using three Eulerian angles; from each angle a rotational matrix is created. The individual matrices are then multiplied together to create one rotational matrix representative of a XZX rotation. This provides all the information necessary to calculate energy requirements by resolving stresses along habit planes. The three Eulerian angles are assigned at random to each representative grain or Voronoi area and in turn all corresponding finite elements.

Habit planes are the interface between the parent austenite and martensite phase. By definition, these unique planes have no lattice distortion due to the transformation. In the case of 52100 steel, the habit plane is best approximated by the [2 2 5] plane [70]. Considering the [2 2 5] plane within an FCC crystal structure gives 24 equivalent planes but only six unique stress states after stresses were resolved. The resolved stresses were then implemented in Patel and Cohen's work equation to determine the most advantageous plane for RA transformation. All future work energy calculations are performed with respect to this plane.

3.5 Material Evolution

3.5.1 Material Deterioration

The RCF process brings about gradual material changes. Within this modeling procedure, material deterioration, RA transformations and RS formation are the three principle considerations. As previously described, damage is often represented by microvoids within the material. Equivalently, damage can be expressed as a deterioration of the material stiffness by introducing the concept of damage into the stress equation as follows.

$$\tilde{\sigma} = \frac{F}{\tilde{S}} = \frac{F}{S - S_D} = \frac{F}{S(1-D)} = \frac{\sigma}{(1-D)} \tag{3.2}$$

where F is some applied force, $\tilde{\sigma}$ is the effective stress in the material due to damage, and $\tilde{S}$ is the effective area of some plane within the material subjected to damage. Apply equation (3.2) to Hooke's law

$$\sigma = E(1-D)\epsilon \tag{3.3}$$

The effective modulus of a material subjected to damage is defined as

$$\tilde{E} = E(1-D) \tag{3.4}$$

This definition for the material stiffness is implemented within the ABAQUS simulation to represent the deterioration or weakening of the material.

3.5.2 Retained Austenite

RA is distributed throughout the material domain by means of an assigned volume fraction. The volume fraction is randomly assigned to each element, however, the process ensures that the aggregate amount of RA within the microstructure is representative of concentrations typically found in 52100 steel, approximately ten percent. Using an assigned state variable, the volume fraction at each location within the domain was implemented within the ABAQUS FE model to modify element specific material properties. For simplicity, a Voight or rule of mixtures solution [72] was applied to calculate the yield strength for each element similar to previous modeling of RA in 52100 steel [35].

$$S_y = V_f * S_{ya} + \left(1 - V_f\right) * S_{ym} \tag{3.5}$$

where V_f, S_{ya}, and S_{ym} are the volume fraction of austenite, yield strength of austenite and yield strength of the matrix, respectively. In order to compare with the experimental data presented by Voskamp [42], the yield strength and modulus of elasticity are needed for both the austenite and matrix of 52100 steel. Hatem [34] provides material properties for the austenitic phase while Shimizu [73] has conducted extensive material testing on 52100 steel. Table 2.1 contains the required material properties for this investigation.

3.5.3 Residual Stress

The fundamental concept of internal or residual stresses due to misfit strains is well understood. However, the prediction of RS within materials is a complex phenomenon to capture. The occurrence of RS can be considered as the combination of two accumulative functions and one dissipative function. Plastic yielding and phase transformations within the material will increase misfit strains while material relaxation reduces internal stresses.

Relaxation has been observed in cyclic loading conditions of materials with preexisting RS values such as cold rolled steel or shot peened materials [86,87]. Voskamp [42] also provides evidence of relaxation occurring during the RCF process by observing a decrease of the RS values measured at depths where all RA has transformed. Some phenomenological models have been proposed to predict new residual stress states in materials as function of previous stress state, applied stress, and cycle [88–90]. These models are material dependent and limited to uniaxial loading conditions. Zhuang et al. [91] proposed a physics based modeling approach, however, this approach is not applicable to an evolving residual stress state nor complex state of stress as would be present during the RCF process.

Initial simulations were used to verify the model developed by comparing experimental work performed by Voskamp to simulated results. The maximum Hertzian pressure due to the applied load was set to 3.28 GPa. According to Johnson [92], the yield condition for two contacting cylinders assuming a Von Mises criteria is given by the following equation

$$p_0 = 3.1\,k \tag{3.6}$$

where p_0 is the maximum Hertzian pressure and k is the shear yield strength of the material. This yield criterion is extended to line contact by the notion of equivalent radius. Experiments performed using a MTS torsional fatigue rig give $k \approx 1.5$ GPa for 52100 through hardened steel, Figure 3.3.

Figure 3.3: Static torsional test of through hardened 52100 steel. Yielding initiates at approximately 1500 MPa.

Therefore, given Voskamp's loading conditions, the effects of plasticity are small and will therefore be neglected when considering RS formation. Thus, RS formation becomes a function of phase transformations and material relaxation. Due to the extremely intricate nature of residual stresses arising in the material, an empirical formulation is constructed from experimental results obtained by Voskamp. The function assigns an RS value to each element within the domain based on the RA decomposition and stress history. The RS values are then implemented within ABAQUS and Matlab to modify the subsurface stress state and energy calculations, respectively.

Material degradation, retained austenite transformation, and residual stress formation are all considered to be occurring simultaneously. The modeling procedure determines damage as a function of cycles using equation (2.9). The change in damage is used in conjunction with the work performed along habit planes to determine RA decomposition and RS generation. Values of

RA and RS were calculated using an iterative process to converge at a new material state. This material state is then implemented within the ABAQUS simulation.

3.6 Results and Discussion

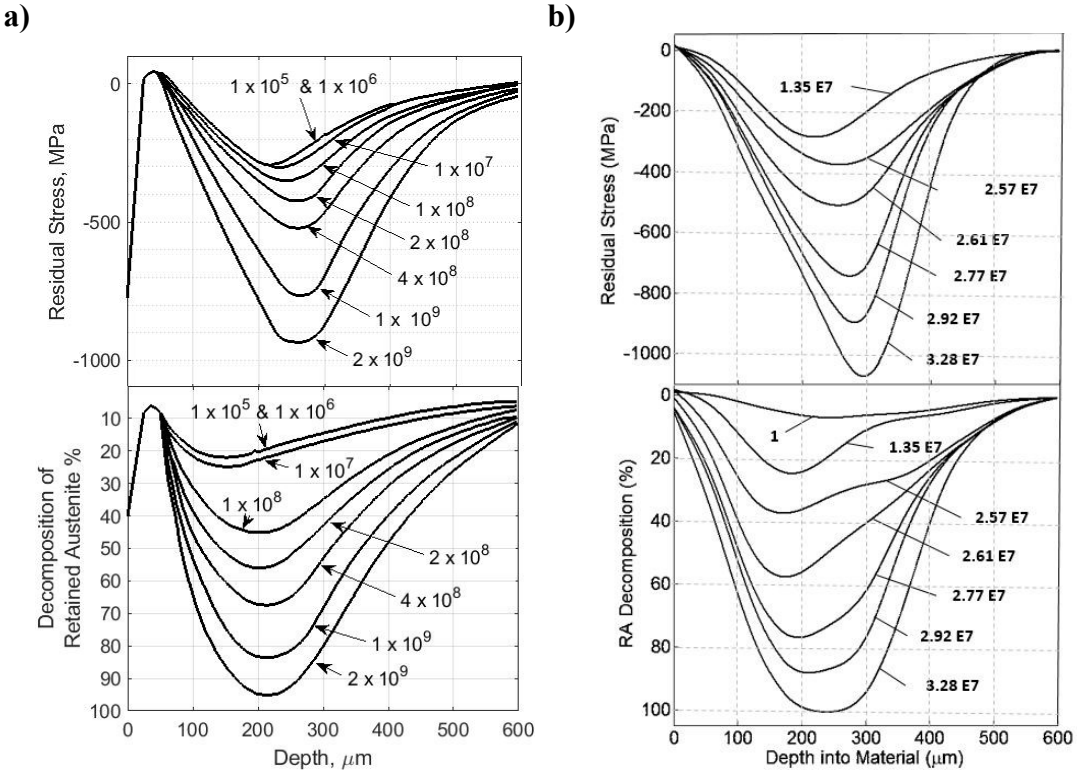

Figure 3.4: RS values and RA Decomposition as a function of depth and cycles. a) Experimental results provided by Voskamp et al [42] from 52100 steel deep-groove ball bearings. b) Simulated results.

The ABAQUS simulation combining material degradation, phase transformations and residual stress formation was first completed with loading conditions and material parameters to replicate experimental conditions as recorded by Voskamp [42]. The results for this simulation are directly compared to experimental measurements of RA decomposition and RS formation in deep groove ball bearing obtained through X-ray diffraction as depicted in Figure 3.4.

Both the RA decomposition and RS formation observed in the simulated results show good agreement with Voskamp's measurements. The simulation correctly predicts the largest RA decomposition near 0.215 mm with an asymmetric profile about the depth of highest decomposition. Additionally, the RS profile produced via the simulation closely mirrors stress

levels measured within the bearing material. The simulation predicts a marginally higher compressive stress at a slightly deeper depth within the material. Overall, the trends of RA decomposition and RS formation are remarkably similar to experimental results. It should be noted that Voskamp et al. attributes the high compressive stresses and high RA decomposition at the surface to the machining processes performed to manufacture the specimens.

The results of the initial simulation indicate the model is capable of capturing the overall pattern of microstructural evolution due to RCF. However, the model is not considered accurate at predicting microstructural evolution as a function of cycles. This is attributed to uncertainty in the material parameters chosen for the simulation as well as the underlying assumption that all material parameters will remain constant throughout the entire process. Regardless of the model's limitation in predicting material evolution as a function of cycles, the model is considered adequate for a comparative examination of initial residual stress profiles.

3.6.1 DER Formation

RA decomposition is considered to directly correlate to the formation of the DER [38]. Therefore, the results of the FEA modeling of RA decomposition were compared to experimental observations of DER formation. In order to compare the FEA results with DER formation, the volume fraction of austenite was plotted in grayscale at different steps throughout the simulation. The maximum value of 12.5% RA in this simulation is represented by white while a 0% austenite concentration is represented as dark gray. Figure 3.5 presents images of the RVE from the FEA simulation utilizing parameters to simulate loading conditions described by Voskamp.

Due to crystal orientation, RA within certain prior austenite grains is more susceptible to martensitic transformations. This is the cause of the seemingly sporadic transformations occurring at various depths. As demonstrated in Figure. 3.5, the repeated rolling contact favors transformations within the region between the maximum orthogonal shear and the maximum Von Mises stress. As RA is depleted within this region, transformations begin to occur more regularly at greater depths. The results closely represent experimentally observed patterns and behavior of DER formation. Figure 3.6 illustrates images of DER formation in deep groove ball bearings made of 52100 steel. Figures 3.6a and 3.6b correspond to a rolling contact fatigue specimens after 3.4 x 10^8 and 1 x 10^9 cycles, respectively, applying a 3.2 GPa maximum Hertzian pressure.

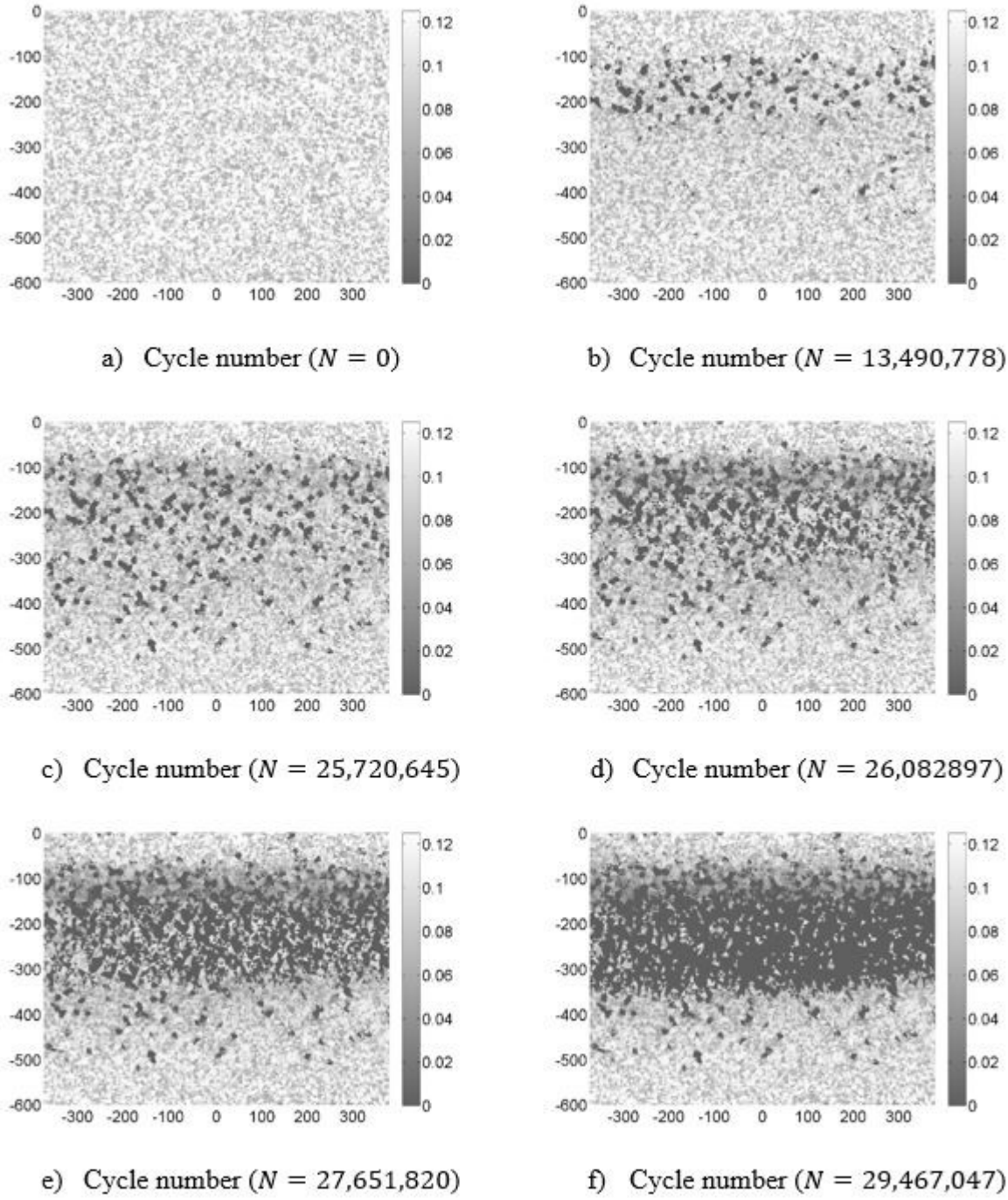

Figure 3.5: Simulated RA decomposition plotted in a relative scale where white is the maximum RA present (12.5%) and black represents zero RA. Images correspond to an increasing cycle count moving from left to right.

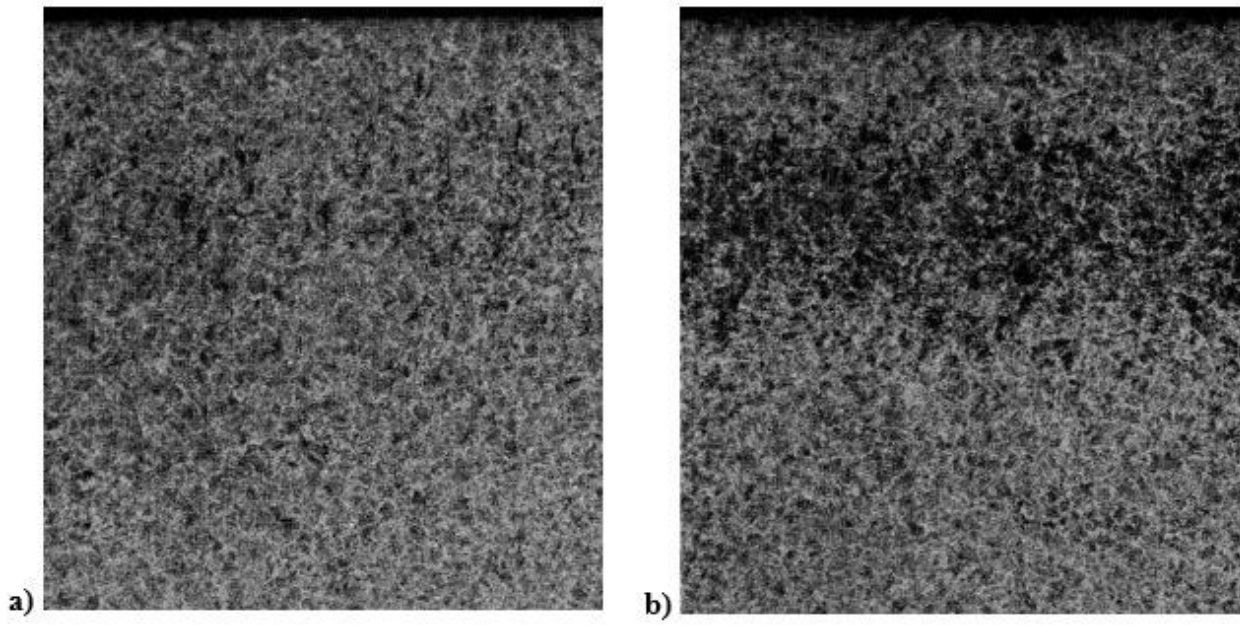

Figure 3.6: Images of DER formation in 52100 steel due to rolling contact P_max=3.2 GPa after a) 3.4 x 10^8 cycles and b) 1 x 10^9 cycles [42]

3.6.2 Effect of Initial Residual Stress State

Different manufacturing processes achieve a variety of initial residual stress conditions. Some methods such as shot peening, laser-shock peening, and cold rolling intentionally induce RS within the material. Other processes such as heat treating, case carburizing, or gas nitriding inevitably create RS fields within the material. Nikitin et al. [86] provides RS profiles for conditions of laser-shock peened and cold rolled steel. Walvekar et al. [85] discusses various RS profiles due to the carburizing process; these profiles are also applicable to nitride layers [93]. Seven distinct RS profiles are implemented within the microstructural evolution simulation to represent RS values achieved via manufacturing processes. Figures 3.7 through 3.13 illustrate differences in RA decomposition and RS formation due to various initial RS profiles. The implemented initial residual stress profiles correspond to different manufacturing processes: laser-shock peening, deep rolling and carburizing at different case depths (b, 2b, 4b, 5b, 10b).

In general, the addition of an initial residual stress state provided an increase to the total number of cycles required to cause RA transformations. Furthermore, in the cases of high initial residual stresses near the surface, laser-shot peened; deep rolled; and carburized at a case depth of

b, the high compressive stresses near the region of maximum orthogonal shear stress serve to retard phase transformations. This creates a scenario where the RA phase found deeper within the material is more likely to transform. This effect is minimal in the laser-shot peened case but apparent in the deep rolled and case depth of b material as illustrated in Figure 3.8-3.9.

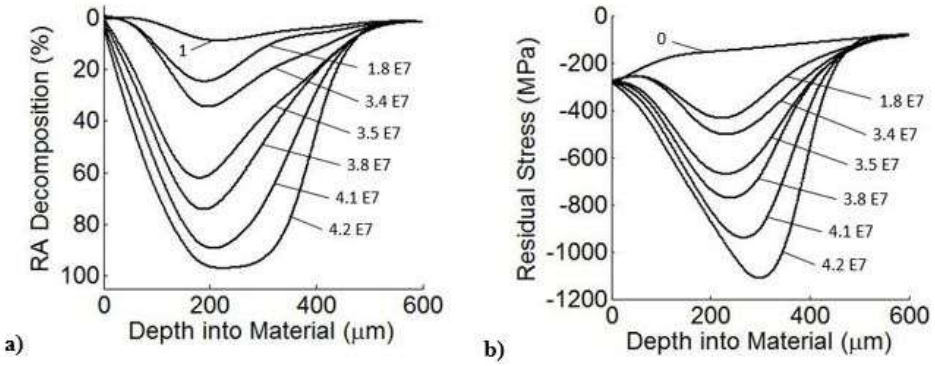

Figure 3.7: Simulation results for a) RA decomposition and b) RS formation in laser shot peened steel.

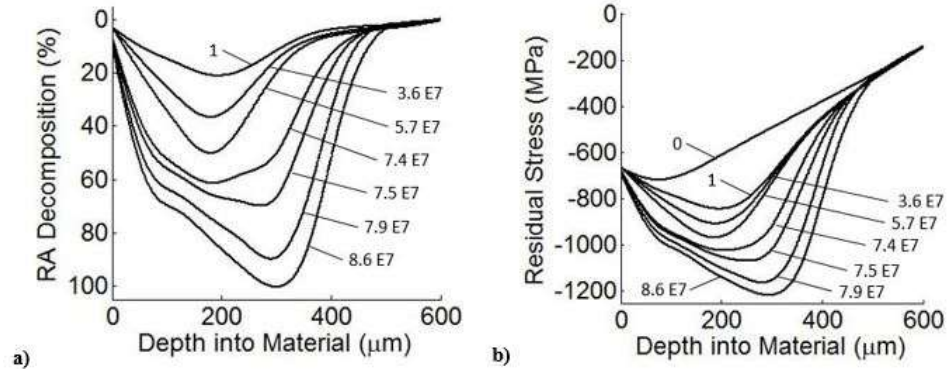

Figure 3.8: Simulation results for a) RA decomposition and b) RS formation in deep rolled steel.

In the case of large initial residual stresses deeper within the material, preliminary RA decomposition is concentrated at the location of maximum orthogonal shear stress. As this region is depleted, RA at greater depths begins to be consumed by the RCF process as shown in Figure. 3.11-3.13. Failure in the RCF process occurs when a crack propagates to the surface and material is dislodged creating a pit or spall. Therefore, in order to extend RCF life, material degradation is preferential at greater depths within the material. RS profiles that have increasing RS values at depths beneath the location of orthogonal shear stress intensify the RA decomposition within the

near surface region. Since this behavior is linked to material degradation, this may lead to crack initiation nearer the surface and therefore lower RCF lives.

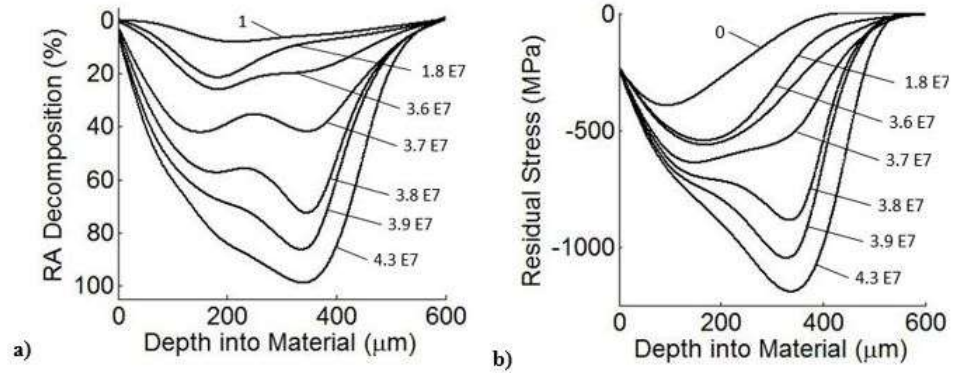

Figure 3.9: Simulation results for a) RA decomposition and b) RS formation in case carburized steel of case depth b, where b is the length of the Hertzian half-contact.

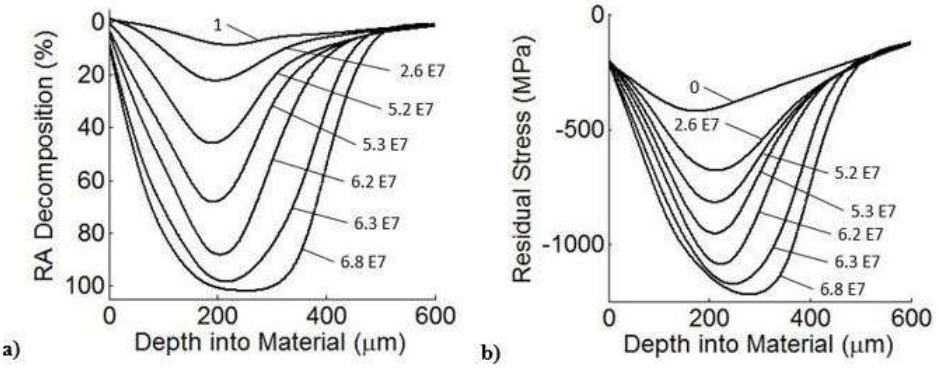

Figure 3.10: Simulation results for a) RA decomposition and b) RS formation in case carburized steel of case depth 2b.

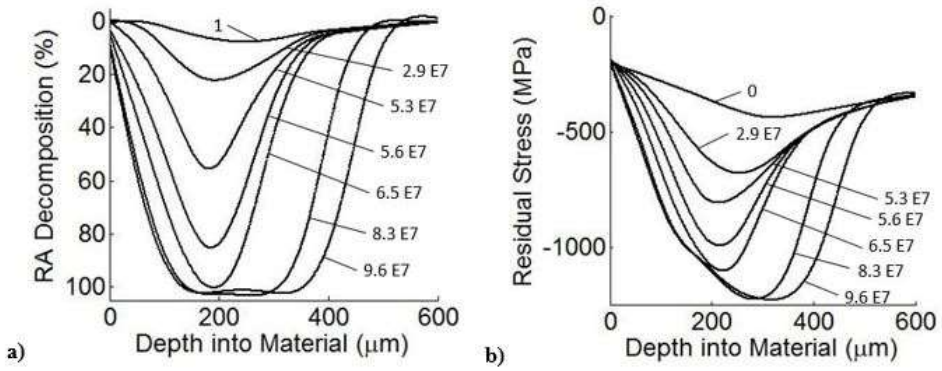

Figure 3.11: Simulated results for a) RA decomposition and b) RS formation in case carburized steel of case depth 4b.

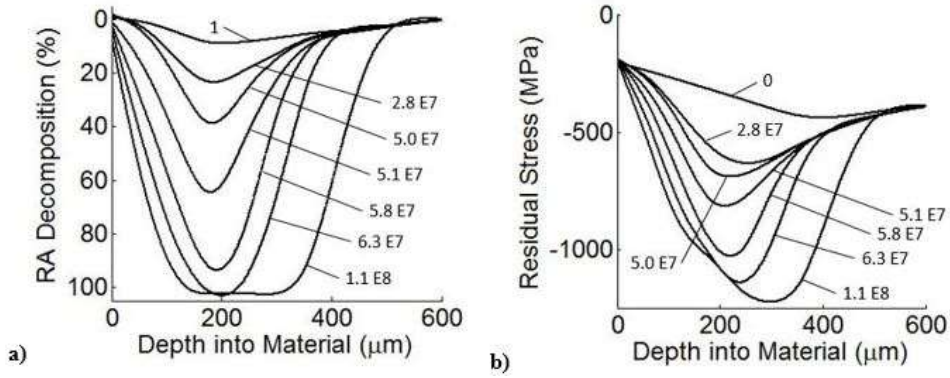

Figure 3.12: Simulated results for a) RA decomposition and b) RS formation in case carburized steel of case depth 5b.

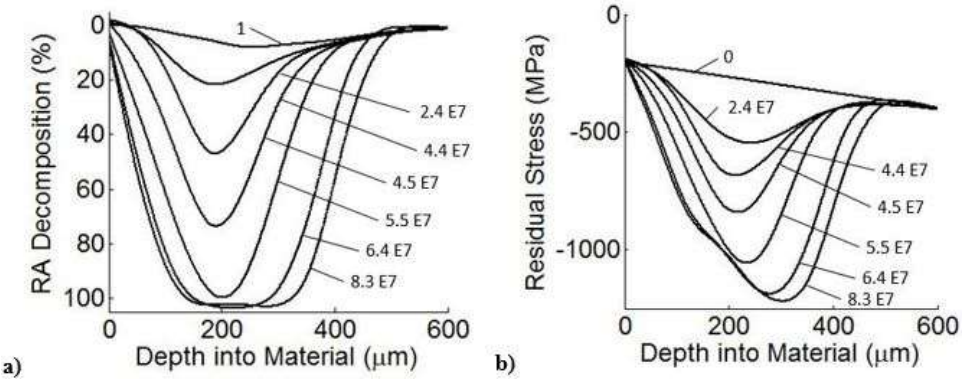

Figure 3.13: Simulated results for a) RA decomposition and b) RS formation in case carburized steel of case depth 10b.

Considering all the initial RS profiles implemented within the simulation, the deep rolled case was considered the most beneficial. The high RS values near the surface retard near surface material degradation and shifted the material deterioration to greater depths. These results concur with practices frequently performed in industrial settings. Often to increase the life of a rolling element bearing, the component will be subjected to a load much larger than anticipated operating conditions to cause plasticity and large residual stresses similar to the deep rolled RS profile.

3.7 Summary and Conclusion

The focus of this paper was to capture a more complete picture of microstructural evolution occurring during the RCF process. This was accomplished by utilizing principles of damage mechanics and energy to predict phase transformations within the material. Residual stress values were then determined from experimental data relating stress state and RA decomposition to RS present within the material. Material degradation, RA transformations and RS formation are then coupled together within an ABAQUS FE simulation to observe microstructural evolution due to RCF. The simulation provided good agreement with experimentally determined values of RA decomposition and RS formation in deep groove ball bearings.

The modeling procedure was then used to investigate various initial RS conditions within the material. Higher RS values near the surface caused microstructural alterations to occur deeper within the material. This is beneficial as cracks would need to propagate a larger distance in order to reach the contact surface.

CHAPTER 4. RESIDUAL STRESS FORMATION AND STABILITY IN BEARING STEELS DUE TO RETAINED AUSTENITE TRANSFORMATION

4.1 Introduction

Hardened steels are commonly used for critical mechanical components subjected to rolling contact fatigue (RCF). The high hardness achieved through rapid quenching and subsequent heat treatments is ideal for RCF scenarios. To improve RCF life, compressive residual stress (RS) is often introduced within the material [94–96]. Carburization, nitriding, over-rolling, hard turning and shot peening are viable processes to induce compressive RS within materials. The RS created during these processes is a consequence of either chemical, thermal, or plastically generated misfits within the material [82]. Materials that use phase transformation specifically to generate residual stresses in the material can also be created.

Typically, the austenite phase in steels is energetically unstable at low temperatures. However, because of the rapid quenching and chemical composition, austenite may exist within the steel matrix at room temperature. The entrapped or retained austenite (RA) within the steel microstructure is a metastable phase that produces improved ductility and strain hardening behavior in specimens subjected to tensile loading. Improvements in material behavior are attributed to the approximate 5%–8% volume expansion accompanying the transformation as face-centered cubic (FCC) austenite transforms to a body-centered cubic (BCC) ferrite/cementite or a body-centered tetragonal (martensite) crystal lattice.

Unlike many types of phase transformation, RA transformation is martensitic or occurs in an orderly manner without the need for diffusion. Instead of relying on diffusion, RA transformation is typically assisted or triggered by the applied stress state or overall material strain. Although tensile stresses normal to the RA habit plane facilitate decomposition [28], RA transformation can occur under purely compressive loading.

Several published studies have supported this observation. Hossain et al. [97] applied compressive stresses to high-carbon steel to examine RA transformation. The results show increasing RA transformation as compressive stresses increase. Interestingly, Hossain et al. [97] also indicates that despite 3 GPa of applied compressive stress, some amount of RA remained in the material microstructure. Similar work by Voskamp [42] observed gradual RA transformation

in bearing raceways as a function of rolling passes. An increase in compressive RS magnitude was observed to accompany RA transformation. Morris et al. [78] proposed that the process of RA decomposition in bearing steels subject to fatigue is enabled by the weakening of the surrounding steel microstructure, which allows the RA to expand. Results by Voothaluru et al. [81] of in-situ neutron diffraction on bearing steel subjected to uniaxial loading supports this idea. The results indicated that no RA transformation occurred until the material began to plastically deform, which created space for the RA to transform.

Many researchers consider RA within the microstructure to be beneficial to material fatigue resistance. Some attribute the improvement in fatigue life to the theory that RA acts to blunt crack tips propagating through the material [18]. In the case of RCF, researchers have suggested that the compressive residual stresses accompanying RA transformation improve RCF life [10–12,14,15].

However, the issue is more complex than simply the amount of RA present within the material. In order to achieve high volume fractions of RA, specific heat treatments and chemical compositions are required to stabilize the RA within the material. Further, the stability of the RA is also dependent on morphology. Park et al. [57] observed bulk or granular RA decomposing at lower macro strains compared to film RA, which is much thinner and often wedged between or around plates of martensite. Garcia-Mateo et al. [98] suggested that the stability of RA must neither be too high nor too low to capitalize on the benefits of RA within the material. For RCF, the increase in compressive RS from RA transformation is assumed to be the most significant benefit. But the development of RS in the material cannot be attributed solely to RA transformation.

As previously mentioned, many processes are available to induce RS within a material microstructure. The extremely high localized stresses caused by the RCF phenomenon induce subsurface compressive RS [77]. Once RS is present in the material, repeated loading creates a competing process known as “material relaxation” to alleviate RS [88,90]. Zhuang and Halford [91] identified the main factors affecting RS relaxation: initial magnitude, stress amplitude, and number of cycles. Lu et al. [99] notes that relaxation via macroplasticity is dominant for high stresses. Thus, the RS present within the bearing steel material is a combination of various phenomena occurring simultaneously.

The objective of this investigation is to observe RS development as a function of RA transformation in bearing steels. A material subjected to rolling contact fatigue exhibits compressive principal stresses. The differences between these principal stresses create shear

stresses within the body, including fully reversed shear stress. The RCF process can be greatly affected by a number of factors such as lubrication, contamination and material hardness. In order to remove the influence of these factors, bearing steel specimens were subjected to fully reversed shear stress via torsional fatigue. Torsional fatigue has the added benefit of applying pure shear without compressive stresses to hinder RA transformation, applying a far more uniform stress state compared to RCF, and removing the high localized stresses of rolling contact as a means of RS generation.

To examine the relationship between RA transformation and RS generation, specimens of carburized AISI 8620 steel with high RA concentrations (~35%) were subjected to various loads of torsional fatigue at prescribed cycles. The specimens were then examined using X-ray diffraction techniques to observe changes in the RA concentration and RS magnitude. The results demonstrate the interaction between RA transformation and material relaxation as it relates to RS formation in the material. Utilizing the experimental results, an analytical model was developed to predict RS formation in the AISI 8620 steel specimens.

4.2 Experimental Investigation

ISO standard 1352 torsional specimens of carburized AISI 8620 steel were machined to the specifications presented in Figure 4.1 and subjected to fully reversed shear loading. The specimens were specifically manufactured to have high amounts (approximately 35%) of RA within the microstructure. The material was measured to have an ultimate shear strength (S_{us}) of 2.17 GPa.

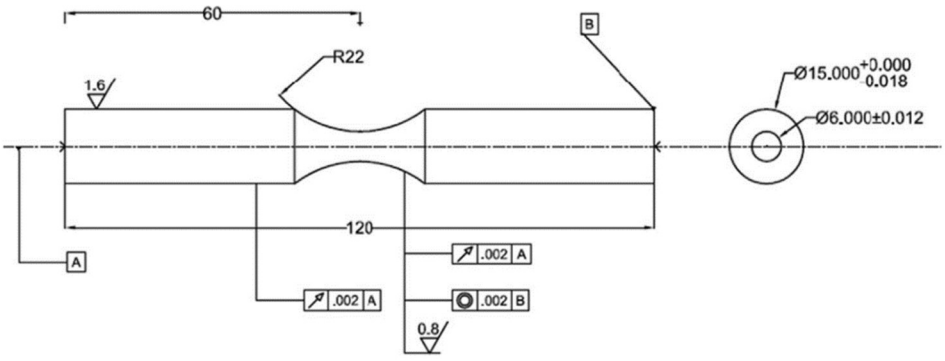

Figure 4.1: Torsional fatigue specimen. Surface is ground and polished along axial direction.

The testing was performed at three stress levels in an attempt to isolate the different phenomena occurring during the fatigue process. At low stresses, relaxation is generally minimal, and slow and progressive RA transformation is expected. At high stresses, RA is quickly consumed during the fatigue process, and relaxation becomes the dominant RS behavior. Therefore, $0.4S_{us}$, $0.6S_{us}$, and $0.8S_{us}$ were chosen as the stress levels. Stress level $0.6S_{us}$ acts as an intermediary between the two extremes. Multiple tests were performed at each stress level for the various prescribed cycles. Table 4.1 presents the stress level and prescribed cycles for each torsional fatigue specimen.

In order verify that RS was not being generated by the fatigue process alone, certain specimens were subjected to a unique stress history. The specimens were first subjected to one fatigue cycle at $0.8S_{us}$, after which additional fatigue testing was performed at $0.4S_{us}$ or $0.6S_{us}$. The first cycle served to consume the majority of the RA in the system, thereby enabling the observation of RS formation in the material in the absence of RA. This group was designated as the R group (see Table 4.1).

Table 4.1: List of various stress levels and prescribed cycles for the carburized AISI 8620 specimens. Cells with numbers represent standard testing; an ® represents R group results. Cells with both indications had two specimens performed under the two different conditions.

		Cycles								
Shear Stress Amplitude (S_{us})		1	5	10	50	100	1,000	10,000	100,000	
	0.4	4-1		4-2 ®			4-3 ®	4-4	4-5	Group 1
	0.6	6-1	6-2	6-3 ®		6-4	6-5 ®			Group 2
	0.8	8-1		8-4	8-5					Group 3

Upon test completion, x-ray diffraction (XRD) was used to measure the RA volume fraction, circumferential RS, and distortional RS in the material. The measurements were taken at 0, 10, 40, and 80 μm below the surface. The average measurement error of the circumferential stress was $\pm$4.34 MPa, with the highest recorded error being $\pm$6.95 MPa.

4.3 Results and Discussion

The primary focus of this work was to investigate the evolution of the RS in carburized AISI 8620 steel. Phase transformation and material relaxation are considered to be the primary drivers of RS formation. Specimens were divided into four groups. Groups 1, 2, and 3 correlate to the applied shear stress amplitude (τ_a) at the values of $0.4S_{us}$, $0.6S_{us}$, and $0.8S_{us}$, respectively. The final group is the R group, as previously mentioned. Each group will be discussed individually, although certain overarching patterns were observed in all data sets.

Similar to bearing steels subjected to RCF, the torsional specimen exhibited a "shakedown period." The shakedown period is characterized by higher strains that lead to material hardening. After initial deformation, the material response stabilized and constant strains were observed until final failure was approached. Consequently, the first fatigue cycle, regardless of τ_a, consumed the most RA compared to any subsequent fatigue cycle. Additionally, the initial fatigue step caused a reduction in the surface RS magnitude.

After initial loading, RA decomposition and RS generation stabilized. RA decomposition occurred at near equal rates throughout the material depth measured. As the amount of RA present in the material decreased, inducing additional phase transformation in the remaining RA became increasingly difficult. Indicative of uniform volume expansion, RA transformation did not lead to an increase in distortional or shear RS under any loading condition. An increase in compressive circumferential RS due to RA transformation was observed in all cases.

4.3.1 Group 1 ($\tau_a = 0.4S_{us}$)

For the majority of specimens in group 1, the change in RS magnitude from depths of 0 to 10 μm below the surface was approximately 200 MPa, as shown in Figure 4.2. This matches well with the pristine or un-run specimen measurement, and is indicative of two important phenomena. First, the RS increase caused by RA transformation was evenly distributed throughout the material. Second, material relaxation was small, if not negligible, for the $0.4S_{us}$ case. Given that relaxation is a function of the current RS in the material, the fact that the much higher RS value at the surface was not reduced to more closely match the RS value at 10 μm suggests that material relaxation was not occurring.

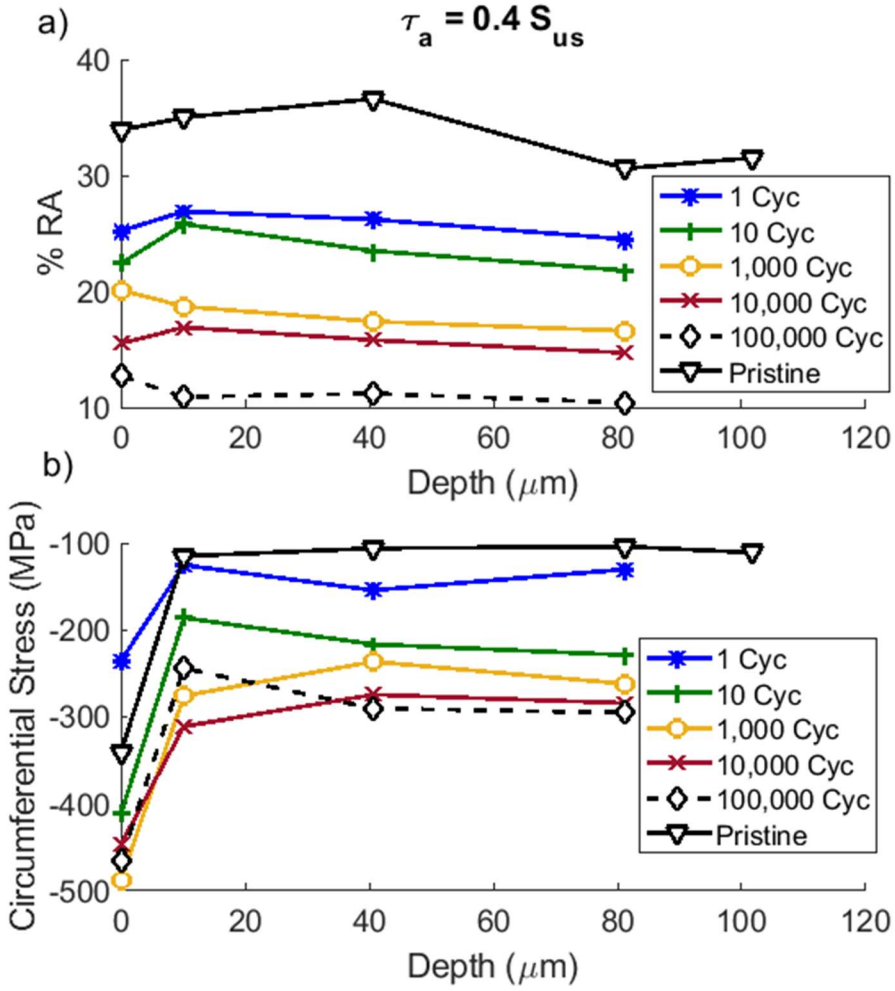

Figure 4.2: X-ray diffraction measurements for torsional fatigue specimens subjected to a shear stress amplitude of 0.4 S_us after various prescribed fatigue cycles. a) RA percentage as a function of depth. b) Circumferential residual stresses as a function of depth.

Despite being the lowest loading condition, the RA volume fraction was reduced to approximately 25% within the first cycle. The RA morphology is most likely the cause for the large drop in RA. As Parks et al. [57] demonstrated, the larger bulk RA transforms more readily at low strains. More importantly, the large amount of RA decomposition did not lead to a significant increase in the overall RS value. This leads to the conclusion that not all RA present within the material is equally advantageous in generating compressive RS.

The authors observed that the RA decomposition due to the low τ_a value was slow and progressive. This enables a gradual increase in compressive RS over a long period of time. As less RA is transformed with each cycle, the RS growth levels off (stabilizes) and is incapable of

attaining a higher RS magnitude. This is particularly interesting, since stagnation occurs while the volume fraction of available RA in the material is greater than 10%. It follows that the applied stress does not provide sufficient energy to drive the transformation forward.

4.3.2 Group 2 ($\tau_a = 0.6S_{us}$)

Due to the increase in τ_a, the rate of RA decomposition for group 2 increased, as expected. The first fatigue cycle was able to trigger phase transformation and reduce RA concentration by approximately 18%, as shown in Figure 4.3. Contrary to group 1, the majority of the compressive RS was produced during the first load cycle. Although it is unclear why RS was generated on the first cycle, unlike the previous group, possible explanations are presented here.

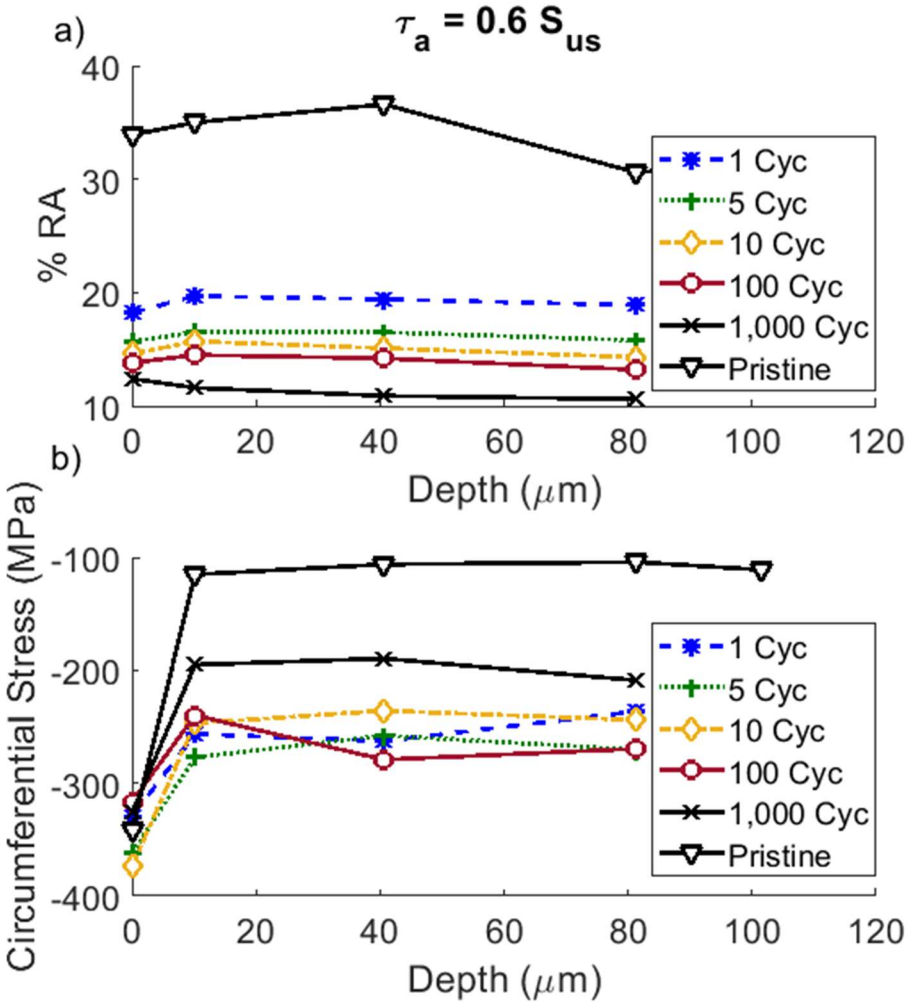

Figure 4.3: X-ray diffraction measurements for torsional fatigue specimens subjected to a shear stress amplitude of 0.6 S_us after various prescribed fatigue cycles. a) RA percentage as a function of depth. b) Circumferential residual stresses as a function of depth.

First, the increase in RS could be a combination of the phase transformation and plastic deformation occurring in the material. The higher shear stress may cause localized yielding to generate misfits in the material. This seems unlikely, since the applied stress is reasonable and uniform throughout the depth.

The second possibility is based on the results from Hossain et al. [97]. During compressive testing, two different martensitic structures were formed. The initial RA decomposition resulted in hexagonal close-packed (HCP) martensite, while the later RA transformation resulted in BCC/BCT martensite. The difference in lattice structure generally results in very different compressive stresses. Therefore, the large amount of RA decomposition observed during the first

cycle may have depleted all the HCP martensite and initiated the BCC/BCT stage. This idea is supported by RS measurements from group 1 where significant RS generation occurred only after one-third of the RA volume fraction had transformed. RA morphology may also be an important consideration. Bulk RA transforms more readily, but it may not generate the desired compressive stresses.

In contrast to group 1, the increased shear stress in group 2 enabled material relaxation to occur from the offset of testing, as evidenced by the reduction in the difference of the RS between the surface and 10 μm below. This is best demonstrated in Figure 4.3 by the change of slope at the surface between the pristine specimen and all other specimens in group 2. It is interesting to note that after the initial loading, the slopes did not appear affected by additional cycles.

After the initial fatigue cycle, ensuing cycles resulted in further RA decomposition, but no significant increase in the compressive RS state (as shown in Figure 4.3). This is indicative of a balance between material relaxation and RS generation as a result of RA transformation. As less RA transforms, the RS generation is no longer able to counteract the material relaxation, and the RS magnitude begins to decline.

4.3.3 Group 3 ($\tau_a = 0.8S_{us}$)

At $\tau_a = 0.8S_{us}$, macro plastic deformation is expected. Figure 4.4 illustrates the high rate of RA decomposition and material relaxation caused by high stress and material yield. Within one fatigue cycle, the RA volume fraction in group 3 was reduced to 8% and surface RS was reduced by approximately 200 MPa. Two measurements were taken for specimens subjected to one cycle at $\tau_a = 0.8S_{us}$. The results show very different material responses. For one measurement, the residual RA was extremely low (~8%) and only a small increase in RS magnitude accompanied the large amount of RA decomposition. For the other measurement, more RA remained in the material (~11%) and a significant increase in compressive RS was observed. With additional cycling, the RA concentration was further reduced — but the fatigue process was unable to completely deplete RA from the material, as was observed in the previous groups. Despite applying multiple loadings above the material yield strength, some of the RA remained untransformed.

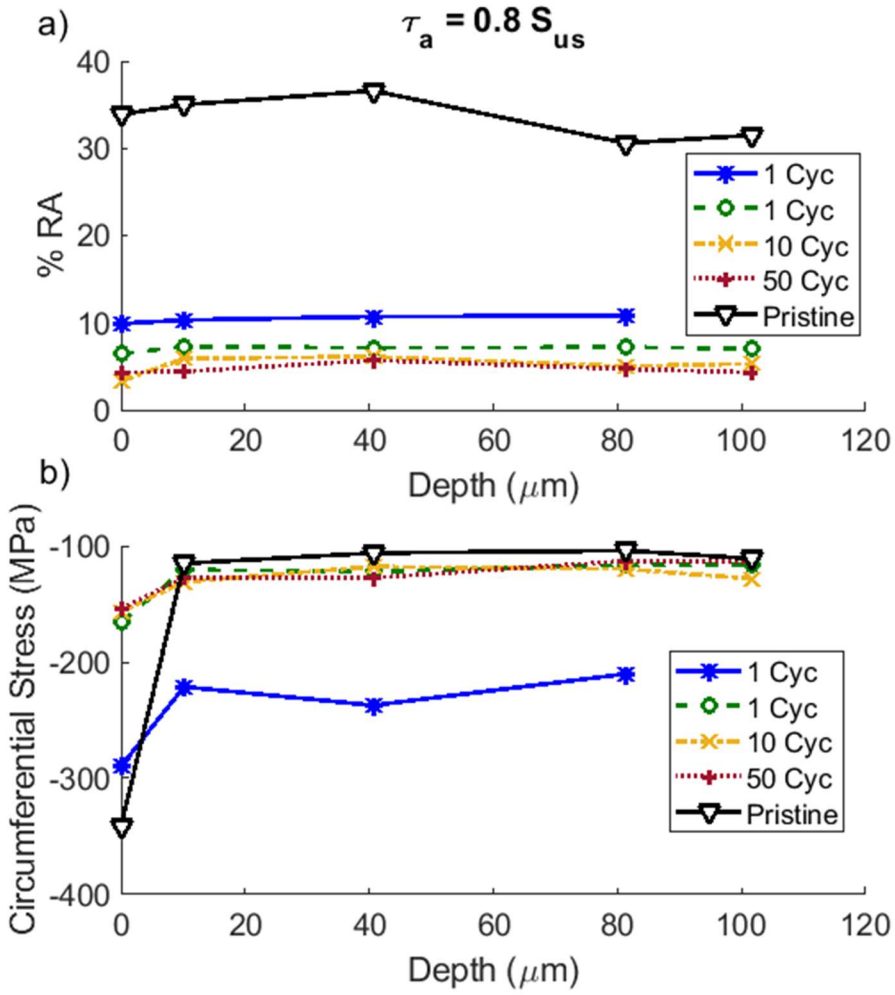

Figure 4.4: X-ray diffraction measurements for torsional fatigue specimens subjected to a shear stress amplitude of 0.8 S_us after various prescribed fatigue cycles. a) RA percentage as a function of depth. b) Circumferential residual stresses as a function of depth.

4.3.4 Group 3 (R Group)

As previously mentioned, the R group consists of specimens that had a single $0.8S_{us}$ fatigue load applied prior to being subjected to additional cycles at lower τ_a values (see Table 4.1 for exact specifications). The focus of the R group was to observe the RS behavior after the majority of the RA had already transformed. Figures 4.5 and 4.6 depict the R group specimens subjected to 10 and 1,000 cycles, respectively, with their non-R group counterparts.

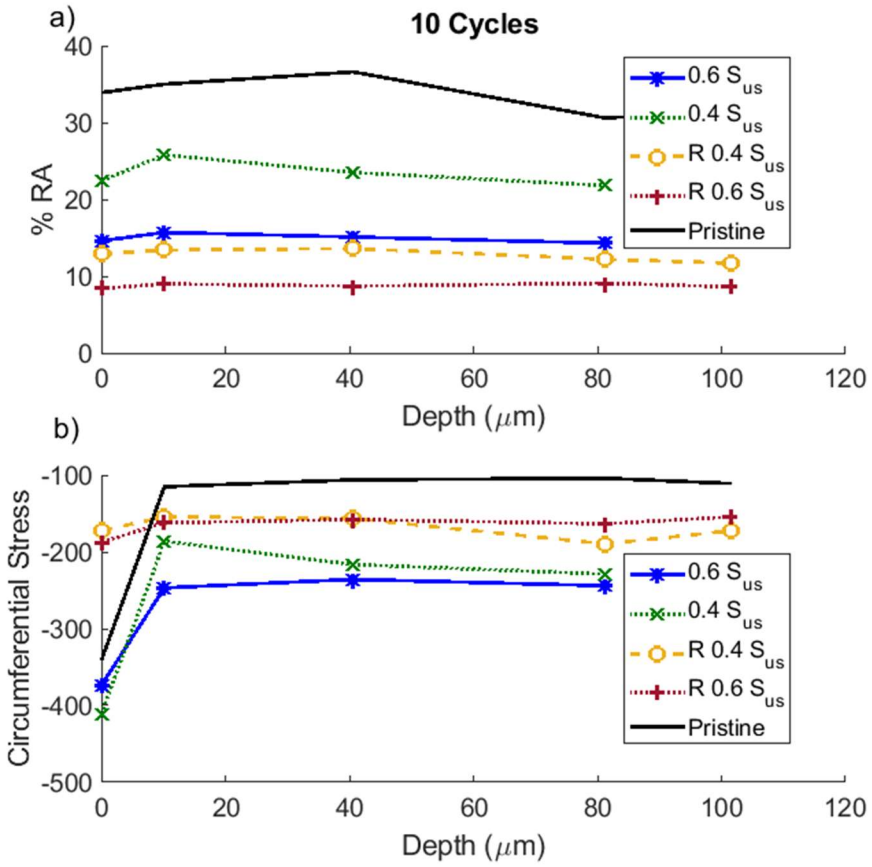

Figure 4.5: X-ray diffraction measurements for torsional fatigue specimens subjected to 10 fatigue cycles at various shear stress amplitudes. a) RA percentage as a function of depth. b) Circumferential residual stresses as a function of depth.

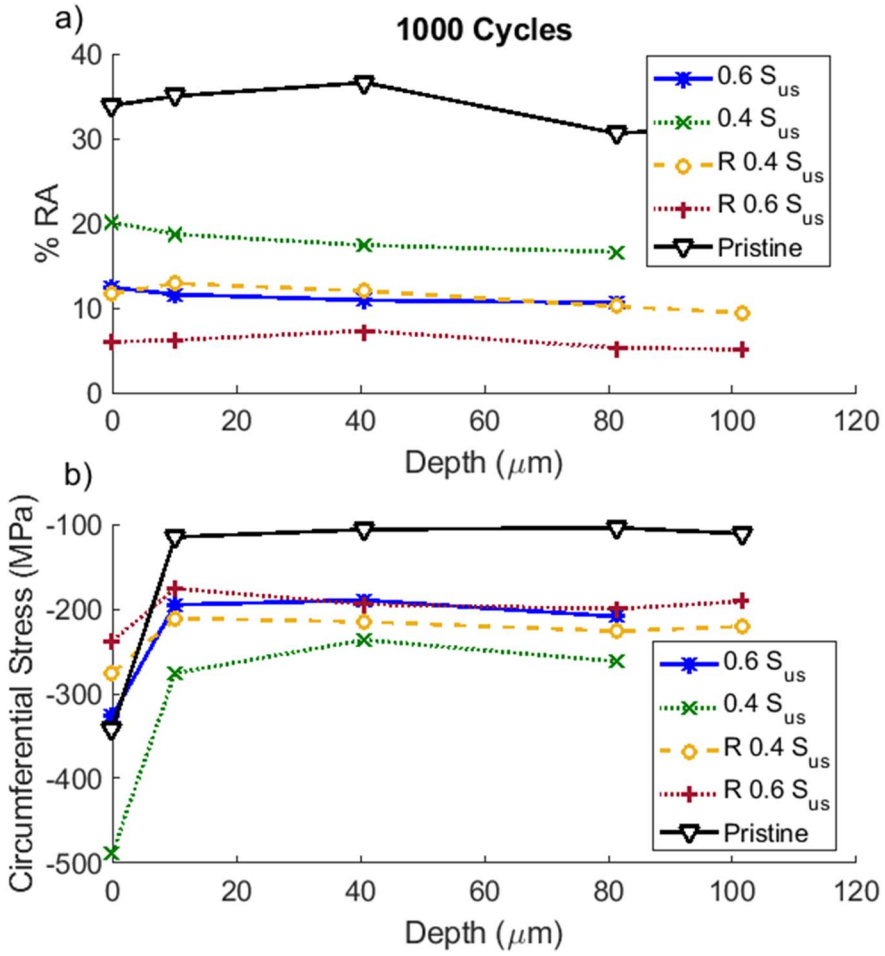

Figure 4.6: X-ray diffraction measurements for torsional fatigue specimens subjected to 1,000 fatigue cycles at various shear stress amplitudes. a) RA percentage as a function of depth. b) Circumferential residual stresses as a function of depth.

The first high stress load was assumed to put the material into a condition similar to the specimens from group 3 that were subjected to one cycle. For R group specimens with higher RA measurements (>10%), the first high stress cycle was assumed to modify the RS state to a condition similar to the RS measurements observed for the group 3 specimens with a higher remaining RA concentration. The continued fatigue process at lower stress then caused further alterations to the RA and RS present.

The initial high stress cycle consumed the majority of the RA, leaving the more stable RA within the material. As cycling continued at lower stresses, the RS magnitude stagnated because the applied stress was an insufficient driving force to induce transformation in the remaining RA.

High stresses at the beginning of the fatigue process, whether intentional or accidental, had an adverse effect on the development of compressive RS, as observed in Figures 4.5 and 4.6.

4.4 Analytical Model

The next objective was to develop an empirical model based on the experimental results incorporating the effects of RA transformation and material relaxation. The following equation is proposed to describe the change in RS per cycle:

$$\sigma_{RS}^{*} = \sigma_{RS} + F_1(\Delta\gamma) + F_2(\tau_a, \sigma_{RS}) \quad (4.1)$$

where σ_{RS}^{*} is the new RS magnitude, σ_{RS} is the RS magnitude at the current cycle, and functions $F1$ and F_2 represent the change in RS due to phase transformation and material relaxation, respectively.

As material undergoes case carburization, the amount of carbon diffused into the material varies as a function of distance from the surface. This is one cause of the high RS at the surface and may also explain behavioral differences between RS formation at the surface versus inside the material. Since data was not taken to measure variations in carbon as a function of depth, the model is limited and does not consider the effect of carbon concentration when predicting RS formation.

4.4.1 Effect of Phase Transformation

The F_1 function describes the observed change in RS magnitude due to the volume expansion caused by the RA transformation. F_1 is considered a function of the decomposition of RA per cycle ($\Delta\gamma$). Excluding the RA transformation caused by the initial fatigue step, RA decay due to subsequent cyclic loading is characterized well by a power law relationship:

$$\gamma = C_1 * N^{b_1} + C_2 \quad (4.2)$$

where C_1, C_2, and b_1 are fitting constants, γ is the RA volume fraction, and N is the number of fatigue cycles. These parameters vary among the groups and are presented in Table 4.2. This relationship was used to obtain $\Delta\gamma$.

Table 4.2: Constants necessary for power law relationship of RA as a function of fatigue cycles.

Shear Stress Amplitude (S_{us})	C_1	C_2	b_1
0.4	-.09337	.3482	.07973
0.6	.2909	-.1061	-.03976
0.8	.04184	.04529	-.8495

The relationship between RS increase and $\Delta\gamma$ is best observed in group 1, where the rate of material deformation and relaxation was lowest. The change in RS is captured well by:

$$F_1 = A_1 * \Delta\gamma \tag{4.3}$$

where A_1 is a fitting parameter. As the amount of RA that transforms per cycle decreases, the RS growth levels off and allows for material relaxation to occur.

4.4.2 Effect of Relaxation

The relaxation function F_2 is based on work by Zhuang et al. [91] and is dependent on τ_a and the current RS magnitude in the material (σ_{RS}). With increasing τ_a and σ_{RS}, the rate of relaxation increases, but the relaxation is a much stronger function of τ_a. For example, at $\tau_a = 0.4\, S_{us}$ the relaxation is nearly negligible at even the highest RS level, while at $\tau_a = 0.8\, S_{us}$ relaxation becomes the most dominant of the three functions.

The relaxation function is described as follows:

$$F_2 = A_2 * \left(\frac{\sigma_{RS}}{S_y}\right)^{f_1} * \left(\frac{\tau_a}{S_y}\right)^{f_2} \tag{4.4}$$

where $A_2, f_1,$ and f_2 are fitting parameters and S_y is the material yield strength in shear (~1500 MPa). Equation (4.4) fulfills the intuitive boundary condition that material relaxation goes to zero as the RS value approaches zero. Further, the form allows for τ_a to have a greater effect on material relaxation than the RS value. For the specific case of the carburized AISI 8620 steel, the RS measurements show a minimum compressive RS limit at 100 MPa. This is attributed to the carburization process, which allows carbon to diffuse into the material and occupy interstitial sites. Equation (4.4) is thus modified by adding an addition term to represent the RS value created by carburization:

$$F_2 = A_2 * \left(\frac{\sigma_{RS}+B_1}{S_y}\right)^{f_1} * \left(\frac{\tau_a}{S_y}\right)^{f_2} \tag{4.5}$$

B_1 acts as the reference of material relaxation. For materials without RS values created by carburizing or nitriding practices, $B_1 = 0$.

4.5 Predictive Model Comparison

The RS values at the specimen surface did not exhibit RS formation behavior similar to that of the interior points within the material. This is thought to be caused by the carburization process. Regardless, the modeling procedure was more focused on matching behavior at subsurface locations, since crack initiation in RCF is commonly a subsurface phenomenon. Using an optimization scheme, all necessary constants were calculated based on experimental data and are reported in Table 4.3. After calibrating the functions, the model was run and compared to the experimental results. Figures 4.7–4.10 illustrate the results of the predictive model compared to the corresponding experimental results. The modeling results represent the RS alterations well.

Table 4.3: Constants for RS functions.

A_1	1297.86
A_2	119.07
f_1	2
f_2	15.15

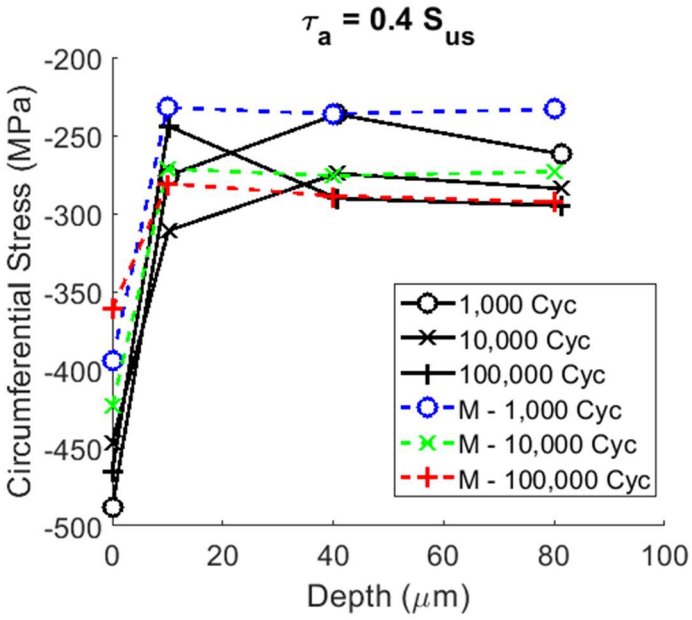

Figure 4.7: Predictive RS model results at $\tau_a = 0.4\ S_{us}$ plotted against experimental results under equivalent conditions. M is used to identify results obtained through the predictive model.

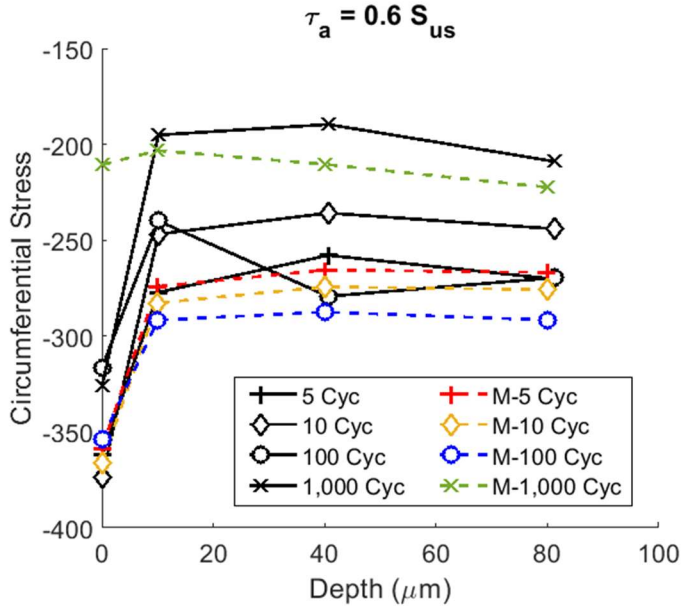

Figure 4.8: Predictive RS model results at $\tau_a = 0.6\ S_{us}$ plotted against experimental results under equivalent conditions. M is used to identify results obtained through the predictive model.

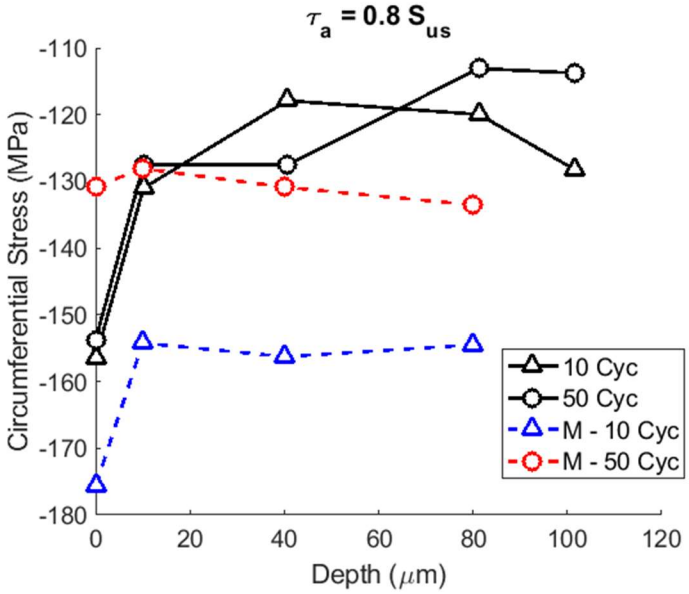

Figure 4.9: Predictive RS model results at $\tau_a = 0.8\, S_{us}$ plotted against experimental results under equivalent conditions. M is used to identify results obtained through the predictive model.

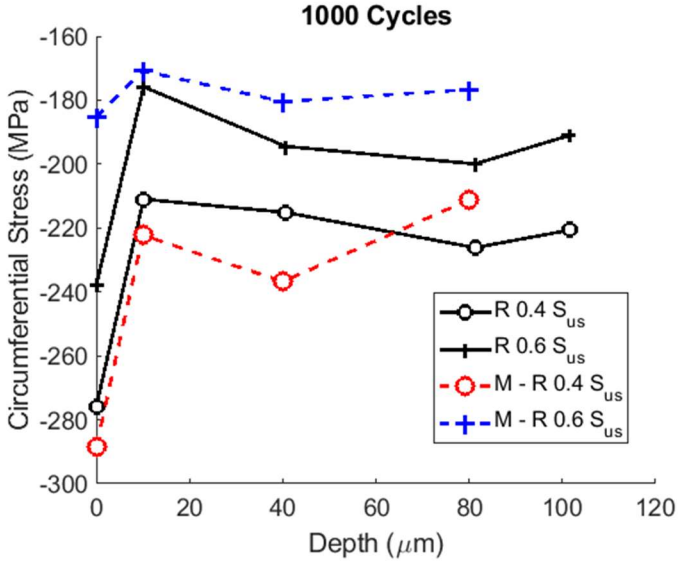

Figure 4.10: Predictive RS model results for R group specimens plotted against experimental results under equivalent conditions. M is used to identify results obtained through the predictive model.

As previously mentioned, an initial high stress load can greatly disrupt RA decomposition and, consequently, RS generation in the material. Using the torsional fatigue life (N_f) for carburized AISI 8620 steel presented in Figure 4.11(a), the model was exercised to examine the effect of a high stress cycle later in the fatigue process. Figure 4.11(b) demonstrates how RA transformation stalls and the amount of RA in the material stabilizes with increasing fatigue cycles. The RA remaining in the system is thus unusable because the applied loading is unable to trigger transformation. By applying a higher stress, the unusable RA becomes active, resulting in a sudden increase in RS magnitude (as seen in Figures 4.12 and 4.13). Restoring the original loading results in a higher rate of relaxation than previously experienced because RA is further depleted and cannot act as an obstacle to material relaxation. Therefore, the inactive RA in the system can act as a buffer from unexpected high loads, but the benefit is limited.

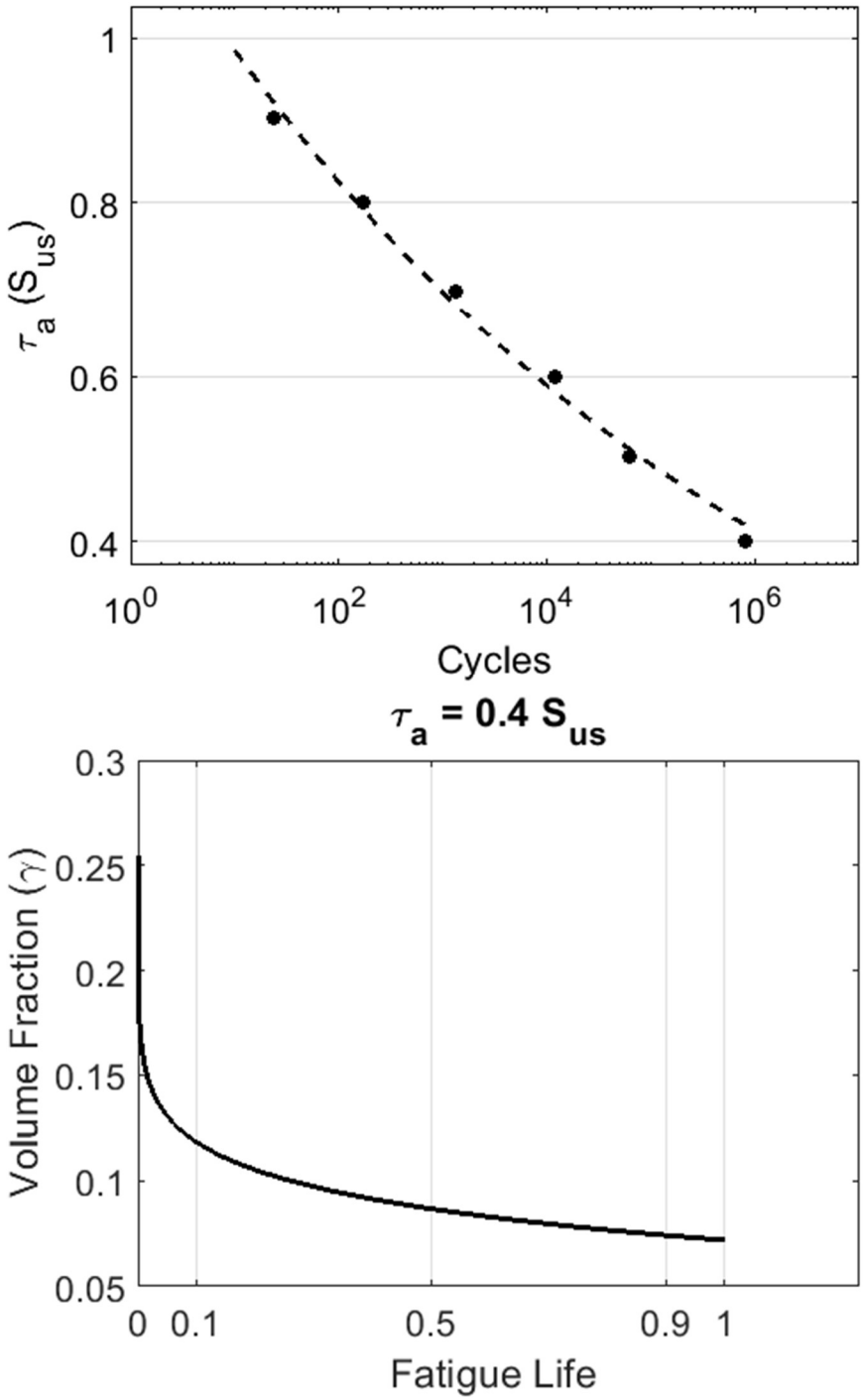

Figure 4.11: (a) Torsional fatigue results for carburized AISI 8620 steel. (b) Model prediction of volume fraction of RA present within the material subjected to $\tau_a = 0.4\ S_{us}$

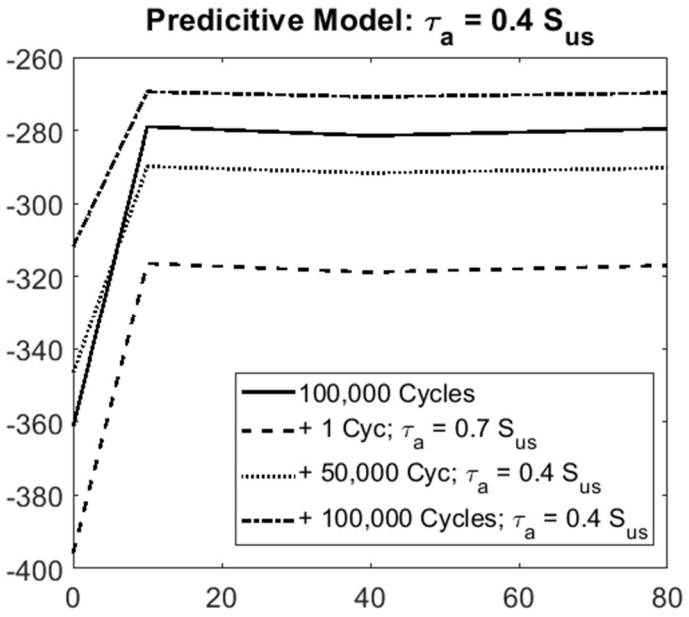

Figure 4.12: Predictive RS model used to evaluate the effects of high stress applied during the high cycle fatigue process for $\tau_a = 0.4\, S_{us}$. The different lines represent the evolution of the RS in the material when subjected to additional cycles.

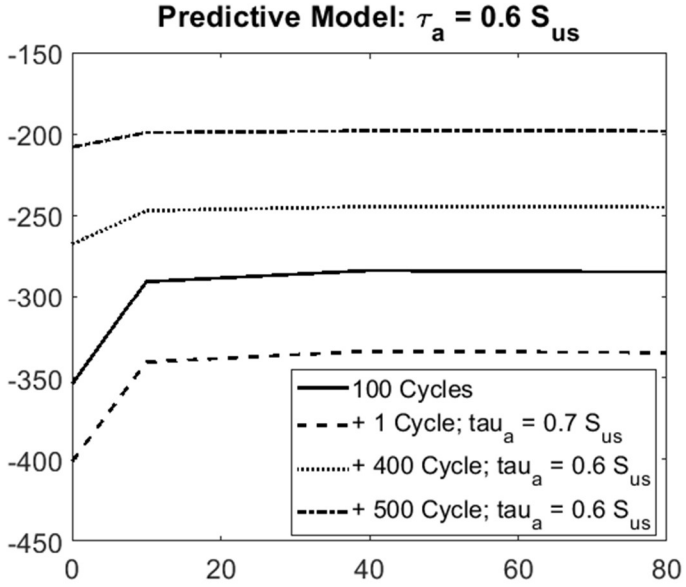

Figure 4.13: Predictive RS model used to evaluate the effects of high stress applied during the high cycle fatigue process for $\tau_a = 0.6\, S_{us}$. The different lines represent the evolution of the RS in the material when subjected to additional cycles.

Figures 4.14, 4.15, and 4.16 depict the RA volume fraction and RS magnitude as a function of load and cycles. The figures illustrate the importance of controlling the applied load. At $\tau_a = 0.4S_{us}$, phase transformation is triggered and the corresponding RS generated is maintained in the material throughout the fatigue process. In contrast, when $\tau_a = 0.6S_{us}$, the material is initially able to generate a large amount of RS by quickly consuming a large amount of RA. However, the higher stress results in a higher rate of relaxation. Since no RA is available to obstruct relaxation, the high RS value is quickly reduced during the fatigue process.

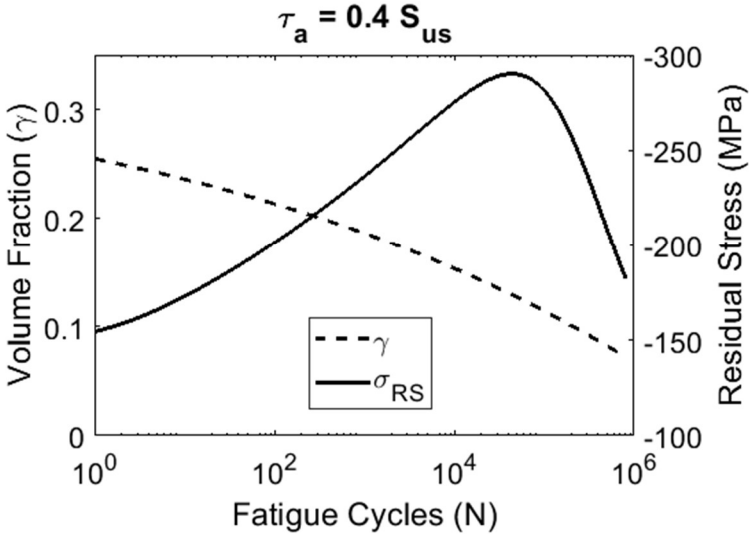

Figure 4.14: Model prediction of RA and internal compressive stresses present within the material at $\tau_a = 0.4\, S_{us}$.

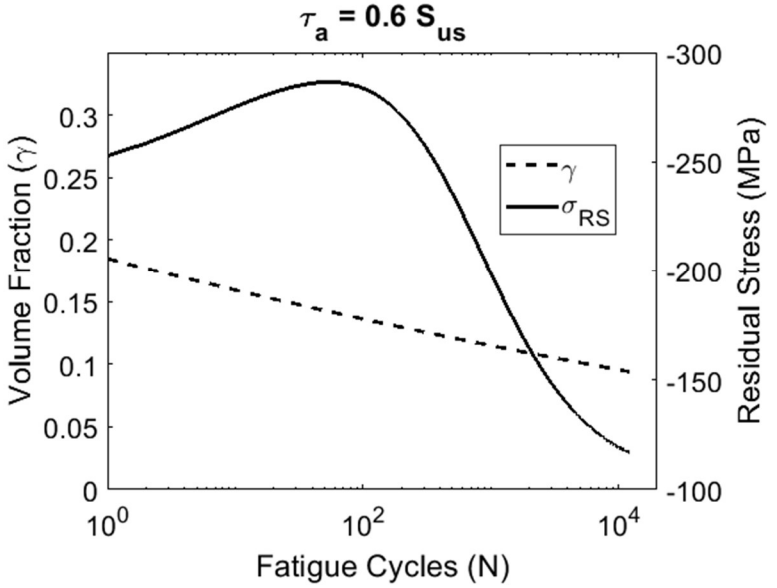

Figure 4.15: Model prediction of RA and internal compressive stresses present within the material at $\tau_a = 0.6\, S_{us}$.

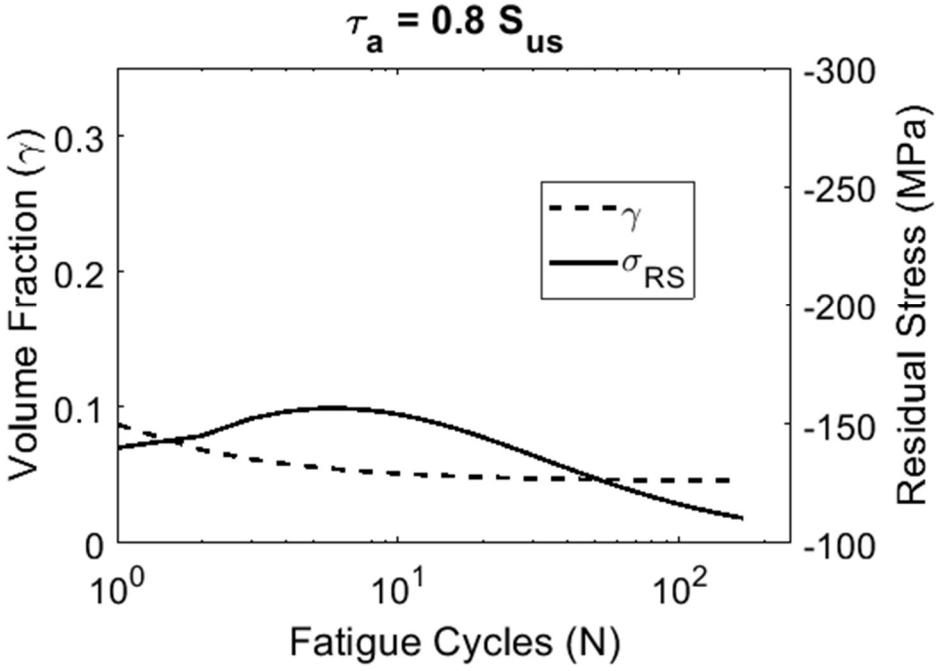

Figure 4.16: Model prediction of RA and internal compressive stresses present within the material at $\tau_a = 0.8\, S_{us}$.

Table 4.4: XRD measurements of high RA 52100 through-hardened steel subject to τ_a=0.25 S_us=530 MPa. RS values from predictive model are in parentheses.

Cycles	**$\Delta\gamma$**	**Residual Stress (MPa)**	
100	.025	-36 μm	(32.45)
$1 * 10^5$	0.09	-147 μm	(-116.8)
$1 * 10^6$	0.04	-85 μm	(-51.9)
$3 * 10^5$	0.11	-116.5 μm	(-142.8)

Both 8620 and 52100 steel are commonly used in bearings and exhibit similar hardness and yield strength. To further validate the predictive model, XRD measurements of through-hardened 52100 steel subject to torsional fatigue were compared to model results. The 52100 material was subjected to torsional fatigue at 530 MPa or $\tau_a = 0.25\ S_{us}$. RA volume fraction and circumferential RS measurements were taken at 10 µm and 100 µm below the surface, as seen in Figures 4.17 and 4.18. The 52100 steel data is limited, so all parameter values calculated from the AISI 8620 steel were used to predict RS generation in the 52100 steel. The XRD measurements and modeling results are summarized in Table 4.4. The modeling results match well, considering all parameters were calibrated using the XRD data for AISI 8620 material.

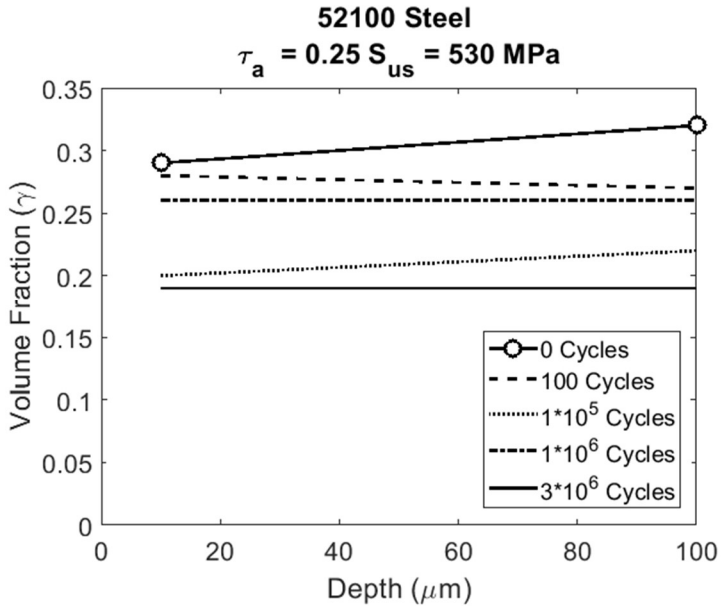

Figure 4.17: Volume fraction of retained austenite in 52100 through-hardened steel subjected to torsional fatigue at $\tau_a = 0.25\, S_{us} = 530$ MPa.

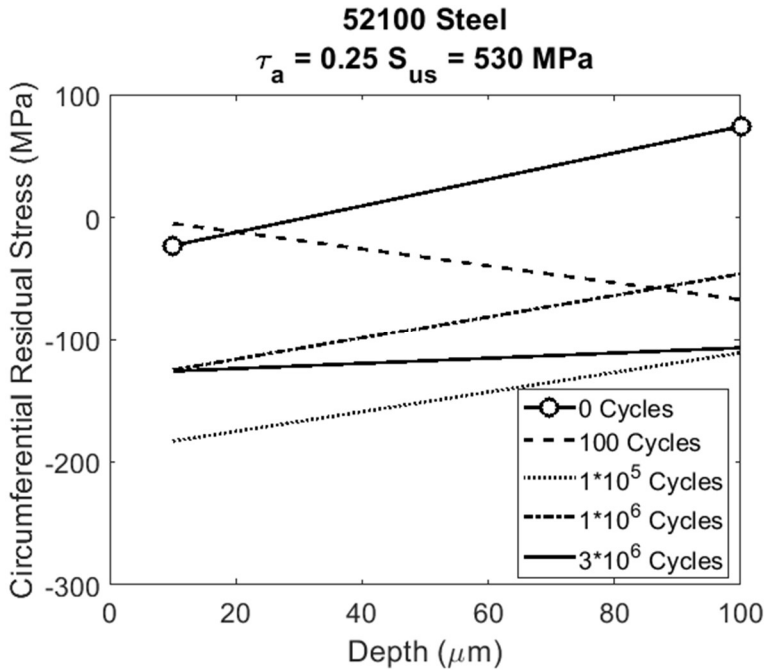

Figure 4.18: Residual stress in 52100 through-hardened steel subjected to torsional fatigue at $\tau_a = 0.25\, S_{us} = 530\ MPa$.

4.6 Rolling Contact Considerations

The objective of this study was to examine RS formation in bearing steel as a function of RA transformation. A torsional fatigue procedure was chosen instead of an RCF process because it eliminated many factors that could generate RS. However, bearing steels are intended for rolling contact scenarios. Therefore, the results were considered next with respect to RCF. This was accomplished by recognizing that the RCF of a given maximum Hertzian pressure (P_{max}) produces fully reversed shear stress in the body at a depth of $z = 0.5b$, where b is the half-width of the Hertzian contact. This allows for a comparison between the applied shear in torsion and shear due to RCF. According to Johnson [92], the amplitude of shear reversal between two contacting elastic bodies in rolling contact is:

$$\tau_a = 0.25 P_{max} \tag{4.6}$$

Converting the three values of τ_a from torsional fatigue results produces three RCF cases: $P_{max} = 3.5\ \text{GPa}, 5.23\ \text{GPa}, \text{and } 7\ \text{GPa}$. In this manner, the torsional fatigue results can be used to estimate RA decomposition and accompanying RS evolution in RCF of equivalent alternating shear. Based on experimental results, Hertzian contacts at approximately 5 GPa or greater rapidly deplete RA volume fraction, and compressive RS due to RA transformation is limited.
This is not to say that no compressive RS is expected in a material subject to a 5 GPa Hertzian pressure profile — rather that the RS generation directly caused by RA transformation is limited in such a scenario.

At $P_{max} = 3.5$ GPa, the RA decomposition is expected to be a more controlled and beneficial process. Contacts at or below this pressure should generate compressive RS in the material that can be maintained throughout the entire fatigue life.

Also of interest is to consider at what point the RA is no longer triggered for RA transformation. Referring again to the measurements of high-RA through-hardened 52100 bearing steel depicted in Figures 4.17 and 4.18, initial cycling does not cause a shakedown or sudden drop in RA volume fraction. RA is stable within the material, particularly for the specimen subject to 1 million fatigue cycles. The small amount of RA that did transform resulted in a mild increase in compressive RS, but the applied stresses were insufficient to trigger the majority of the RA in the

material. Applied torsion of $\tau_a = 530$ MPa corresponds to a Hertzian contact of $P_{max} = 2.1$ GPa. This indicates that in order to maximize the benefits of compressive stresses associated with RA transformation, materials should be subject to RCF within the range of $P_{max} = 2.1 - 3.5$.

This comparison is limited as it does not account for plasticity occurring in the bodies or the hindering effect of compressive normal stresses on RA transformation. The comparison should therefore be considered a conservative prediction of RA transformation during RCF.

4.7 Summary and Conclusions

The role of retained austenite (RA) in developing and maintaining compressive residual stresses (RS) in bearing materials was examined. To evaluate RS alterations due to RA transformation, specimens of carburized AISI 8620 steel were subjected to torsional fatigue. Cyclic torsional loading was performed for a prescribed number of cycles at specific stress levels. After fatigue testing, the specimens were examined using x-ray diffraction techniques to observe RS values and RA concentration. The results identified RA transformation and material relaxation as two competing phenomena in the material. An empirical model incorporating phase transformation and material relaxation was then developed to predict RS formation. The results obtained from the model corroborate with the experimental measurements.

The experimental results indicated that only a small portion of the total RA was useful in generating compressive RS. To clarify this outcome further, modeling results were compared with known specimen fatigue lives to consider RA and RS evolution throughout the expected fatigue life. It was found that by controlling applied loading, compressive RS can be generated and maintained throughout fatigue life.

These findings were then translated into RCF scenarios to identify the loading conditions that maximize the benefits associated with RA transformation. The experimental and modeling results highlight the utility of RA transformation in increasing compressive stresses within the material, but emphasize the importance of controlling applied load in order to maintain beneficial levels of RS.

CHAPTER 5. RETAINED AUSTENITE STABILITY ON ROLLING CONTACT FATIGUE PERFORMANCE OF 8620 CASE-CARBURIZED STEEL

5.1 Introduction

To achieve high hardness and strength, bearing steels are subjected to rapid quenching in order to generate a martensitic microstructure. As a consequence of the rapid quenching process, various concentrations of retained austenite (RA) may be present within the steel microstructure. The amount of RA in a steel microstructure is a function of steel processing and chemical composition.

Generally, RA volume fraction is limited in most applications due to the dimensional instability associated with the volume expansion as RA undergoes a martensitic transformation [22,23,25,26]. The effect of RA on RCF performance has been investigated a few times [10,11,13,14,100–103], despite concerns with dimensional stability. The focus of previous research has been to examine the effects of RA quantity on various failure mechanisms caused by RCF; surface initiated cracking, subsurface initiated cracks, and micropitting. The research concludes that higher quantities of RA in the system are beneficial to RCF performance. However, to achieve variation in the RA volume fraction, researchers may alter quench severity, tempering time and duration, or carburization temperature and atmospheric carbon concentration. These variations in material processing produce variations in microstructure beyond simply the amount of RA present in the material. This leads to uncertainty on whether the change in RA volume fraction or the change in the overall microstructure is responsible for variation in RCF performance [14]. Further, limited work has been performed to examine the effects of RA stability on RCF performance. The stability of RA is defined by the driving force or energy requirement to induce the martensitic transformation. A higher stability RA requires a larger driving force to initiate the phase transformation. Thus, RA stability is affected by a number of factors.

Chemical composition affects both the amount and the stability of the RA in the material. Alloying elements such as nickel are known austenite stabilizers which enable austenite to be produced at room temperature [104]. High concentrations of carbon dissolved in the austenite also act to stabilize the austenitic phase. It is by this principle that high strength alloy steels commonly

known as TRIP steels are able to maintain a desirable amount of metastable austenite in the steel microstructure [105].

Size and shape or morphology of the RA within the microstructure are other important qualitative considerations of the austenitic phase. Xiong et al. [106] used X-ray diffraction (XRD) and transmission electron microscopy (TEM) to observe greater resistance to the martensitic transformation in small film-like RA compared to large bulk RA despite higher concentrations of carbon in the bulk RA. Parks et al. [57] performed electron backscatter diffraction (EBSD) of TRIP steel undergoing elongation and confirmed these findings. The energy requirements to drive the martensitic transformation of the RA will directly affect material properties and performance [107].

In this investigation we have experimentally examined the effects of RA on RCF performance of AISI 8620 case carburized steel. RCF testing was conducted on a 3 ball on rod test apparatus. RA quantity and residual stress (RS) magnitude was measured via XRD. EBSD was used to characterize the RA in the system. Based on the experimental results, the role of RA stability on RCF performance was investigated. The effect of RA stability was examined using a continuum damage mechanics finite element model developed for RCF simulations. The model incorporates an energy criteria to predict RA transformations due to the RCF process. The model was utilized in a parametric study to compare RCF performance as a function of the applied Hertzian pressure, RA volume fraction, and energy requirements to induce RA transformations. The results of the study indicate that RCF performance is a strong function of RA stability.

5.2 Experimental Investigation

The chemical composition of all 8620 steel specimens prior to carburization is provided in Table 5.1. All 8620 specimens were carburized for 8 hours at 940 C in a 0.90 – 1.05% carbon atmosphere and directly quenched in 49 C oil. This resulted in a case depth of 1.5 mm and a post-carburization carbon content of 0.7 – 0.8% for all specimens. The specimens were then divided into three groups to vary RA volume fraction. The variation in RA concentration was achieved through varying the amount of undercooling applied to each group of specimens prior to tempering. This allowed for consistent chemical composition between all specimens from all groups while also varying the amount of RA in the system. Table 5.2 contains the undercooling and tempering processes.

Table 5.1: Chemical Composition of of 8620 Specimens (wt%)

C	0.17 – 0.23 *0.7 – 0.8
Mn	0.35 – 0.75
Ni	0.35 – 0.65
Cr	0.15 – 0.65
Mo	0.15 – 0.25
Si	0.15 – 0.25
S	0.015 – 0.025
Cu	> 0.35
P	> 0.025
*After Carburization: 58-62 HRC at surface with case depth of 1.5 mm.	

Table 5.2: Undercooling and Tempering Process for RA groups

RA Groups	Processing Procedure
~30-35% RA (High)	No freeze Temper at 149 C for 2 hours
~15-20% RA (Mid)	-45 C freeze for 2 hours Temper at 149 C for 2 hours
~10% RA (Low)	-84 C freeze for 2 hours warm to room temperature -84 C freeze for 2 hours Temper at 149 C for 2 hours

5.2.1 XRD Measurements of RA/RS as a function of depth

RA content in the different groups was quantified and characterized using XRD and EBSD techniques. One specimen from each heat treatment group was used to examine the microstructure prior to RCF testing. To obtain RA and RS measurements as a function of depth, measurements were performed by an A2LA accredited laboratory to ISO 17025. Material was removed by electro-polishing in accordance with SAE HS784. XRD measurements were performed in

accordance with ASTM E2860 and ASTM E975 for RS and RA measurements, respectively. Figure 5.1 presents XRD data for RA volume fraction as a function of depth in the Low, Mid, and High RA groups. A large reduction in RA was observed between the High and Mid groups while the difference between the Low and Mid groups was much smaller. Despite the severe undercooling imposed upon the Low RA group, a significant amount of RA was retained in the steel.

It is well known that compressive residual stresses have a significant effect on RCF performance, therefore, XRD was also implemented to compare the residual stress state between the three groups. Figure 5.2a depicts XRD measurements to quantify RS as a function of depth in three different groups of 8620 steel specimens prior to RCF testing. The stress state is similar between the three groups with the exception of a large difference in the surface RS measurement between the High RA group and the remaining two. To verify whether this difference in compressive stresses at the surface was consistent, the surface RS was measured for three additional specimens from each of the three groups. Figure 5.2b presents the results which indicate no apparent trend in the surface RS value between the three groups.

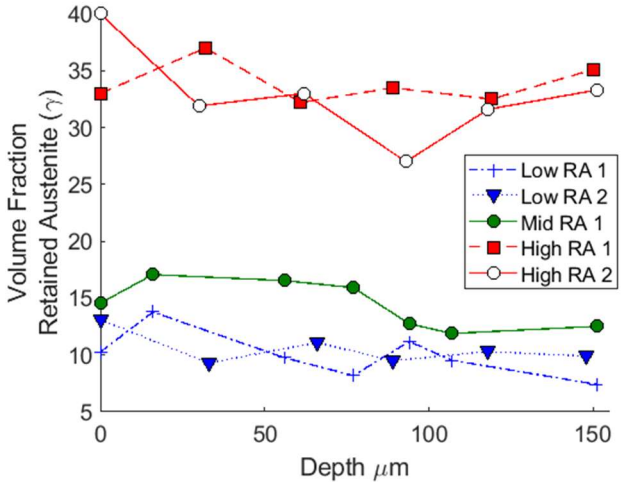

Figure 5.1: XRD measurements to quantify RA volume fraction as a function of depth in the three different undercooling groups of 8620 steel specimens prior to RCF testing.

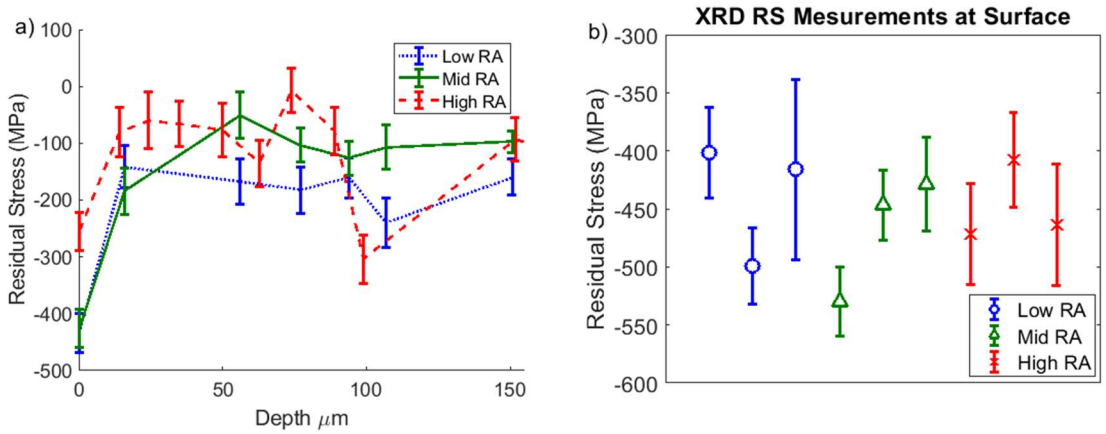

Figure 5.2: a) XRD measurements of residual stresses on experimental specimens prior to RCF testing. b) Measurements at the contact surface. Three different specimens were measured from each group.

5.2.2 EBSD and Optical Examination of Microstructure

Rolling contact fatigue is a localized phenomenon inducing high stresses near the contacting surfaces which quickly dissipate in the material as a function of distance from the contact. Using Hertzian theory for two elastic bodies in contact, the maximum orthogonal shear, maximum von Mises stress, and maximum resolved shear occur at $0.5b$, $0.7b$, and $0.78b$ below the surface, respectively, where b is the calculated half-contact width. In our experimental investigation $b = 153\ \mu m$. Therefore, the critical material which will define RCF performance is from $0 - 200\ \mu m$ below the contacting surface. Therefore, EBSD techniques was used to determine the material state near the surface.

The rod specimen was sectioned normal to the axial direction and set in a cold mount epoxy. Specimens were then mechanically polished up to a 1µm diamond abrasive with final polishing on a VibroMet using 0.05 μm colloidal silica. Since ferrous alloys are prone to oxidization, specimens were re-polished by hand using 0.05 μm colloidal silica prior to loading into the SEM. The accelerating voltage and step size for the EBSD measurements were 20 keV and 2 μm, respectively. EBSD was performed approximately up to 50 μm below the contacting surface to avoid edge charging caused by the cold mount material.

One specimen from each group was selected and up to 4 EBSD scans were performed per specimen. Table 5.3 presents the results of the EBSD investigation. The total fraction corresponds

to the amount of austenite divided by the total scan area while partition fraction is the amount of austenite divided by the area of positively identified crystal structure. For all three RA levels, the majority of the scan was considered null space where no phase description had a confidence index greater than 0.1. The null space occurs at locations of multiple grain boundaries and areas of highly distorted crystal structure. The EBSD measurements confirm variation in the RA concentration in agreement with the labels. As expected, the EBSD predicts lower RA in the system compared to the XRD measurements.

Table 5.3: EBSD results on specimens from the low, mid, and high RA groups. Values are the averages of up to 4 scans per group

	Low RA	Mid RA	High RA
Total Fraction (%) FCC Austenite	1.7	3.85	9.55
Partition Fraction (%) FCC Austenite	6.73	8.33	19.9
Total Fraction (%) BCC ferrite	23.63	42.13	38.55
Total Null Space (%)	74.67	54.03	51.9

As described earlier, EBSD was used to observe qualitative aspects of the RA: size and morphology. Figure 5.3 depicts EBSD scans from each of the three groups. Figure 5.4 shows optical white light images of the three materials after polishing to a mirror finish with 5 μm diamond paste and etching in 2% Nital for 5-7 seconds. The microstructure for all three groups consists of lathe and plate martensite as observed in the optical images. Bright areas in optical imaging represent retained austenite in the microstructure. The High RA group presented in Figure. 5.3a, has large clusters of bulk like RA approximately 5 μm across. Fine, submicron, RA pockets can also be observed throughout the high RA material microstructure. The microstructure of the intermediate or Mid RA group appears similar to the High RA group but all large RA has been removed from the system by undercooling. However, the finer RA can be seen persisting in the Mid RA group microstructure. The Low RA group has a small amount of RA in the system which is very finely dispersed in the microstructure. Please note, the amount of null space reported for the Low RA group is significantly higher than the other two groups. This is attributed to an increase in material distortion as more of the RA had undergone the martensitic transformation due to the more severe undercooling condition.

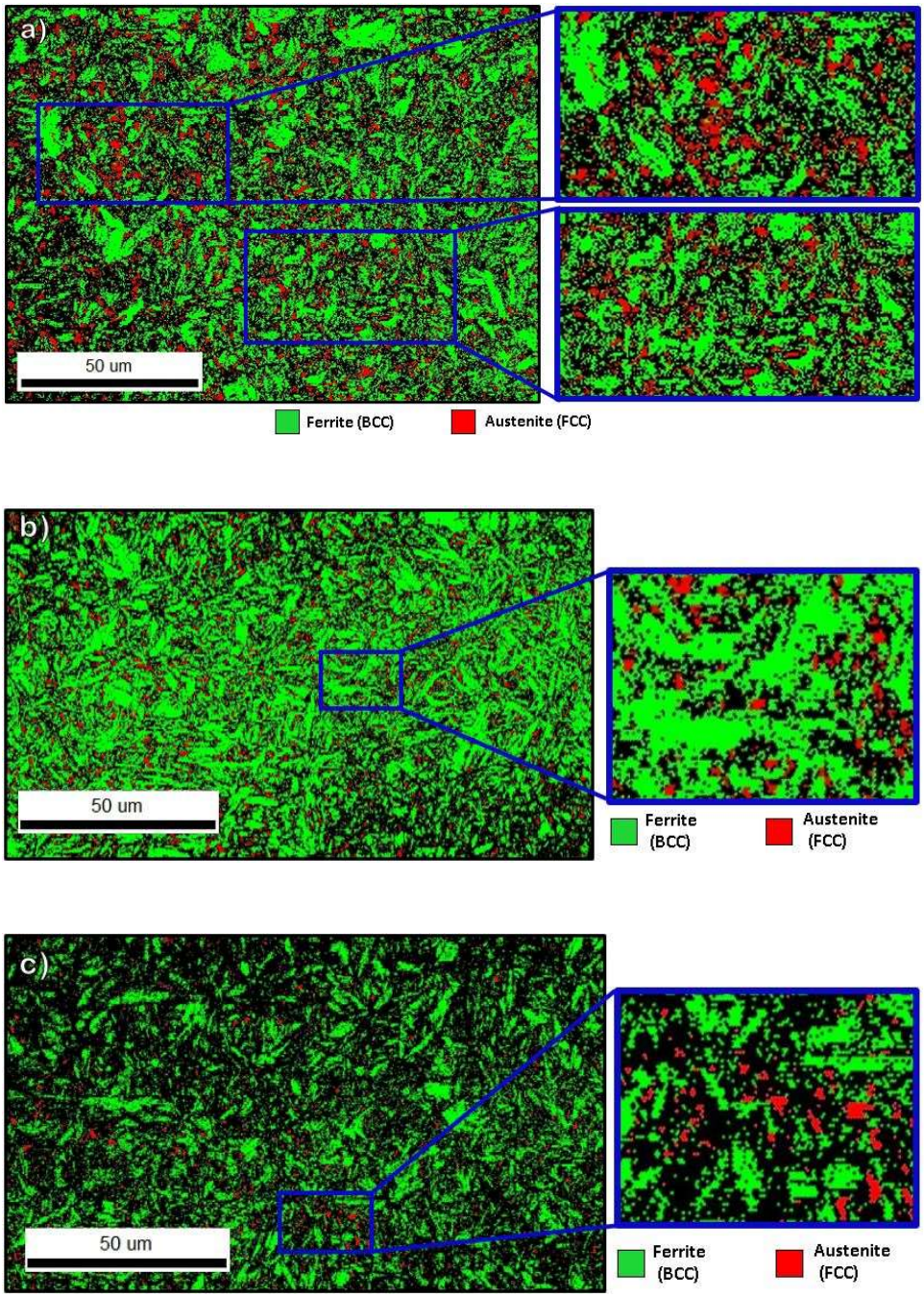

Figure 5.3: a) EBSD phase map of specimen from high RA specimen. b) EBSD phase map of specimen from intermediate or mid RA group. c) EBSD phase map of specimen from low RA group

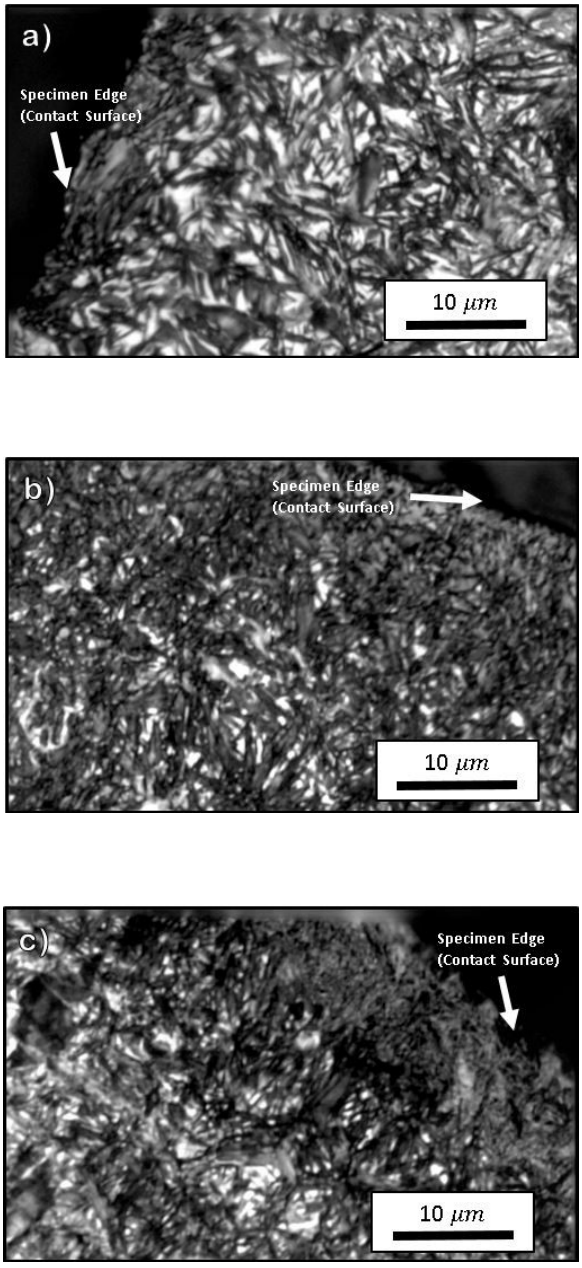

Figure 5.4: White light optical image of material surface after 2% Nital etch for a) High RA, b) Mid RA, c) Low RA.

5.2.3 RCF Experiments

RCF testing was performed using a 3 ball on rod apparatus. In this apparatus, a rod specimen is driven by an electric motor while 3 hardened steel balls are radially loaded against the rod surface using a self-aligning spring mechanism. Spring loads are calibrated using a dead weight load to achieve the desired contact pressure. An oil drip feed provides lubrication for the contact. RCF tests are run until failure. This type of testing results in a subsurface initiated failure which is detected by a rapid increase in measured vibration. Specimens are then removed and inspected to verify that a spall is present within the contact track. The experimental rig is thoroughly described by Glover [108] with similar testing performed by Liston [109]. Table 5.4 provides all relevant parameters for the RCF testing. In this investigation, tests re suspended after ~725 hours of operation if no failure occurred. 33 tests were completed for each RA group.

Table 5.4: Experimental Conditions for 3 Ball on Rod Experiment

Rod Diameter	$^3/_8$" (9.525 mm)
Rod Surface Speed	$1.8\frac{m}{s}$
Rod Surface Roughness (Sq)	0.382 μm
Ball Material	52100 through hardened steel
Ball Surface Roughness (Sq)	0.248 μm
Ball Diameter	0.5" (12.7 mm)
Applied Dead Weight	215 N
Maximum Pressure P_{max}	3.6 GPa
Hertzian Half-Contact (b)	153 μm
Lubricant	MIL-PRF-23699F
Operating Temperature ($C°$)	$\sim 45 - 50\ C°$
Lambda Ratio	0.3

5.2.4 Results and Discussion

Figure 5.5 depicts the 2 parameter Weibull distributions fitted to the experimental results obtained from the 3 ball and rod RCF machine with the accompanying Weibull parameter values. The Weibull slope or β parameter quantifies the amount of scatter in the data with lower values indicating a larger scatter. All three groups have similar Weibull slopes which fall within the range of expected values for bearing steel subjected to RCF. The Weibull shape or strength represented by the η parameter provides the number of cycles at which approximately 63% of specimens are expected to fail. The Weibull strength facilitates the comparison between the three experimental groups as the Low RA group is approximately two times that of the High and Mid groups. The results shown in Figure 5.5 demonstrate that the Low RA group outperforms the Mid and High RA group. This is contrary to the general notation that RA improves RCF performance.

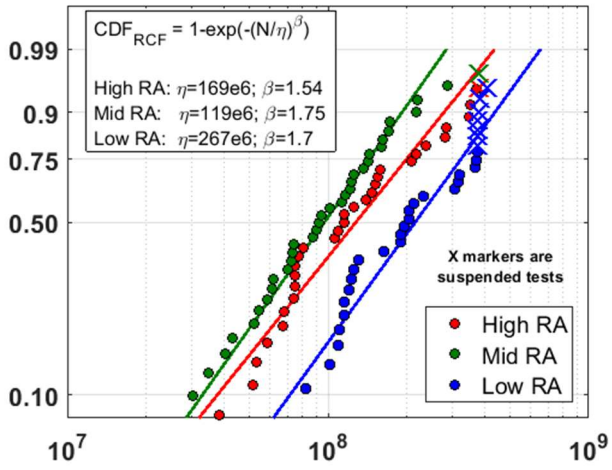

Figure 5.5: 2 parameter Weibull distributions fitted to experimental RCF results of 8620 specimens.

After completing testing of each group, the RCF track of a specimen from each group was reexamined using XRD to measure RA volume fraction and RS. The results of the XRD RA measurements are shown in Figure 5.6a. Figure 5.6b through 6d depict the post-RCF XRD RA measurements for each group plotted against their respective RA measurements prior to RCF testing. The amount of RA in the Low RA specimen remained constant despite the 120 million RCF passes. The Mid RA specimen exhibited some amount of RA decomposition but was not reduced beyond the RA level observed in the Low RA specimen. Remarkably, little RA

decomposition is observed in the High RA specimen after 333 million cycles. To confirm this finding, additional measurements were taken at two additional RCF tracks on the High RA specimen. The results are shown as Figure. 5.6e. The additional measurements verify that despite having large amounts of RA available in the High RA group, the RA remained stable throughout the entire fatigue process. It was speculated that the RA decomposition in the High RA group was occurring at depths correlated with the maximum orthogonal shear. Figure 5.6e exhibits a distinct drop in RA amount for all three measured RCF tracks at a depth of $89\ \mu m$. The maximum shear reversal is expected to occur at $76.5\ \mu m$ according to Hertzian theory for elastic bodies in contact. It is hypothesized that the lower hydrostatic pressure present at the location of maximum orthogonal shear compared to the location of maximum resolved shear induces more RA decomposition. However, the results are not conclusive to confirm this hypothesis. XRD measurements of the internal stresses acting in the circumferential direction of the rod specimen are provided in Figure 5.7a through 5.7d. The Low RA group shows no significance change in the residual stress state. However, the Mid and High groups show an appreciable increase in the compressive residual stress state after testing. Generally, this increase in compressive internal stress is attributed to the volume expansion associated with the RA transformation, however, no significant change in RA concentration was observed in these measurements. The higher internal compressive stresses are generally considered beneficial to RCF life. Both the High and Mid RA groups, which generated additional internal compressive stresses, were outperformed by the Low RA group which exhibited no increase in the compressive residual stress state.

The martensitic transformation of metastable RA is considered a benefit which can improve fatigue life. However, the stability or resistance of the RA to undergo a phase transformation is affected by many factors: alloying, heat treatment, size, and morphology [56,57,106,110,111]. As the experimental results indicate, RA that is too stable will not undergo the beneficial transformation and may act to reduce RCF life. Conversely, RA that is not adequately stable will undergo the martensitic transformation prematurely and the maximum benefit is not achieved [98]. This was previously observed for torsional fatigue of AISI 8620 carburized steel [112]. Much of the RA had undergone the phase transformation within the first cycle of fatigue and did not cause significant change in the material condition. Only a small portion of the RA volume fraction produced behavior beneficial to resisting fatigue.

The high RA specimens had a significant amount of RA within the microstructure, however, the RA remained stable throughout the entire test and the RCF performance was worse compared to the lower RA specimens. There is a trade-off between retaining austenite in the matrix and producing a fine martensitic microstructure. As the EBSD and optical results indicate, the Lower RA group was able to produce a more distorted and fine martensitic structure due to the induced RA transformations during severe undercooling. Therefore, the inability to transform the RA in the High and Mid group during RCF testing, combined with an initial finer martensitic microstructure in the Low RA group, resulted in higher RCF lives in the Low RA group. The decision to seek more RA in the microstructure must be considered against what quality of steel microstructure could be produced if the RA was removed. Further, highly stable RA is a detriment to the steel microstructure as it is intrinsically weaker than the martensitic structure. The results highlight that RA quantity alone is not sufficient criteria to predict RCF performance.

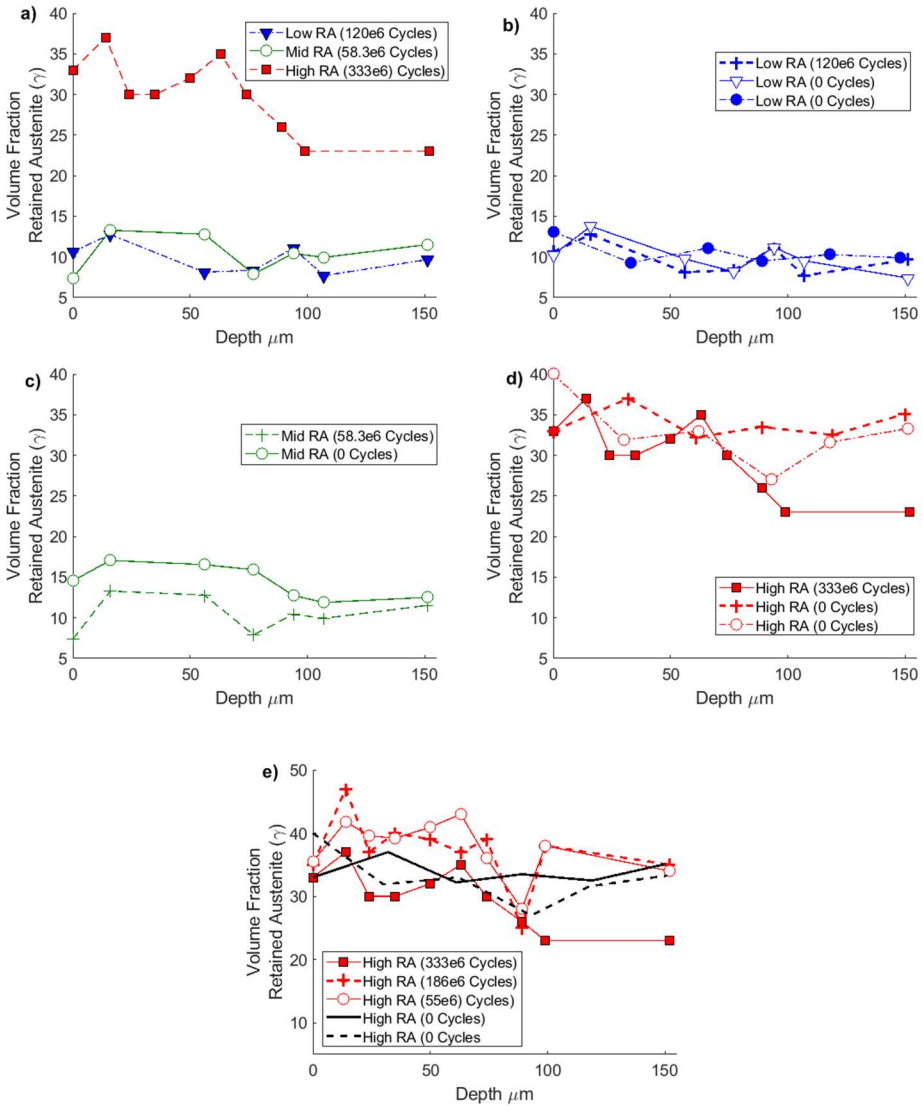

Figure 5.6: a) XRD RA measurements of RCF tracks from each of the three RA groups. Direct comparison between the XRD measurements before and after RCF testing are given in b) – d) for the Low, Mid, and High groups, respectively. e) Additional XRD measurements on th

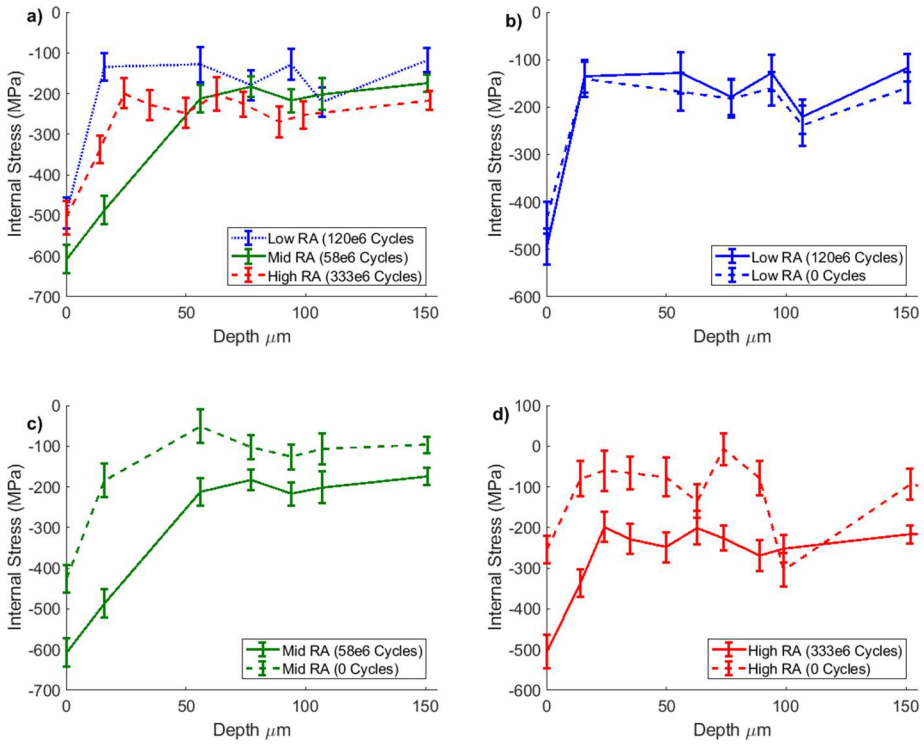

Figure 5.7: a) XRD RS measurements of RCF tracks from each of the three RA groups. Direct comparison between the XRD measurements before and after RCF testing are given in b) – d) for the Low, Mid, and High groups, respectively.

5.3 RCF Simulation

The experimental RCF results demonstrated that a lower RA concentration improved performance. XRD examination demonstrated that the majority of the RA in the system remained untransformed despite millions of rolling passes. To examine the effect RA stability may have on RCF performance, a 2D continuum damage mechanics (CDM) finite element model (FEM) was further developed to investigate the effects of RA stability (E_T) on RCF performance. The RCF CDM ABAQUS FE model has been described in previous works. [78,113]

Figure 5.8a depicts the ABAQUS domain developed and used in this investigation. The domain is a semi-infinite plane strain FEM extending -10b to 10b along the rolling direction and 10b in the vertical direction. The domain contains a center region known as the representative volume element (RVE) which extends from -1.5b to 1.5b along the rolling direction and down 2b from the surface. The pressure is moved from -2.5b to 2.5b across the top surface of the domain in 81 discrete steps to model a rolling pass. The ABAQUS UTRACLOAD subroutine was used

to pass a Hertzian pressure profile of half-width (b) and maximum pressure (P_{max}) on the surface of the finite element domain. The surface of the semi-infinite domain is subjected to a frictional force proportional to the applied pressure. The coefficient of friction used is $\mu = 0.05$, which is representative of good lubrication [114,115]. The domain is constructed using CPE3 elements with infinite elements acting as boundary conditions for the lateral and lower surfaces. The RVE was meshed using Voronoi tessellations with an average grain diameter of $10\ \mu m$.

Simulations were conducted at a set level of RA volume fraction (V_{RA}). In order to achieve the desired V_{RA} in the simulation while allowing for randomness in the RA distribution, a Gaussian distribution with a mean set to the target RA concentration and a standard deviation of 0.1 or 10% RA was used to assign V_{RA} values to each individual element within the RVE. If the total V_{RA} of the simulation differed from the desired target V_{RA} by $\pm 1\%$, then the V_{RA} values assigned to each element were adjusted until the total V_{RA} of the system fell within $\pm 1\%$ of the target or desired V_{RA}. In order to conform to reality, V_{RA} values assigned to individual elements had to fall within the range of $0\% - 100\%$. In order to account for variation in the material response due to varying amounts of V_{RA}, a Reuss boundary was used to describe the resultant Young's modulus (E') and the resultant Poisson's ratio (ν') of each element as a function of V_{RA}. Equations 5.1 and 5.2 [116] provide the formulas implemented within the ABAQUS subroutine UMAT to define elastic properties where E_a, ν_a are the Young's modulus and Poisson's ratio for austenite and E_m, ν_m are the Young's modulus and Poisson's ratio for the steel matrix or martensitic phase, respectively. Inelastic behavior was described using a J2 criteria with linear kinematic hardening as defined in equation 5.3 where $\dot{\alpha}, C, \sigma_0, \sigma, \alpha, \dot{\bar{\epsilon}}^{pl}$ are the change in the backstress, the kinematic hardening modulus, the yield strength, the stress tensor, the backstress, and the equivalent plastic strain rate, respectively. Values for the necessary material constants are provided in Table 5.5.

Table 5.5: Material parameters for RCF simulation[10,34,59]

Young's Modulus (E_a)	130 GPa
Young's Modulus (E_m)	228 GPa
Poisson's Ratio (ν_a, ν_m)	0.3
Linear Hardening Parameter (C)	6 GPa
Shear Resistance Parameter (σ_r)	5.97 GPa
Shear Exponent (m)	11.1
Crack Closure Parameter (h)	0.2
Coefficient of Friction	0.05

$$\frac{1}{E'} = \frac{V_{RA}}{E_a} + \frac{1-V_{RA}}{E_m} \tag{5.1}$$

$$\frac{1}{\nu'} = \frac{V_{RA}E_m + (1-V_{RA}) * E_a}{V_{RA}E_m\nu_a + (1-V_{RA})E_a\nu_m} \tag{5.2}$$

$$\dot{\alpha} = C\frac{1}{\sigma_0}(\sigma - \alpha)\,\dot{\epsilon}^{pl} \tag{5.3}$$

ABAQUS was used to solve for the stress fields resulting from the applied Hertzian pressure. The stress tensor at each element was extracted for each step of the simulation using a python script. The stresses acting on each element were utilized within a MATLAB script to perform necessary calculations for fatigue related damage and energy considerations to predict RA transformations.

5.3.1 Damage Mechanics

The damage variable, D, is defined by equation 5.4 where S is the total cross-sectional area of some arbitrary plane in the material and S_D is the area of voids lying on that plane. Therefore, as D increases, there is less material available to resist the applied loading. As Equation 5.5 demonstrates, the effective stress within the material (σ_{eff}) becomes infinite when $D = 1$.

$$D = \frac{S_D}{S} \tag{5.4}$$

$$\sigma_{eff} = \frac{\sigma}{1-D} \tag{5.5}$$

The damage accumulation associated to the fatigue process was calculated using equation 5.6 [117].

$$\frac{\Delta D}{\Delta N} = \left[\frac{\Delta \tau}{\sigma_r(1-Dh)}\right]^m \tag{5.6}$$

where $\frac{\Delta D}{\Delta N}, \Delta\tau, \sigma_r,$ and m are the rate of damage per cycle, the shear reversal induced by rolling contact, the material shear resistance parameter, and the material shear exponent, respectively. The damage calculation was performed for each individual finite element with the respective damage and shear reversal associated to that element. Material parameters m and σ_r are derived from a power law fit of the torsional fatigue data as described in previous work [10,118]. In accordance with Lemaitre [59], a crack closure parameter $h = 0.2$ was used to modify D directly. A microcrack was considered to occur at the grain boundary of any element where $D > 0.4$. To enable simulation of high cycle fatigue, the jump-in-cycles method originally proposed by Lemaitre [59] was implemented within this modeling procedure. The procedure assumed a constant rate of damage over a given block of cycles. The size of the block of cycles was calculated with respect to the critical damage rate $(dD/dN)_{crit}$ or the highest rate of damage occurring within the RVE. The simulation restricted the amount of damage accumulated by any one element to a maximum of 0.2 for any given block of cycles. By this restriction, the change in the number of cycles (ΔN) can be determined as follows.

$$\Delta N = \frac{\Delta D_c}{(dD/dN)_{crit}} \tag{5.7}$$

where ΔD_c was set to 0.2 for the current simulation. The ΔN value is then multiplied by the damage rates of all remaining elements within the RVE in order to update damage accumulation due to the fatigue process. After the damage was updated, the ABAQUS RCF simulation was performed again to determine new stress fields within the material and the numerical procedure was repeated. The simulation continued running until a crack reached the surface of the FE domain at which point failure was considered to occur.

5.3.2 Energy Criteria for RA Transformations due to RCF

The energy criteria to predict RA transformations is based on the premise that RA would undergo a spontaneous phase transformation if the steel matrix were not acting to halt the martensitic transformation. Therefore, as the material is subject to fatigue, useful work energy is dissipated as entropy [59]. This loss in useful work energy limits the ability of the steel matrix to halt the RA transformation. This reduces the barrier restricting the phase transformation from occurring until the transformation may occur spontaneously. Morris et al. [78] combined damage mechanics with principles of phase transformations in solids to formulate an energy criteria to predict RA transformations during a fatigue process. This was accomplished by recognizing that the Gibb's free energy enthalpy term could be directly related to the damage. The change in the Gibb's free energy due to damage could then be quantified and considered as the driving force for inducing martensitic transformations. The necessary equations to calculate the change in Gibb's free energy as a function of damage are provided by Lemaitre [60] and are presented below.

$$\Delta\Psi^* = \Delta\Psi_e^* + \frac{1}{\rho}\Delta\sigma_{ij}\Delta\epsilon_{ij}^p - \Delta\Psi_P \tag{5.8}$$

$$\Delta\Psi_e^* = \frac{\sigma_{eq}^2 R_{VE}}{2E(1-\Delta D)} \tag{5.9}$$

$$R_{VE} = \frac{2}{3}(1+\nu) + 3(1-2\nu)\left(\frac{\sigma_H}{\sigma_{eq}}\right)^2 \tag{5.10}$$

$$\Delta\Psi_P = \frac{1}{\rho}\left(\frac{1}{3}C\Delta\alpha_{ij}\Delta\alpha_{ij}\right) \tag{5.11}$$

In Equation (5.8), $\Delta\Psi^*, \Delta\Psi_e^*, \Delta\Psi_p, \rho, \Delta\sigma_{ij}, \Delta\epsilon_{ij}^p$ are the change in the specific Gibbs free energy to drive the phase transformation, the elastic contribution, the plastic contribution attributed to kinematic hardening, the material density, the change in stress, and corresponding plastic strain, respectively [78]. The elastic contribution $\Delta\Psi_e^*$, equation (5.9), is calculated from the equivalent von Mises stress σ_{eq}, the elastic modulus E, the damage variable D, and the triaxiality function defined in equation (5.10) where ν and σ_H are the Poisson's ratio and hydrostatic stress, respectively

In addition to the above, the modeling approach developed for this investigation considered the effect of stress-assisted transformations. Each Voronoi tessellation within the RVE was

randomly assigned three Euler angles to be used in a ZXZ rotation sequence to define a unique crystal orientation in space. These crystallographic orientations were used to resolve shear and normal stresses acting on habit planes to modify energy requirements for the martensitic transformation [28]. Shear and tensile stresses acting on the habit planes facilitate the phase transformation while normal compressive stresses act to resist the transformation in accordance to equation 5.11 where U is the work energy driving the phase transformation and τ, σ are the shear and normal stress resolved on the habit plane. The shear and normal components of the transformational strain are denoted by γ_0 and ϵ_0 and are set at 0.2 and 0.04, respectively. RA is considered to transform when the available energy in the system exceeds the energy threshold. The energy threshold increases as less RA is present in the system [57] until an upper energy limit is reached.

$$U = \tau\gamma_0 + \sigma_n\epsilon_0 \tag{5.12}$$

The martensitic transformation of RA is known to have an accompanying volume expansion which varies depending upon carbon content [80]. For the current simulations, the volume expansion was taken to be 3%. This volume expansion was considered to directly reduce damage in the material by acting to close material voids. In accordance with previous work [112], internal compressive stresses generated by the RA transformation were assigned based on the empirical relationship provided. The empirical relationship also accounts for material relaxation which leads to a decrease in material residual stresses as a function of fatigue cycles and applied stress. Internal compressive stresses were assigned using the SIGINI subroutine in ABAQUS at the beginning of each RCF simulation. The change in V_{RA} due to phase transformations was calculated along with damage using a MATLAB script. The elemental values of V_{RA} were then updated in the ABAQUS simulation to modify material properties and alter stress fields.

5.3.3 Validation and Parametric Study

To validate the modeling approach, the RCF simulation was first run with a high value of RA stability (E_T) under contact conditions identical to the experimental RCF testing: $P_{max} = 3.6, b = 153\ \mu m$. The simulation was run a total of 30 times per RA group to generate a Weibull distribution to be compared to experimental results, Figure 5.8b. The qualitative aspects of the

modeling show good agreement with the experimental data. The lowest RA group performed the best with no significant difference between the intermediate and high RA group. The predicted lives from the simulations are smaller than the experimental lives, however, the interest is to examine the relative change in RCF performance based on RA stability. The simulation results for the validation case were further examined to determine the amount of RA decomposition which occurred during the RCF process. As observed in Figure 5.8c, the RA volume fraction remained unchanged from the initial state. This is similar to the behavior observed in the experimental results which showed no discernable change of the aggregate amount of RA after testing.

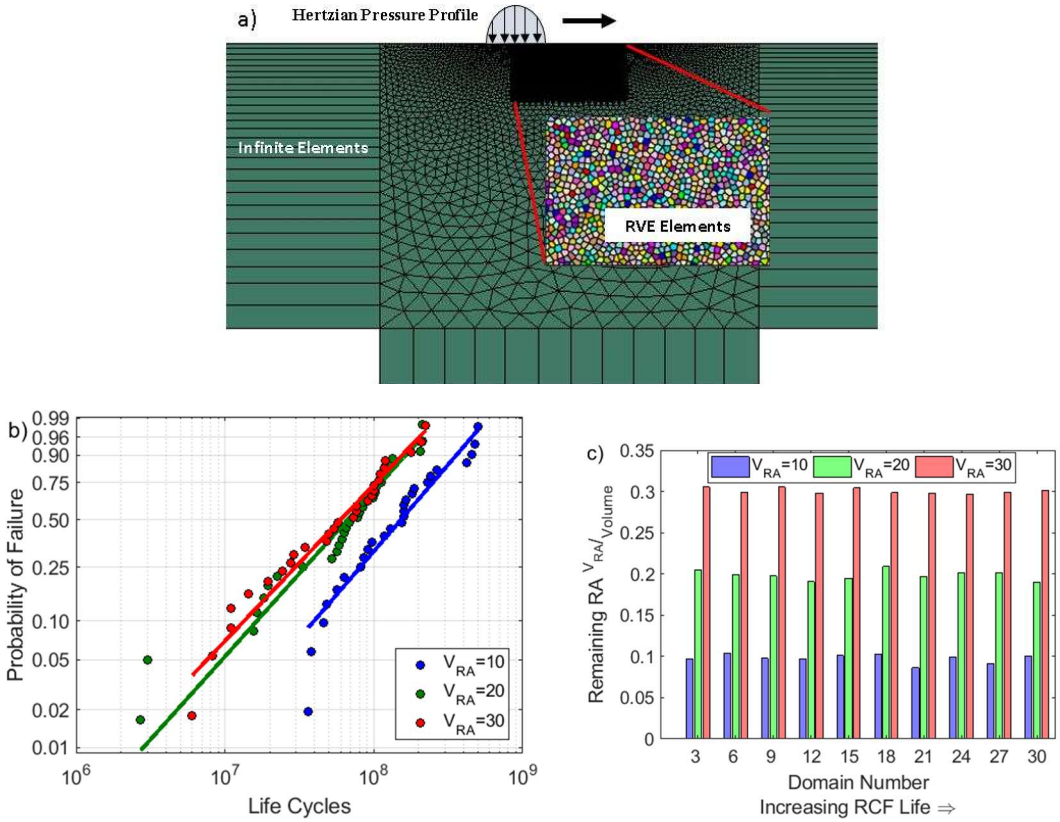

Figure 5.8: a) Representation of RCF simulation in ABAQUS. b) Comparison of predicted RCF lives from FEM simulation run at P_max=3.6 GPa;b=153 μm;E_T=15 GJ/g against experimental RCF data of 8620 steel. c) Amount of RA remaining in the simulation at the time of RCF

Upon finding good qualitative agreement between the simulated and experimental results, a parametric study was undertaken to investigate the effects of RA quantity and stability on RCF. The parametric study varied the amount of RA present, the energy threshold to induce RA

transformations, and the applied Hertzian contact pressure on the material. Table 5.6 provides the values applied in the study. The RA volume fraction (V_{RA}) and Hertzian pressure (P_{max}) are self-explanatory. The energy threshold (E_T) is the initial energy barrier to induce the RA transformation.

Due to the stochastic nature of assigning the elemental values of V_{RA} in the RCF simulations, it was necessary to perform multiple simulations for the same set of parametric conditions to characterize the failure distribution. 30 domains were run for each condition in order to generate a Weibull distribution of the RCF lives as a means to compare performance. The results were fitted using a 2-parameter Weibull distribution to compare against different parametric conditions. The results of the study are given in Table 5.6 as the L50 lives in millions of cycles for the various parametric conditions. As expected RCF life is found to increases as P_{max} is reduced in the simulation.

The parametric study found that lowering the stability of the RA resulted in an increase in predicted RCF life in all RA groups. However, this increase did not occur until the lowest E_T value was used. Figure 5.9 depicts the RCF simulation results with large improvement in RCF life at the lowest E_T value. .If the required driving force was sufficiently low, more RA in the material became a benefit to RCF performance as observed in Figure 5.10. The relative difference in RCF performance between the three RA groups was also dependent on the applied P_{max}. A higher contact pressure will result in a higher driving force inducing more RA transformations. Thus higher RA concentrations were favored under higher contact pressures as the RA was more likely to transform. The simulations demonstrate the importance of RA stability on RCF performance. Knowing only the amount of RA present is insufficient information for determining whether RA will be beneficial to RCF performance.

Table 5.6: L50 lives for the various parameteric conditions. Values are in millions of cycles

Volume Fraction or Retained Austenite (V_{RA})	Energy Threshold (E_T) $15e^{-9}\frac{GJ}{g}$	$10e^{-9}\frac{GJ}{g}$	$5e^{-9}\frac{GJ}{g}$	$1e^{-9}\frac{GJ}{g}$	
10% RA	81	44	66	492	P_{max} 3.5 GPa
20% RA	43	26	29	1,336	
30% RA	27	15	12	1,036	
10% RA	183	110	101	1,821	P_{max} 3 GPa
20% RA	156	117	133	3,099	
30% RA	129	100	76	1,396	
10% RA	687	811	779	7,906	P_{max} 2.5 GPa
20% RA	600	513	732	8,265	
30% RA	528	585	711	1,724	
10% RA	5,373	4,859	4,703	18,041	P_{max} 2 GPa
20% RA	3,337	3,089	3,803	13,645	
30% RA	3,537	4,249	5,743	3,497	

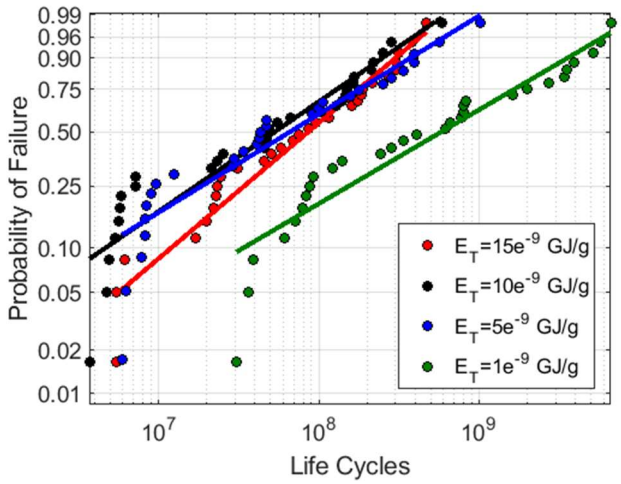

Figure 5.9: Predicted RCF lives as E_T is varied given P_max=3.5 GPa;b=100 μm with a RA volume fraction of 10%. An increase in life is not observed until the lowest energy threshold.

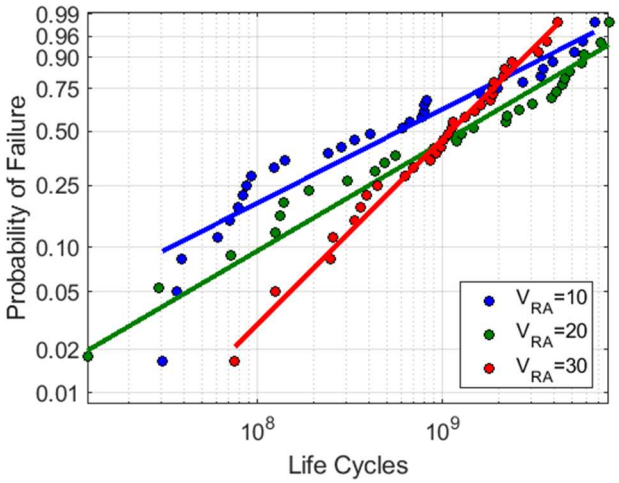

Figure 5.10: Predicted RCF lives given $P_{max} = 3.5\ GPa; b = 100\ \mu m;$ $E_T = 1e-9\frac{GJ}{g}$. With the lower energy requirement, the higher concentration of RA becomes beneficial to RCF performance.

5.4 Summary and Conclusion

The effect of RA volume fraction in RCF has long been a topic of interest for many decades. It is usually assumed that more RA within the system results in improved fatigue life. However, experimental work performed on case-carburized 8620 steel has shown that increasing the amount of RA present within a material system does not necessarily improve RCF life. In this investigation, all specimens underwent an identical carburization and tempering process in an effort to maintain chemical composition and similar microstructures between the three groups. Variation in RA volume fraction was achieved through varying the severity of undercooling between the carburization and tempering process.

The specimens were subject to RCF in a 3 ball and rod machine. Despite millions of fatigue cycles at high contact pressures (3.6 GPa), little to no RA decomposition was induced in the material. The high stability of the RA restricted phase transformations which halted the formation of additional martensite in the microstructure. This resulted in an overall weaker microstructure which was detrimental to RCF performance. The importance of RA stability was explored using a FEM CDM model incorporating RA transformations. If RA stability was reduced below a certain threshold, then RCF performance was found to improve regardless of the RA concentration. Additionally, higher RA concentration outperformed lower RA groups at the lower driving force

requirements. The experimental and analytical results indicate that RA considerations must extend beyond simply quantifying the amount of RA to ensure RA is beneficial to RCF performance.

CHAPTER 6. SUMMARY

In Chapter Two, a thermodynamics based theory for predicting RA transformation during RCF was presented. The energy based criteria was constructed by combining principles from phase transformations in solids with the field of damage mechanics. The energy criteria considered elastic, plastic, thermal, and dissipative energy contributions to the phase transformation. The required driving force for RA transformation was taken from the open literature with special consideration of normal stresses acting on the parent austenite habit planes. The criteria was implemented in an FEM simulation of RCF to corroborate results against experimental data. Multiple damage causing mechanisms were considered and compared against experimental data to determine best fit.

Chapter Three further discussed the RCF modeling by considering microstructural deterioration, the RA transformation, and RS formation occurring during RCF. An FEM domain was developed from Voronoi tessellations to represent prior austenite grain boundaries. Grains were assigned crystal orientation to modify required driving force for the RA transformation. Damage laws were modified to consider RS and different components of the stress as the driver of failure. RS was allowed to develop due to RA transformation and were implemented to directly alter the fatigue process. Common RS profiles achieved through various manufacturing post-processing procedures were investigated to examine RCF performance as a function of initial RS profile. The modeling approach was capable of capturing an evolving microstructure and produced results similar to experimental observation such as DER formation.

Chapter Four discussed experimental data to investigate the stability and formation of RS in bearing steel material due to RA transformation. Specimens of 8620 case carburized steel were subjected to torsional fatigue at specific stress levels for a prescribed number of cycles. After fatigue testing, x-ray diffraction techniques were used to measure RS and RA volume fraction as a function of depth in the material. The results identified RA transformation and material relaxation as two competing phenomena in the material. An empirical model was developed to predict RS formation as a function of RA transformation and material relaxation. The model was corroborated with experimental results. Further, the results indicate that only a small portion of the total RA was useful in generating compressive residual stresses. This demonstrated the

importance of controlling the loading condition in order to maximize residual stress formation associated with the RA transformation.

Chapter Five presented experimental and analytical work demonstrating the significance of RA stability on RCF performance. Varying levels of retained austenite (RA) were achieved through varying undercooling severity in uniformly treated case carburized 8620 steel. Specimens were characterized via XRD and EBSD techniques to determine RA volume fraction and material characteristics prior to rolling contact fatigue (RCF). Higher RA volume fractions did not lead to improvement in RCF lives. XRD measurements after RCF testing indicated that little RA decomposition had occurred during RCF. A continuum damage mechanics (CDM) finite element model (FEM) was then developed to investigate the effects of RA stability on RCF. The results obtained from the CDM FEM captured similar behavior observed in the experimental results. Utilizing the CDM FEM, a parametric study was undertaken to examine the effects of RA quantity, RA stability, and applied pressure on RCF performance. The study demonstrates that the energy requirements to transform the RA phase is critical to RCF performance.

REFERENCES

[1] Lundberg G. Dynamic capacity of rolling bearings. IVA Handl 1947;196.

[2] Bhadeshia H. Steels for bearings. Prog Mater Sci 2012;57:268–435.

[3] Mercier JP, Zambelli G, Kurz W. Introduction to materials science. Elsevier; 2012.

[4] Porter, David A, Easterling, Kenneth E, Sherif, Mohamed Y. Phase Transformations in Metals and Alloys. Third. 2008.

[5] Zaretsky E V. STLE life factors for rolling bearings. STLE Spec Publ SP 1992.

[6] Baughman RA. Effect of Hardness, Surface Finish, and Grain Size on Rolling-Contact Fatigue Life of M-50 Bearing Steel. J Basic Eng 1960;82:287–94.

[7] Perez M, Sidoroff C, Vincent A, Esnouf C. Microstructural evolution of martensitic 100Cr6 bearing steel during tempering: From thermoelectric power measurements to the prediction of dimensional changes. Acta Mater 2009;57:3170–81.

[8] Chakraborty J, Bhattacharjee D, Manna I. Austempering of bearing steel for improved mechanical properties. Scr Mater 2008;59:247–50.

[9] Harish S, Bensely A, Lal DM, Rajadurai A, Lenkey GB. Microstructural study of cryogenically treated En 31 bearing steel. J Mater Process Technol 2009;209:3351–7.

[10] Shen Y, Moghadam SM, Sadeghi F, Paulson K, Trice RW. Effect of retained austenite–Compressive residual stresses on rolling contact fatigue life of carburized AISI 8620 steel. Int J Fatigue 2015;75:135–44.

[11] Dong Z, Fu-Xing W, Qi-Gong C, Ming-Xin Z, Yin-Quian C. Effect of retained austenite on rolling element fatigue and its mechanism. Wear 1985;105:223–34.

[12] Dommarco RC, Kozaczek KJ, Bastias PC, Hahn GT, Rubin CA. Residual stresses and retained austenite evolution in SAE 52100 steel under non-ideal rolling contact loading. Wear 2004;257:1081–8.

[13] Zheng C, Dan R, Zhang F, Lv B, Yan Z, Shan J, et al. Effects of retained austenite and hydrogen on the rolling contact fatigue behaviours of carbide-free bainitic steel. Mater Sci Eng A 2014;594:364–71.

[14] Yajima E, Miyazaki T, Sugiyama T, Terajima H. Effects of Retained Austenite on the Rolling Fatigue Life of Ball Bearing Steels. Trans Japan Inst Met 1974;15:173–9.

[15] Xie ZJ, Ren YQ, Zhou WH, Yang JR, Shang CJ, Misra RDK. Stability of retained austenite in multi-phase microstructure during austempering and its effect on the ductility of a low carbon steel. Mater Sci Eng A 2014;603:69–75.

[16] Richman RH, Landgraf RW. Some effects of retained austenite on the fatigue resistance of carburized steel. Metall Trans A 1975;6:955–64.

[17] Huo CY, Gao HL. Strain-induced martensitic transformation in fatigue crack tip zone for a high strength steel. Mater Charact 2005;55:12–8.

[18] Antolovich SD, Chanani GR. Subcritical crack growth of TRIP steels in air under static loads. Eng Fract Mech 1972;4:765–76.

[19] Zhirafar S, Rezaeian A, Pugh M. Effect of cryogenic treatment on the mechanical properties of 4340 steel. J Mater Process Technol 2007;186:298–303.

[20] Roy S, Gould B, Zhou Y, Demas NG, Greco AC, Sundararajan S. Effect of Retained Austenite on White Etching Crack Behavior of Carburized AISI 8620 Steel Under Boundary Lubrication. Tribol Lett 2019;67:40.

[21] Averbach BL, Cohen M, Fletcher SG. THE DIMENSIONAL STABILITY OF STEEL. 3. DECOMPOSITION OF MARTENSITE AND AUSTENITE AT ROOM TEMPERATURE. Trans Am Soc Met 1948;40:728–57.

[22] Cohen M. RETAINED AUSTENITE (1948 CAMPBELL, EDWARD, DEMILLE MEMORIAL LECTURE). Trans Am Soc Met 1949;41:35–94.

[23] Pearson PK. Size change of through hardened bearing steels at application temperatures. 1997.

[24] Duval P, Murry G, Constant A. Stabilité dimensionnelle dans le temps. Contribution à l'étude des facteurs métallurgiques affectant la stabilité dimensionnelle des aciers'. Mécanique Electr 1968;11:28–37.

[25] Hengerer F, Nierlich W, Volkmuth J, Nützel H. Dimensional stability of high carbon bearing steels. Ball Bear J 1988;231:26–31.

[26] Franklin J, Hill P, Allen C. The Effect of Heat Treatment on Retained Austenite in a 1% Carbon--Chromium Bearing Steel. Heat Treat Met 1979;6:46–50.

[27] Voskamp AP. Microstructural stability and bearing performance. Bear. Steel Technol., ASTM International; 2002.

[28] Patel JR, Cohen M. Criterion for the action of applied stress in the martensitic transformation. Acta Metall 1953;1:531–8.

[29] Ghosh A, Singh SB, Chakraborti N. Optimization of stability of retained austenite in TRIP aided steel using data-driven models and multi-objective genetic algorithms. J ASTM Int(Mater Perform Charact) 2012;1.

[30] Perlade A, Bouaziz O, Furnemont Q. A physically based model for TRIP-aided carbon steels behaviour. Mater Sci Eng A 2003;356:145–52.

[31] Lani F, Furnémont Q, Van Rompaey T, Delannay F, Jacques PJ, Pardoen T. Multiscale mechanics of TRIP-assisted multiphase steels: II. Micromechanical modelling. Acta Mater 2007;55:3695–705.

[32] Fischer FD. A micromechanical model for transformation plasticity in steels. Acta Metall Mater 1990;38:1535–46.

[33] Alley ES, Neu RW. Microstructure-sensitive modeling of rolling contact fatigue. Int J Fatigue 2010;32:841–50.

[34] Hatem TM. Microstructural modeling of heterogeneous failure modes in martensitic steels. ProQuest; 2009.

[35] Anoop AD, Sekhar AS, Kamaraj M, Gopinath K. Modelling the mechanical behaviour of heat-treated AISI 52100 bearing steel with retained austenite. Proc Inst Mech Eng Part L J Mater Des Appl 2015:1464420715612235.

[36] Xie L, Zhou Q, Wen Y, Wang L, Lu W. Microstructure variation and local plastic response of chrome molybdenum alloy steel after quasi rolling contact fatigue testing. Mater Sci Eng A 2016.

[37] Voskamp AP. Microstructural changes during rolling contract fatigue: Metal fatigue in the subsurface region of deep groove ball bearing inner rings. TU Delft, Delft University of Technology, 1997.

[38] Šme\clova V, Schwedt A, Wang L, Holweger W, Mayer J. Electron microscopy investigations of microstructural alterations due to classical Rolling Contact Fatigue (RCF) in martensitic AISI 52100 bearing steel. Int J Fatigue 2017;98:142–54.

[39] Evans M-H, Walker JC, Ma C, Wang L, Wood RJK. A FIB/TEM study of butterfly crack formation and white etching area (WEA) microstructural changes under rolling contact fatigue in 100Cr6 bearing steel. Mater Sci Eng A 2013;570:127–34.

[40] Martin JA, Borgese SF, Eberhardt AD. Microstructural alterations of rolling—bearing steel undergoing cyclic stressing. J Basic Eng 1966;88:555–65.

[41] Swahn H, Becker PC, Vingsbo O. Martensite decay during rolling contact fatigue in ball bearings. Metall Mater Trans A 1976;7:1099–110.

[42] Voskamp AP, Österlund R, Becker PC, Vingsbo O. Gradual changes in residual stress and microstructure during contact fatigue in ball bearings. Met Technol 1980;7:14–21.

[43] Österlund R, Vingsbo O. Phase changes in fatigued ball bearings. Metall Mater Trans A 1980;11:701–7.

[44] Oila A, Shaw BA, Aylott CJ, Bull SJ. Martensite decay in micropitted gears. Proc Inst Mech Eng Part J J Eng Tribol 2005;219:77–83.

[45] Huang M, He B, Van der Zwaag S. Effect of free surface on martensitic transformation in individual retained austenite grains. Int. Conf. Solid-Solid Phase Transform. Inorg. Mater. PTM 2015, 2015.

[46] Da Silva VF, Canale LF, Spinelli D, Bose-Filho WW, Crnkovic OR. Influence of retained austenite on short fatigue crack growth and wear resistance of case carburized steel. J Mater Eng Perform 1999;8:543–8.

[47] Abareshi M, Emadoddin E. Effect of retained austenite characteristics on fatigue behavior and tensile properties of transformation induced plasticity steel. Mater Des 2011;32:5099–105.

[48] Kaufman L, Cohen M. Thermodynamics and kinetics of martensitic transformations. Prog Met Phys 1958;7:165–246.

[49] Radcliffe S V, Schatz M. The effect of high pressure on the martensitic reaction in iron-carbon alloys. Acta Metall 1962;10:201–7.

[50] Singh KP, Parr JG. Thermodynamics of the martensite transformation. Acta Metall 1961;9:1073–4.

[51] Zener C. Kinetics of the decomposition of austenite. Trans Aime 1946;167.

[52] Cohen M, Machlin ES, Paranjpe VG. Thermodynamics in Physical metallurgy. Am Soc Met 1950:264.

[53] Nishiyama Z. Martensitic transformation. Elsevier; 2012.

[54] Yang H-S, Bhadeshia H. Austenite grain size and the martensite-start temperature. Scr Mater 2009;60:493–5.

[55] Capdevila C, Caballero FG, de Andrés C. Analysis of effect of alloying elements on martensite start temperature of steels. Mater Sci Technol 2003;19:581–6.

[56] Wang J, Van Der Zwaag S. Stabilization mechanisms of retained austenite in transformation-induced plasticity steel. Metall Mater Trans A 2001;32:1527–39.

[57] Park HS, Han JC, Lim NS, Seol J-B, Park CG. Nano-scale observation on the transformation behavior and mechanical stability of individual retained austenite in CMnSiAl TRIP steels. Mater Sci Eng A 2015;627:262–9.

[58] Dan WJ, Zhang WG, Li SH, Lin ZQ. A model for strain-induced martensitic transformation of TRIP steel with strain rate. Comput Mater Sci 2007;40:101–7.

[59] Lemaitre J. A course on damage mechanics. Springer Science & Business Media; 2012.

[60] Lemaitre J, Desmorat R. Engineering Damage Mechanics: ductile, creep, fatigue and brittle failures. Springer Science & Business Media; 2005.

[61] Rubin CA, Chen Q, Kim K. Analysis of the rolling contact residual stresses and cyclic plastic deformation of SAE 52100 steel ball bearings. J Tribol 1987;109:619.

[62] Xiao Y-C, Li S, Gao Z. A continuum damage mechanics model for high cycle fatigue. Int J Fatigue 1998;20:503–8.

[63] Raje N, Slack T, Sadeghi F. A discrete damage mechanics model for high cycle fatigue in polycrystalline materials subject to rolling contact. Int J Fatigue 2009;31:346–60.

[64] Slack T, Sadeghi F. Explicit finite element modeling of subsurface initiated spalling in rolling contacts. Tribol Int 2010;43:1693–702.

[65] Warhadpande A, Jalalahmadi B, Slack T, Sadeghi F. A new finite element fatigue modeling approach for life scatter in tensile steel specimens. Int J Fatigue 2010;32:685–97.

[66] Weinzapfel N, Sadeghi F. Numerical modeling of sub-surface initiated spalling in rolling contacts. Tribol Int 2013;59:210–21.

[67] Jalalahmadi B, Sadeghi F. A Voronoi FE fatigue damage model for life scatter in rolling contacts. J Tribol 2010;132:21404.

[68] Warhadpande A, Sadeghi F. Effects of surface defects on rolling contact fatigue of heavily loaded lubricated contacts. Proc Inst Mech Eng Part J J Eng Tribol 2010;224:1061–77.

[69] Bomidi JAR, Weinzapfel N, Sadeghi F, Liebel A, Weber J. An improved approach for 3D rolling contact fatigue simulations with microstructure topology. Tribol Trans 2013;56:385–99.

[70] Bai MK, Pang JC, Wang GD, Yi HL. Martensitic transformation cracking in high carbon steels for bearings. Mater Sci Technol 2016;32:1179–83.

[71] Warhadpande A, Sadeghi F, Kotzalas MN, Doll G. Effects of plasticity on subsurface initiated spalling in rolling contact fatigue. Int J Fatigue 2012;36:80–95.

[72] Clyne TW, Withers PJ. An introduction to metal matrix composites. Cambridge university press; 1995.

[73] Shimizu S, Tsuchiya K, Tosha K. Probabilistic Stress-Life (PSN) Study on Bearing Steel Using Alternating Torsion Life Test. Tribol Trans 2009;52:807–16.

[74] Blondé R, Jimenez-Melero E, Zhao L, Wright JP, Brück E, der Zwaag S, et al. High-energy X-ray diffraction study on the temperature-dependent mechanical stability of retained austenite in low-alloyed TRIP steels. Acta Mater 2012;60:565–77.

[75] Jones A. Metallographic observations of ball bearing fatigue phenomena. Symp. Test. Bear., 1947.

[76] Becker PC. Microstructural changes around non-metallic inclusions caused by rolling-contact fatigue of ball-bearing steels. Met Technol 1981;8:234–43.

[77] Muro H, Tsushima N. Microstructural, microhardness and residual stress changes due to rolling contact. Wear 1970;15:309–30.

[78] Morris D, Sadeghi F, Chen Y-C, Wang C, Wang B. A novel approach for modeling retained austenite transformations during rolling contact fatigue. Fatigue Fract Eng Mater Struct 2018;41:831–43.

[79] Voskamp AP. Material response to rolling contact loading. ASME, Trans J Tribol 0742-4787) 1985;107:359–64.

[80] Moyer JM, Ansell GS. The volume expansion accompanying the martensite transformation in iron-carbon alloys. Metall Mater Trans A 1975;6:1785–91.

[81] Voothaluru R, Bedekar V, Xie Q, Stoica AD, Hyde RS, An K. In-Situ Neutron Diffraction and Crystal Plasticity Finite Element Modeling to study the Kinematic Stability of Retained Austenite in Bearing Steels. Mater Sci Eng A 2017.

[82] Withers PJ, Bhadeshia H. Residual stress. Part 2--Nature and origins. Mater Sci Technol 2001;17:366–75.

[83] Johnson KL, Hearle K. Cumulative plastic flow in rolling and sliding line contact. J Appl Mech 1987;54:1.

[84] Meyer S, Brückner-Foit A, Möslang A. A stochastic simulation model for microcrack initiation in a martensitic steel. Comput Mater Sci 2003;26:102–10.

[85] Walvekar AA, Sadeghi F. Rolling contact fatigue of case carburized steels. Int J Fatigue 2017;95:264–81.

[86] Nikitin I, Altenberger I. Comparison of the fatigue behavior and residual stress stability of laser-shock peened and deep rolled austenitic stainless steel AISI 304 in the temperature range 25--600 C. Mater Sci Eng A 2007;465:176–82.

[87] Torres MAS, Voorwald HJC. An evaluation of shot peening, residual stress and stress relaxation on the fatigue life of AISI 4340 steel. Int J Fatigue 2002;24:877–86.

[88] Morrow J, Sinclair GM. Cycle-dependent stress relaxation. Symp. basic Mech. Fatigue, 1959.

[89] Jhansale HR, Topper TH. Engineering analysis of the inelastic stress response of a structural metal under variable cyclic strains. Cycl. Stress. Behav. Exp. Fail. Predict., ASTM International; 1971.

[90] Kodama S. The behavior of residual stress during fatigue stress cycles. Proc. Int. Conf. Mech. Behav. Met. II, Soc. Mater. Sci. Kyoto, vol. 2, 1972, p. 111–8.

[91] Zhuang WZ, Halford GR. Investigation of residual stress relaxation under cyclic load. Int J Fatigue 2001;23:31–7.

[92] Johnson KL, Johnson KL. Contact mechanics. Cambridge university press; 1987.

[93] Totten GE. Handbook of residual stress and deformation of steel. ASM international; 2002.

[94] Schwach DW, Guo YB. A fundamental study on the impact of surface integrity by hard turning on rolling contact fatigue. Int J Fatigue 2006;28:1838–44.

[95] Matsumoto Y, Hashimoto F, Lahoti G. Surface integrity generated by precision hard turning. CIRP Ann Technol 1999;48:59–62.

[96] Guo YB, Warren AW, Hashimoto F. The basic relationships between residual stress, white layer, and fatigue life of hard turned and ground surfaces in rolling contact. CIRP J Manuf Sci Technol 2010;2:129–34.

[97] Hossain R, Pahlevani F, Quadir MZ, Sahajwalla V. Stability of retained austenite in high carbon steel under compressive stress: an investigation from macro to nano scale. Sci Rep 2016;6:34958.

[98] García-Mateo C, Caballero FG. The role of retained austenite on tensile properties of steels with bainitic microstructures. Mater Trans 2005;46:1839–46.

[99] Lu J, Flavenot JF, Turbat A. Prediction of residual stress relaxation during fatigue. Mech. Relax. Residual Stress., ASTM International; 1988.

[100] Ooi GTC, Roy S, Sundararajan S. Investigating the effect of retained austenite and residual stress on rolling contact fatigue of carburized steel with XFEM and experimental approaches. Mater Sci Eng A 2018;732:311–9.

[101] Roy S, Sundararajan S. Effect of retained austenite on spalling behavior of carburized AISI 8620 steel under boundary lubrication. Int J Fatigue 2019;119:238–46.

[102] Kanetani K, Mikami T, Ushioda K. Effect of Retained Austenite on Sub-surface Initiated Spalling during Rolling Contact Fatigue in Carburized SAE4320 Steel. ISIJ Int 2020;60:1774–83.

[103] Roy S, Ooi GTC, Sundararajan S. Effect of retained austenite on micropitting behavior of carburized AISI 8620 steel under boundary lubrication. Materialia 2018;3:192–201.

[104] Smith WF. Structure and properties of engineering alloys. McGraw-Hill; 1993.

[105] Soleimani M, Kalhor A, Mirzadeh H. Transformation-induced plasticity (TRIP) in advanced steels: a review. Mater Sci Eng A 2020:140023.

[106] Xiong XC, Chen B, Huang MX, Wang JF, Wang L. The effect of morphology on the stability of retained austenite in a quenched and partitioned steel. Scr Mater 2013;68:321–4.

[107] Gibbs PJ, De Moor E, Merwin MJ, Clausen B, Speer JG, Matlock DK. Austenite stability effects on tensile behavior of manganese-enriched-austenite transformation-induced plasticity steel. Metall Mater Trans A 2011;42:3691–702.

[108] Glover D. A ball-rod rolling contact fatigue tester. Roll Contact Fatigue Test Bear Steels, ASTM STP 1982;771:107–25.

[109] Liston MJA. RCF life comparsion of bearing steels at two stress levels. Tribol Lubr Technol 1999;55:12.

[110] De Moor E, Matlock DK, Speer JG, Merwin MJ. Austenite stabilization through manganese enrichment. Scr Mater 2011;64:185–8.

[111] Sourmail T, Caballero FG, Moudian F, De Castro D, Benito M. High hardness and retained austenite stability in Si-bearing hypereutectoid steel through new heat treatment design principles. Mater Des 2018;142:279–87.

[112] Morris D, Sadeghi F, Singh K, Voothaluru R. Residual Stress Formation and Stability in Bearing Steels due to Fatigue induced Retained Austenite transformation. Int J Fatigue 2020:105610.

[113] Morris D, Sadeghi F, Chen Y-C, Wang C, Wang B. Effect of residual stresses on microstructural evolution due to rolling contact fatigue. J Tribol 2018;140.

[114] Polonsky IA, Keer LM. On white etching band formation in rolling bearings. J Mech Phys Solids 1995;43:637–69.

[115] Dahiwal R, Pörsch S, Löwenstein M, Sauer B. An Approach to Determine and Analyze the Wear Rates at Cage Pocket Contacts in Solid-Lubricated Rolling Bearings. Tribol Trans 2019;62:979–90.

[116] Yu W. Multiscale Structural Mechanics: Top-Down Modelling of Composites Using the Structural Genome. John Wiley & Sons, Limited; 2020.

[117] Raje N, Sadeghi F, Rateick RG. A statistical damage mechanics model for subsurface initiated spalling in rolling contacts. J Tribol 2008;130:42201.

[118] Morris D, Sadeghi F, Chen Y-C, Wang C, Wang B. Predicting Material Performance in Rolling Contact Fatigue via Torsional Fatigue. Tribol Trans 2019;62:614–25.